# Valuable Metals Recovery by Molten Salts Electrolysis

by

Tazdin Amietszajew

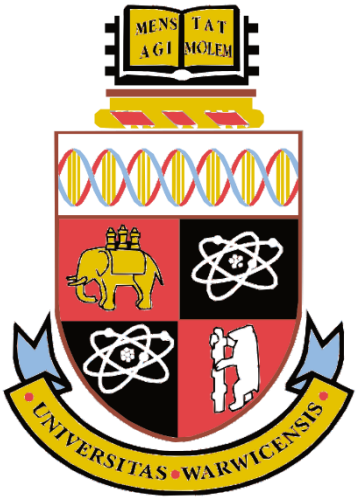


A thesis submitted in partial fulfilment of the requirements for the degree of
Doctor of Philosophy in Engineering

University of Warwick, WMG
September 2016

# Contents

# List of figures

# List of tables

# Acknowledgments

Writing a PhD is an adventure, one full of surprises and challenges. Although what is an adventure without a team of brave heroes?

Without the guidance of my supervisors, this work would never exist. Great thanks to Dr Rohit Bhagat for changing the issues into challenges and worries into exciting opportunities. Sincere thanks to Professor Sridhar Seetharaman for giving me the opportunity to work with him. The support and encouragement I got is immeasurable, the fountain of knowledge offered to me near limitless, just like their patience.

Above it all and behind everything stood my wife. Nadia gave me hope when I had little, and a 24 hours mental support service. I am extremely lucky to have found you.

Special thanks to my fellow PhD students, who offered the necessary distractions and a good amount of crazy ideas. Certain credit is owed to Sam, who bravely took up the challenge of assessing the language of my writings. Also big thanks to the University of Warwick staff members, who always offered a good piece of advice and support on every subject.

There would be no me without my family. I thank my parents for the true freedom of choice, and my sister for criticising every one I made. My mother's life wisdom, which I often cite, still surprises even the most scientific of minds.

Finally my friends, those for life, and those for a single story, no less important. Especially to Konrad *Siwy* Juszczyszyn and Paweł Stróż, whom I know I can look for no matter how lost I get.

Thank you all without whom this thesis would have never been written.

# Declaration

This thesis is submitted to the University of Warwick in support of my application for the degree of Doctor of Philosophy. It has been composed by myself and has not been submitted in any previous application for any degree.

The work presented (including data gathered and data analysis) was carried out by the author except in the case outlined below:

The X-ray Computed Tomography data used in the *Electrochemical analysis* section was gathered in collaboration with the *Metrology group, WMG, University of Warwick*.

Parts of this thesis have been published and/or presented by the author:

**Publications:**

- T. Amietszajew, S. Seetharaman, R. Bhagat, *The Solubility of Specific Metal Oxides in Molten Borate Glass*, Journal of the American Ceramic Society, Vol. 89, Issue 10, p. 2984-2987 (published)
- T. Amietszajew, J. M. Warnett, M. A. Williams, S. Sridhar, R. Bhagat, *Mechanistic analysis of copper and silver electrodeposition from molten salt systems*, Journal of the Electrochemical Society (submitted)
- T. Amietszajew, S. Sridhar, R. Bhagat, *Metal recovery by electrodeposition from a molten salt two-phase cell system*, Journal of the Electrochemical Society Vol. 163, Issue 9, p. D515-D521 (published)

**Conferences:**

- Royal Society of Chemistry – Molten Salts Discussion Group Student Conference, 10$^{th}$ of January 2014, University of Warwick, UK (poster presentation)
- Royal Society of Chemistry – Molten Salts Discussion Group Christmas Research Meeting, 15$^{th}$ of December 2014, London, UK (poster presentation)
- 3$^{rd}$ International Symposium on Sustainable Molten Salts and Ionic Liquid Processing, 4-9$^{th}$ of October 2015, Antalya, Turkey (oral presentation)
- 10$^{th}$ International Conference on Molten Slags, Fluxes and Salts, 22-25$^{th}$ of May 2016, Seattle, USA (oral presentation)
- WMG Doctoral Research and Innovation Conference, 21$^{st}$ of June 2016, University of Warwick, UK (oral presentation - best presentation award)

# Abstract

As the currently available methods for recycling of valuable metals from batteries and old electronics (commonly called eWaste) are in need of improvement, this project focuses on the development of a novel valuable metals recovery method by electrolysis in molten salts. The process proposed consists of three steps: metal oxides dissolution in borate salts, liquid-liquid interface ion transfer between the borate and chloride layer, and electrodeposition from the chloride phase. Inherent borate salts stability and its affinity to metals, coupled with the chloride salts large electrochemical window enables a stable and efficient (semi)-continuous process concept to be explored. Two electrolytic cell concepts akin to an industrial set-up were designed. The first composed of three interconnected chambers each for one of the three steps of the process, or a simpler, single-vessel solution relying on the immiscibility of the molten phases. For the needs of a laboratory scale testing the smaller, one vessel solution has been assembled. The proposed recycling method is a novel solution for the recovery of valuable metals considered and evaluated in this work; Co, Cu, Ni, and Mn, present in most Li-ion and Ni-MH batteries, but also other metals suitable for electrodeposition present in the eWaste or other metal-rich waste streams.

The process proposed was designed, evaluated and resulted in a successful recovery of all of the metals considered. Novel and promising experimental data on the metal oxides dissolution in molten borate salts is reported. Boron oxide salts were assessed, with the sodium borate achieving significant metals concentrations ranging from 4-20 wt%. Metals distribution between the oxide and halide layers was evaluated, and was found to be biased towards the borate layer due to its structure resulting in high metal affinity, with the metal ions concentration in the chloride layer around 1 wt% for the evaluated salts combination. This enables the sodium borate phase to work as a buffer, feeding the dissolved metal required for the electrodeposition into the chloride layer sustaining the process.

Liquid-liquid interface transfer and diffusion phenomena in the melt as well as the metal electrodeposition parameters were studied using a range of (electro)-analytical methods, validating the main steps of the proposed metal recovery process. The system was evaluated in a three-electrode set-up (WE: tungsten, CE; graphite, QRE: tungsten) and the formal redox reaction potentials were reported for the following feedstock: $Co_2O_3$ [-0.733/-1.848 V], CuO [-1.297/-2.375 V], $Mn_2O_3$ [-1.552 V] and NiO [-1.734 V] versus chlorine evolution. The recovered metals were analysed and found to form high purity (~99 %) dendritic deposits (SA/V of 950 $cm^{-1}$), which also supports the assumption of a diffusion controlled process. This marks the successful outcome of this proof-of-concept process, providing a feasible, alternative valuable metals recovery method design.

# Symbols

| | |
|---|---|
| $a$ | Activity |
| $A$ | Atomic mass |
| $c^{\infty}$ | Concentration (bulk) |
| $D$ | Diffusion coefficient |
| $E$ | Electrochemical potential |
| $E$ | Energy (in the *Economic analysis* section) |
| $F$ | Faraday constant |
| $\Delta G$ | Gibbs free energy |
| $I$ | Electric current |
| $K$ | Equilibrium constant |
| $k$ | Boltzmann's constant |
| $m$ | Mass |
| $N$ | Molar concentration |
| $n$ | Amount of electrons exchanged |
| $\eta$ | Dynamic viscosity |
| $\eta_{c/a}$ | Overpotential (cathodic/anodic) |
| $P$ | Power |
| $Q$ | Electric charge |
| $R$ | Gas constant |
| $R$ | Resistance |
| $r$ | Radius |
| $\rho$ | Density |
| $S$ | Surface |
| $T$ | Temperature |
| $t$ | Time |
| $U$ | Electric potential |
| $y$ | Activity coefficient |

# 1. Introduction

The development of a civilisation can be estimated by its growing energy consumption [1], and the portability of power sources is a natural step for a technologically developing society. Energy storage has become an increasingly important area, ubiquitous in mobile technology, electric vehicles (EVs) and land-based power backups. This in turn increases the prevalence of the Li-ion batteries in our everyday life. Without them, we would not be able to use the multitude of consumer electronics that surround us making our lives easier and more efficient. These electronic devices rely heavily on the rechargeable Li-ion or Ni-MH batteries [2]. Their presence in most of our accessories, ranging from a smartphone, a portable computer, GPS device to wireless toiletries, sets a definite foothold for the energy storage technology in the modern society. These devices are unthinkable to live without now, and all of them need the small but highly efficient portable batteries to work. All of these batteries are multi-component devices that rely on small quantities of materials where supply can be affected by geo-political factors. At the end of their end of life most Li-ion batteries are often land filled, leading to land pollution and loss of valuable metals used for their production[3].

Many valuable metals found in a battery (e.g. Co, Mn, Ni, Li) are rapidly diminishing, leading to the current or future rarity [4,5]. Most are not available in the UK, but remain essential components for many high-end technologies. Operating with small or difficult to mine resource sites, costly mining techniques and small concentrations, those elements are difficult to obtain. Recovery of such metals is of growing interest to both EU and USA, considering the growing constraints in raw materials availability, ore extraction and processing cost in the foreseeable future. However, in the US alone, 94 million USD worth of non-ferrous elements are disposed into the land-fill [3], while the recycling rate remain relatively low in major part due to the lack of relevant recycling technology [6].

## 1.1. Challenge and the recycling needs

European Commission Enterprise and Industry Directorate General [4] recognises cobalt as a critical metal and copper, manganese, nickel and lithium among others as of high economic importance. Europe is considered particularly vulnerable in case of shortage of such metals, due to the high dependency on the import from other countries and low natural resources. Many of the industrially essential elements (e.g. cobalt, manganese, rare earths) are mined only in a handful of countries, i.e. Brazil, China, Russia or South Africa, outside of Europe's

influence. These metals are virtually absent from the UK as natural resources. Regarding the global market, cobalt metal demand is being predicted to potentially outgrow the supply as soon as by 2025, in case of high market penetration of the mobile energy storage (i.e. electric vehicles) technology [5]. Lithium consumption is predicted to exceed the supply by 2050 [7], while copper and nickel resources are at risk of depletion within the next 50-100 years with the current rates of consumption [8]. Furthermore, the demand for metals associated with energy storage technology is only going to grow rapidly with the expanding global (hybrid-) electric vehicles market [5] and Tesla's car [9] and home [10] energy storage technologies, worsening the materials shortage predictions.

As the reliance on rare valuable metals is increasing, group of metals labelled as sparse and of diminishing resources, i.e. *critical metals*, is growing each year [4,5]. As an example, according to Argonne National Laboratory analysis [11] cobalt, manganese and nickel, together with lithium make up to ~50% of the Li-ion battery cost, with 1 kg of cell waste containing up to 200 g of cobalt and/or 150 g of copper. This places lithium, cobalt, manganese, copper and nickel together on a list of recoverable and valuable metals present in the battery eWaste stream to be found in the discarded cells.

The number of cars in the automotive industry of European Union is estimated to reach 377 million by 2030, with 52% of the annual sales being EVs [12] which contribute greatly to the Li-ion batteries consumption. Without proper recycling currently known rare/valuable metals sources (excluding oceans) affected by the EVs market growth might be depleted by the end of this century. Though the need of recycling is obvious, feasible methods are by no means given. Recycling methods are of low efficiency considering the amount and range of metals in the waste, as the complex chemistry developed in order to enhance the devices efficiency and lower prices complicate present recycling processes making it even more challenging [13].

Nevertheless, concentration of the metals considered in this project is in favour of utilising the aforementioned eWaste materials. For comparison, concentration of copper in copper ore is about 0.4-1%, while in a typical Li-ion battery the amount reaches up to 14.5%. In case of cobalt, which is scarcer in the Earth's crust, ranges from 5-20% of mass of a Li-ion battery. Having that in mind, energy storage market is a good source of recyclable material and among them a range of valuable metals [14].

In recent years several metals recovery methods have been adapted. However, they suffer from the drawback of not being originally developed for recycling from the considered eWaste

source, and thus they generate losses in valuable materials. Currently available and industrially used recycling methods for metal-rich electronics are mostly based on mechanical treatment, thermal, mechano-chemical process, leaching, bioleaching, solvent extraction, or chemical precipitation. Additionally, they create considerable amounts of waste using water or water-based solutions [13–22]. For these reasons, currently available methods are not economically viable for a wide range of materials and have an adverse environmental impact.

The **challenge** is to design a new, environmentally friendly and efficient method of recycling valuable metals from a wide range of waste feedstock, starting with Li-ion and Ni-MH batteries. A near-critical metal – cobalt is considered, as well as metals of significant economic importance – copper, nickel and manganese, all present in the considered eWaste stream. The investigation is conducted at temperatures ranging between 900-1000 $^{O}$C with the aim of finding a compromise between efficiency and the heat required for the process. The solution proposed is to use a two salt system based on borates and chlorides as the working salts. To process the desired metal, it needs to be extracted into the melt and then electroplated. Separate salts perform the roles of extracting and electroplating environment, for the best efficiency. Finally, optimal electrolytic cell construction needs to be developed in order to allow for efficient mass transfer and seamless cation exchange between the two separate salt phases.

## 1.2. Proposed metal recovery process

The process studied in this work aims to address the multi-metal components recycling needs. The method developed in this work uses a high-temperature molten-salts based system, composed of two immiscible salts; sodium borate and sodium chloride. By dissolving the metal oxides present in the scrap source, the borate layer works as a buffer providing metal ions into the chloride phase by a direct contact through a liquid-liquid interface. The electrolysis process occurs in the chloride layer, allowing for clean metal recovery. Therefore, the process relies on the metals solubility in the selected borate salt, metal ions transfer between the borate-chloride layers and electrolysis in the molten chloride, forming three main steps of the process, as shown in Figure 1.2-1 below. The process would occur at 900 $^{O}$C / 1173 K, which is a balance between the melting temperature of the melt components and their stability, as well as thermal resistance of the available vessel and metal electrodes, and the melting points of the metals considered for recovery.

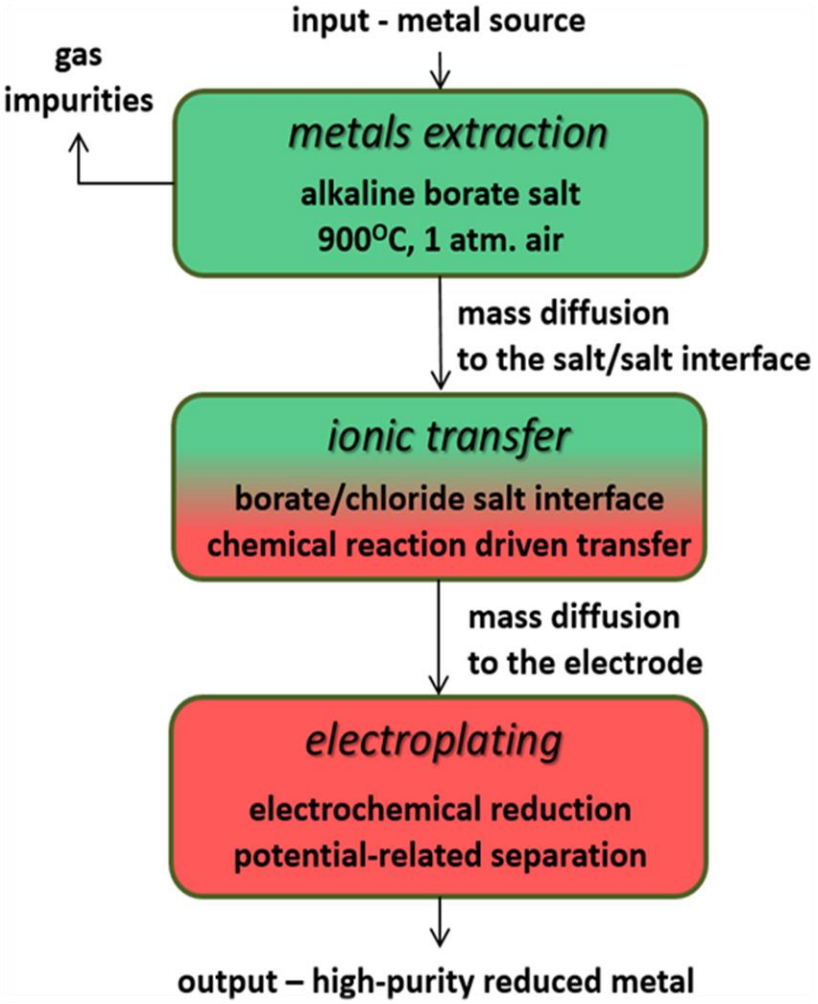


*Figure 1.2-1 Process idea flowchart. Each box represents one step of the process; metal dissolution, liquid-liquid interface transfer and electroplating, potentially done in a separate vessel.*

As shown in the figure, the process can be divided into three steps. Firstly, the feed material has to be dissolved in the borate layer, which will be kinetically (time-wise) and thermodynamically (concentration-wise) limited. Subsequently, the dissolved ions have to diffuse towards the liquid-liquid interface and transfer into the chloride layer. This process is governed by a chemical reaction on the interface, as is explained further in this thesis, section 2.4.3. Metal ions have to then diffuse towards the electrodes, where they will undergo electrochemical electroreduction, described in section 6.2, resulting in an electrolytic-purity metal deposits. The experimental work follows these steps as does the layout of this thesis.

The process proposed is novel and absent from the patent literature, as the commonly used electro-recovery processes work in single-phase systems, as will be discussed in section 2.2 and 2.3.3. The use of immiscible salts has been once suggested [23] for metals extraction, however not in the current configuration with the use in electrochemical cells. Additionally, the thermodynamic databases on the borate systems are lacking [24] as will be discussed later in this thesis in section 2.3.2, therefore the experimentation to follow fits within the knowledge gaps identified. A number of borate salt systems will be evaluated, with the aim of finding the most efficient combination, supported by pre-experimental thermodynamic analysis of the system using phase diagrams. A matching chloride salt will be used for electrolysis to avoid additional ions presence.

## 1.3. Layout of this thesis

This work describes the valuable metals recycling needs and potential sources rich in the metals considered. A metal recovery process is proposed. The following *Literature review* chapter 2 identifies the eWaste stream components and opportunities, and discusses the physicochemical aspects related to the process studied. The process requirements are identified, and a potential processing set-up is suggested. In the *Methodology* chapter 4 the experimental equipment and the basics of the methods used to evaluate the process are described. The following *Experimental* chapter 5 describes each test conducted in detail. The *Results and Discussion* chapter 6 evaluates the data collected and forms conclusions based on the results. Economic feasibility of the process and up-scale benefits are discussed in the *Economic analysis* chapter 7. The *Conclusions* chapter 8 summarises the findings, while the *Future work* chapter 9 outlines the possible further evaluation opportunities.

# 2. Literature Review

In the following literature review, the potential recoverable metal sources of interest are identified. The currently used metal recovery methods from eWaste sources are discussed and their drawbacks are identified, outlining the ground for potential improvements. Following, the known physicochemical properties of the system proposed are analysed and the lacking areas are recognised determining the subsequent experimentation.

As the process relies on the molten borate salts stability and metals solubility, these properties are discussed and predicted using computational thermodynamic software FactSage™ software and databases [24]. Secondly, electrochemistry of chloride salts is considered, as the electro-reduction process is the main step of recovery of the metals from the melt. Finally, the properties of the borate-chloride mix are evaluated, with the focus on the immiscibility of these two salts and the liquid-liquid ion interface transfer, essential for the availability of the metal ions for electrodeposition from the chloride phase.

## 2.1. Types of metal sources and waste feedstock

### 2.1.1. Primary valuable metals source – mining

Metals present in the rechargeable batteries considered in this project are, just like most other minerals, obtained by mining and ore processing. However, ore mining and processing is a very energy intensive process, with the *comminution* – process of crushing ore accounting for 4% of the world's total energy consumption [25]. Many of the valuable and technologically important materials are extracted from relatively remote locations outside of Europe, as previously mentioned. As the metal sources get slowly depleted, the grade of the ores mined declines [8], increasing the global price of the metals produced.

Copper is the most abundant of the metals considered in this project; however, the average ore currently mined is below 0.6% copper [26]. Nickel is primarily mined in Philippines and Indonesia, with the average ore mined containing on average 1% of nickel [27]. Cobalt is a side-product from copper and nickel mining, and therefore is considered at risk due to being reliant on other metals mining processes [5]. Most manganese is currently produced in South Africa, mainly as ferromanganese obtained by pyrometallurgical processing with iron ore, with a resulting manganese concentration of 30-80% [28]. Alternatively, pure metal can be obtained by hydrometallurgical methods through acid-leaching and subsequent electrowinning [29]. Alternatively, lithium metal is mainly extracted from water in brine pools, not ores, with

Chile, China and Australia as the main exporters [30]. The source sizes and reserves of lithium are difficult to estimate, depending on the scale of consumption, whether the metal will be extracted from the additional low-concentration sources like the oceans and how much lithium will be actually recycled back into the production streams [31].

In part in relation to the limited sources of these valuable metals, which often results in a highly unstable prices and availability [32], there are strong governmental incentives towards recycling [4,5]. It is known that scrap materials, specifically the eWaste stream contain much higher concentration of the precious metals than the primary sources [8]. The specific metals presence in the batteries is discussed in the next section. The recycling technology is already widely established for some of the most commonly used metals, offering significant benefits to the environment and energy efficiency. Analysing two of the most commonly used metals we can see that as much as ~50% of aluminium is recycled, saving 95% of the energy required in the initial production, while steel recycling saves 74% energy and 94% mining waste when compared to the ore processing [8].

### 2.1.2. Primary focus of recycling – rechargeable batteries

Rapid development of Li-ion and NiMH cells results in an increased consumption of Co, Cu, Mn, Ni, Zn and Li [11,33,34], with Li-ion and NiMH cells accounting for over 80% of the secondary galvanic cells market [22]. Li-ion batteries are designed to fit a wide range of electronic devices and come in different sizes and geometries: button cells, flat, small and large cell formats. Shape and size varying, the materials construction has some constant elements throughout every design. Figure 2.1-2 represents the breakdown of an average Li-ion battery elements cost.

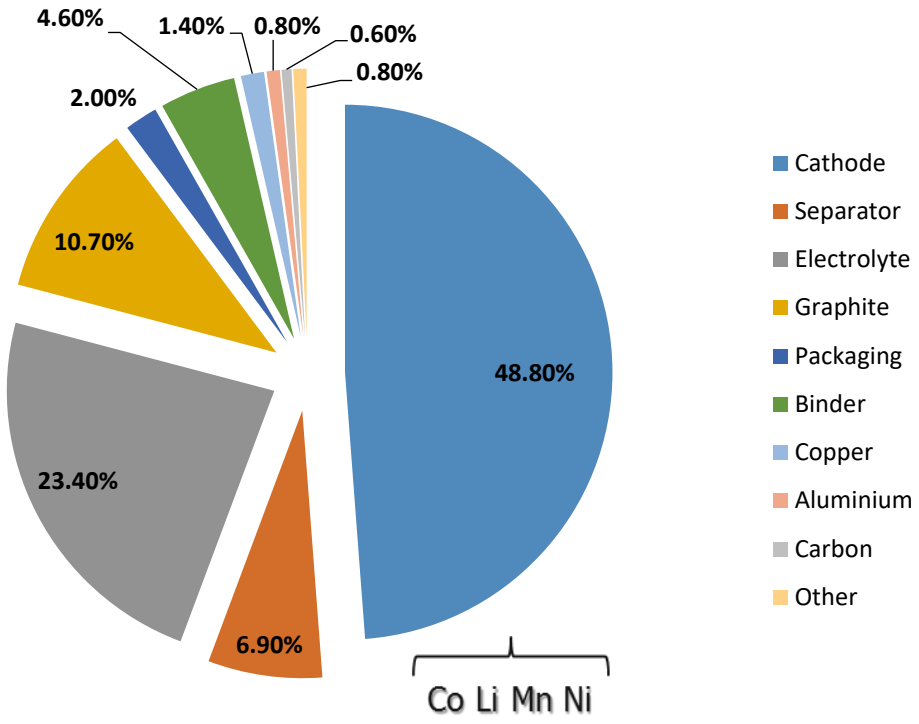


*Figure 2.1-1 Breakdown of lithium-ion battery elements cost. Cathode is the biggest contributor to the overall cost and can contain Co, Li Mn and Ni [11].*

The cathode contributes to most of the cost of the Li-ion battery. The cathode active material can contain Co, Ni and/or Mn oxides and Li in varying proportions in the form of a spinel, e.g. $LiCoO_2$ coated onto an aluminium foil current collector [35]. The anode is made from carbonaceous materials, coated onto a copper current collector [11]. The separator, which protects the electrodes from shorting while allowing for ionic transfer is usually made of porous polymeric materials or fibres [36]. The parts described are either rolled or pressed together and an organic electrolyte is added, forming a working rechargeable cell. Finally, the casing of the battery is made of steel and/or plastic, depending on whether it is a cylindrical, button or a pouch cell [33].

The main contributors to the metals presence in the Li-ion cells are current collectors made of metal foils, and cathode active materials, which are convoluted chemical compounds, e.g. oxides or spinel minerals containing more than one metal in a compound, which require specific processing. While there are many valuable metals present in the batteries, current recycling methods struggle to encompass the diversity of the materials present as is discussed in the following section 2.2. Figure 2.1-2 represents the mass contribution of each of the elements of a typical high-energy Li-ion cell [11], while Table 2.1-1 and 2.1-2 show an exemplary chemical composition breakdown [15,22].

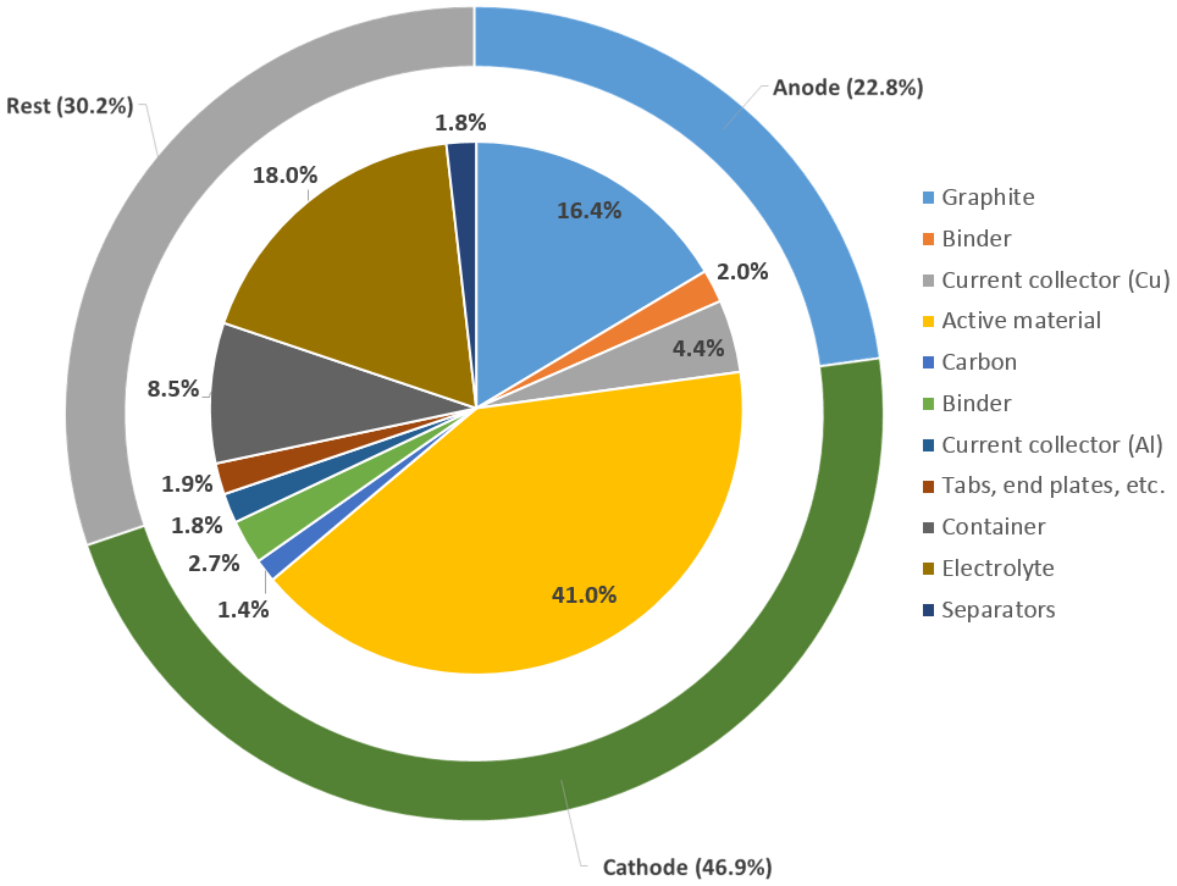


*Figure 2.1-2 Li-ion battery elements by mass. Cathode is the biggest contributor, similarly to the cost breakdown [11].*

*Table 2.1-1 Typical Li-ion battery elements breakdown [15,22]*

| **Battery component** | **Mass [%]** |
|---|---|
| | |
| *$LiCoO_2$* | 27.5 |
| *Steel/Ni* | 24.5 |
| *Cu/Al* | 14.5 |
| *Carbon* | 16 |
| *Electrolyte* | 3.5 |
| *Polymer* | 14 |

*Table 2.1-2 Li-ion battery by chemical compounds [15,22]*

| Battery component | Mass [%] |
|---|---|
| *Cobalt* | 5-20 |
| *Nickel* | 5-10 |
| *Lithium* | 5-7 |
| *Organics* | 15 |
| *Plastics* | 7 |

### 2.1.3. Alternative feedstock – biomass

Metal hyperaccumulation in plants is a growing subject, potentially useful for environmental biotechnology[37]. Additionally, it could be used for soil contamination removal, making it a metal-rich source. Methods used now are based on vitrification, excavation, soil washing/flushing, solidification or electrokinetic stabilisation systems. Alternatively, many plants capable of heavy-metal removal from the soil in an efficient way have been reported, including, but not limited to, fungi, wild plants and vegetables. For example, *T. Cearulscence* can accumulate Cd, Ni, Pb and Zn. As the plants accumulate the metal in its roots and shots, these can be later processed for re-extraction of the metal [37,38].

The process of metal extraction with a plant is called phytoremediation/phytoextraction, and occurs naturally and can be genetically engineered as well. This method works for soils with low and medium levels of metal contamination. Plants are planted (potentially on a large areas), harvested and after-processed (shots and roots). The plant can be then incinerated, providing a heavy-metal containing powder, while also producing heat.

As the method developed in this project is designed to work on various metal sources, it could also process the biomass feed. Therefore, plants used for phytoextraction could form potential feed for the metal recycling process, providing a feasible method for metal-contaminated soil restoration combined with valuable metals recycling. This is a very positive feature of the evaluated system, as its versatility allows enables work on not only battery waste and biomass feed, but potentially other metal sources as well. Such process adaptability would lead to easier feed stream management and therefore higher economic feasibility.

The process developed in this work is flexible regarding the feed and metals of interest, which makes it a fitting solution for a range of metal-rich waste streams, especially the

aforementioned eWaste and biomass. The method design would allow for processing of small particles, e.g. powders, as well as larger pieces, which would dissolve in the melt with time during the process. This allows for some flexibility in the feed preparation steps, enabling recycling of a finely ground electrodes active material, pyrolysed metal-containing matter or battery cathodes/anodes as a whole, without significant pre-processing.

## 2.2. Current metals recovery technology

As described in the previous section, Li-ion batteries are a multi-component system with a range of metals present in varying proportions, quite often locked in different forms or compounds. This poses a significant challenge for the recycling technology, as while the materials present in the battery require specific processing methods, they are not easily separated, unless a manual disassembly is included which can render the process unfeasible with the large amount of cells present in the waste stream. This results in multi-step recycling methods utilising costly and/or waste-generating environmentally adverse processes, as is discussed in the following section.

Metal recovery methods from multi-component materials are commonly divided into two groups; pyro- and hydro-metallurgical [14]. However, many of the methods employ features from both categories, especially for Li-ion and Ni-MH batteries recycling, and thus will be discussed jointly. The methods analysed differ in number of steps, waste preparation and the relation between hydro- and pyro-metallurgical parts. The recovery processes are mainly named after their inventors or company developing the method [14,39]. Figure 2.2-1 is a representation of a typical hydro-metallurgical recycling method.

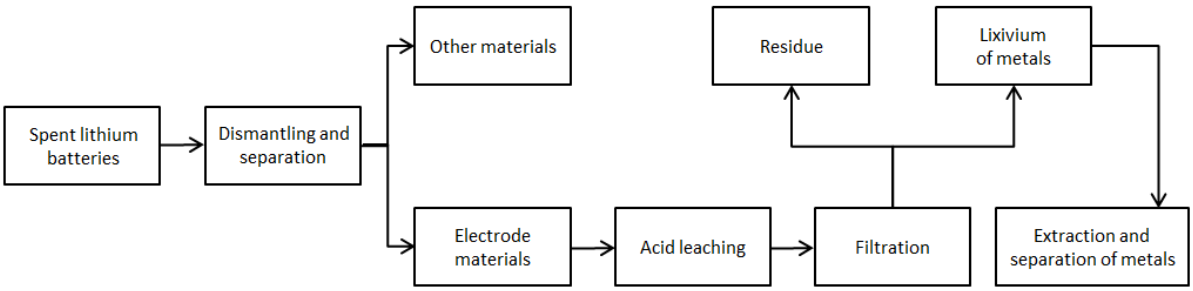


*Figure 2.2-1 Hydro-metallurgical recovery process of Li-ion secondary battery recycling. Adopted from* [39]

**Umicore process**

*Umicore* is a global materials technology company that uses a copper smelting process for valuable metals recycling [40,41]. Their technology is used to recover gold, silver, platinum group metals, and the battery metals from a range of waste feeds including electronics and used rechargeable batteries. The Umicore method is a highly integrated system including pyro- and hydro-metallurgical processing as well as electrodeposition. The general process flowchart is represented in Figure 2.2-2:

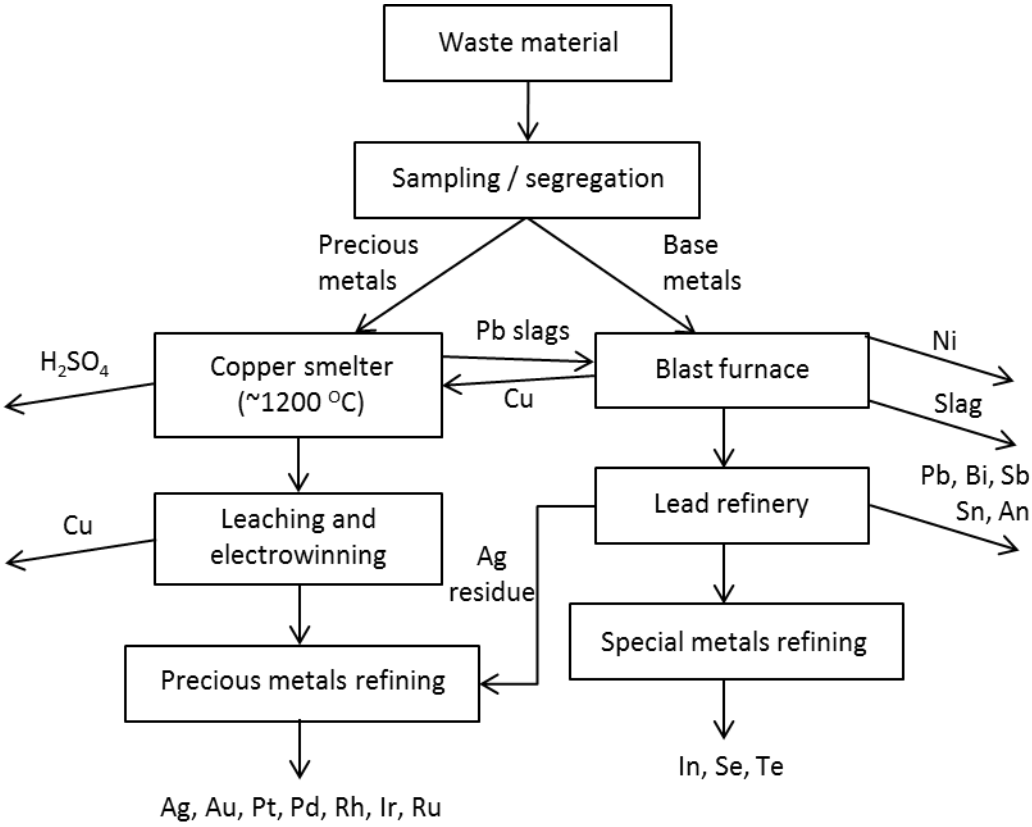


*Figure 2.2-2 Umicore recycling process.*

*Adopted from* [41]

The capacity of the Umicore facilities is significant, processing 250-350 kt of the waste materials yearly. They recover approximately 2 kt of Ni and 30 kt of Cu and other metals each year from a range of waste sources. The side products are mostly sulfuric acid and slag, where the majority components are aluminium, silicon and iron oxides. The gasses produced during the process need to be treated before releasing to the atmosphere, which is achieved using highly precise off gas treatment systems. The process is highly automated and proven profitable, however it is a very complex system requiring precise control on many levels and a large number of staff with a wide range of qualifications. Similarly to other recycling methods, Umicore also introduces the environmentally adverse leaching step, as well as a number of high temperature metal processing procedures.

**Inmetco process**

The Inmetco (*International Metals Reclamation Company*) method is a company-developed process used for metals recovery from battery waste among other sources [22,42,43]. It was not originally intended for battery recycling, and was repurposed to do so through inclusion of the battery scrap in its processing streams. Used Li-ion cells are treated together with iron-

containing materials to produce metal alloys, producing 11-kilogram metal ingots called "pig" later sold to the stainless steel industry. The batteries are sorted, the plastics are removed, the remaining metal parts is calcinated, distilled and then joined with other metal streams in the Rotary Hearth Furnace. The mix is then transported to the Electric Arc Furnace and the metal bars are cast. The produced metal contains up to 13% nickel and chromium. The Inmetco facility recycles around 72 000 tonnes of metal waste per year, with the spent batteries blended into the processing stream. Only copper and nickel are recovered from the li-ion cells using this method, the rest being slagged during the process. Slag recycling is a separate process, not considered in this review. While the process is cost efficient, it does not recover the valuable metals present to be re-used but rather alloys them, and large part of the metals ends up in a slag requiring post-processing. As was mentioned earlier, this method was not designed for the batteries treatment initially and thus is not optimised for it, treating the batteries as mixed secondary metal feedstock, which is sub-optimal when considering recovery of the valuable metals from the eWaste.

**Acid-leaching based methods**

Acid leaching methods are based on the use of strong chemical acids, and thus considered hydrometallurgical due to the significant amounts of water used. Metals are removed from the waste source, i.e. cell cathode, as a soluble salt by the leaching process, which is currently a very common approach in the Li-ion cells metal recovery methods. The solution usually used for this process is based on an inorganic acid and hydrogen peroxide, e.g. 4 M $H_2SO_4$ + 10% $H_2O$, 4 M HCl or 1 M $HNO_3$ + 1.7% $H_2O$ [44]. The leaching step takes up to 2 hours at the elevated temperature of 60-80 $^{O}$C. An exemplary leaching reaction (2.2-1) is shown [45].

$$4LiCoO_2 + 6H_2SO_4 \rightarrow 4CoSO_4 + 2Li_2SO_4 + 6H_2O + O_2 \qquad (2.2\text{-}1)$$

Precise control of the process parameters, i.e. temperature, concentration, solid content ratio and time, has a significant impact on the process efficiency. Shin et al. [15] studies acid-leaching methods as a potential option for battery waste management. It was reported that the particle size has a significant impact on the leaching efficiency, reaching over 95% for particles below 160 µm, or as low as 60% for bigger particles. The concentration of the metal (here: copper and aluminium) were relatively low, not exceeding 80 g $l^{-1}$ [15,39]. The leeched metal tends to create very fine and complicated structures in the solvent, which makes it difficult to separate metals in case of multi-component samples, and required additional post-treatment in order to recover the metals. This increases the time, cost and complexity of the

acid-leaching processes. Additionally, as the method uses water-based acid solvents, significant amounts of water waste are produced including the sulphates by-products contamination, which is considered extremely damaging for the environment.

**Mixed methods for electrode active materials recovery**

The mixed recycling processes composed of mechanical, hydrometallurgical, thermal and sol-gel processing steps are being studied as a way to recover lithium and cobalt from used li-ion cells, producing $LiCoO_2$ as the final product [39]. The lithium cobaltate powder produced can be ready to use for battery industry as the Li-ion battery cathode material. An example of such process has been reported by Lee et al [46]. The method described starts with thermal treatment and shredding of the li-ion batteries for the shredded pieces to be later sorted. Another thermal treatment follows and burning off the carbon and cathode binder to obtain the electrode active material for leaching in nitric acid using $HNO_3$ and $H_2O_2$. The resulting solution was used to produce an amorphous gel in a rotary vacuum dryer and later calcinated, producing the $LiCoO_2$ cathode powder to be used in batteries. Thermal pre-treatment element of the process is relatively simple; however, it produces significant amount of fumes, which require purification before being released to the atmosphere. Nonetheless, while such methods recover two of the elements present; cobalt and lithium, other metals are still not recycled in the main process, also constraining the method to one type of cell chemistry [47]. Figure 2.2-3 presents an example of the mixed method process flowchart.

The most environmentally detrimental and potentially costly step in this process is the acid leaching, as mentioned earlier, which produces considerable amounts of waste water, with aggressive chemicals required for the method to work. Strict solvent control has to be maintained, and the process complexity as well as the equipment requirements elevate the cost of the recovered material. In author's opinion, while the method is interesting due to its good efficiency of up to 85% and ready to use end product, it is lacking in the range of metals recovered and thus is not fully suitable for the growing and rapidly changing battery industry waste recovery.

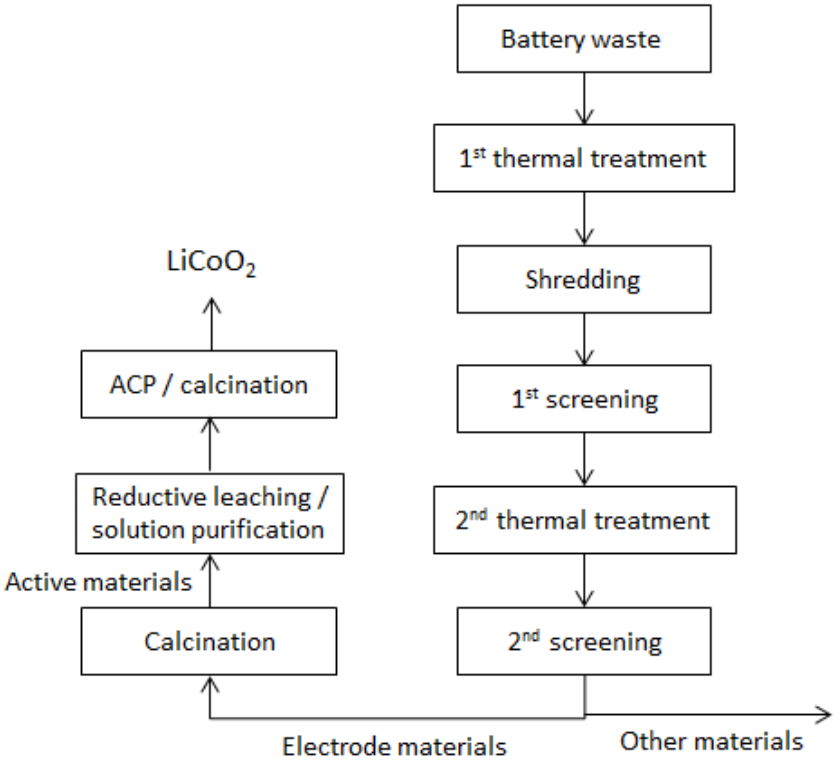


*Figure 2.2-3 $LiCoO_2$ recycling method flowchart.*

*Adopted from* [39]

**Mechano-chemical recycling methods**

A relatively simple method has been reportedly evaluated by M. Contestabile on a laboratory scale [16]. In this multi-step process, most of the metals present in the waste are recovered. Firstly, the batteries are opened and the active material is mechanically extracted. $Co_3O_4$ is then produced by means of thermal treatment, and then mixed with $Li_2CO_3$ which is another material recovered from the batteries, to form $LiCoO_2$ to be used as a cathode active material for li-ion cells production. Again, similarly to the previous case, this method is chemistry-specific and works only works with a selected type of li-ion batteries. Highly precise control of the process parameters is required as a high-temperature acid-solution is used as the solvent, producing vapours dangerous to health. Cobalt metal is recovered from the solution by pH variations, with good efficiency and quality of the recovered metal reported. Significant amount of filtration steps is of negative effect on the processing time and creates unavoidable valuable materials loss. As mentioned, this method considers only cobalt and lithium recycling, and does not offer a solution for the other metals in case of more complex battery chemistry. Being developed only on a small laboratory-scale, the scale-up of this method

might pose difficulties yet unknown. Figure 2.2-4 represents a flowchart describing the process.

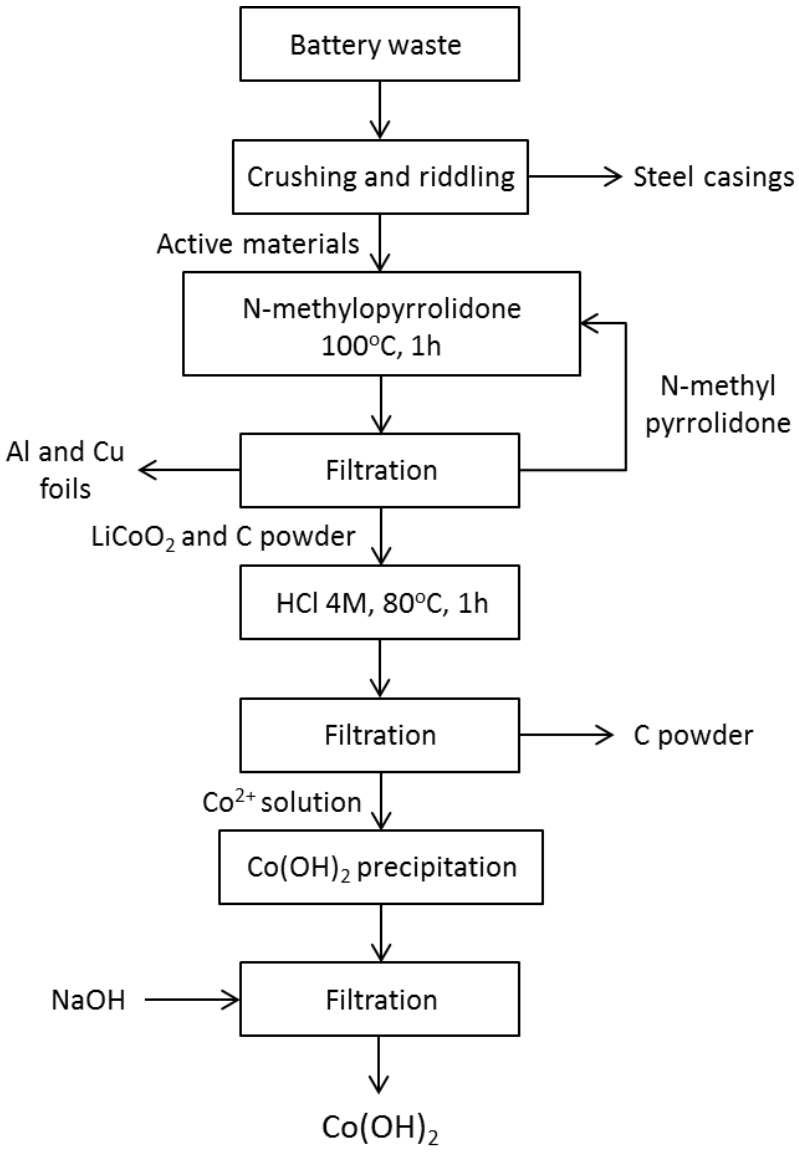


*Figure 2.2-4 Mechano-chemical laboratory-scale recycling method flowchart. Adopted from* [16]

**FFC Cambridge process**

Named after the three researchers of the University of Cambridge, where it was developed, the Fray Farthing Chen (FFC) Cambridge is a process that recovers titanium by reducing oxide scales or titanium dioxide powder pellets on titanium foils. The electrochemical cell used is shown in Figure 2.2-5. This process can be used to produce pure metal, or several metal alloys from mixed metal precursor, e.g. Ti-W [48] or Mo-Ti [49]. This method uses molten $CaCl_2$ salts as the electrolyte at 900-1100 $^{O}$C, carbon-based anode and the metal precursor as the

cathode. Cathode/precursor is then polarised to negative potentials versus the $Ni/NiCl_2$ reference, resulting in oxygen ions released into the melt, forming CaO, and subsequently pushing oxygen out of the melt to preserve balance re-forming Ca. Ca then diffuses back to the cathode to reduce another part of the oxide. The reactions occurring in the electrolyte would be as follows:

$$MO_x + xCa \rightarrow M + xCaO \tag{2.2-1}$$

$$xCaO \rightarrow xCa^{2+} + xO^{2-} \tag{2.2-2}$$

$$xCa^{2+} + 2xe^{-} \rightarrow xCa \tag{2.2-3}$$

$$xO^{2-} \rightarrow \frac{x}{2}O_2 + 2xe^{-} \tag{2.2-4}$$

Finally forming the net reaction:

$$MO_x \rightarrow M + \frac{x}{2}O_2 \tag{2.2-5}$$

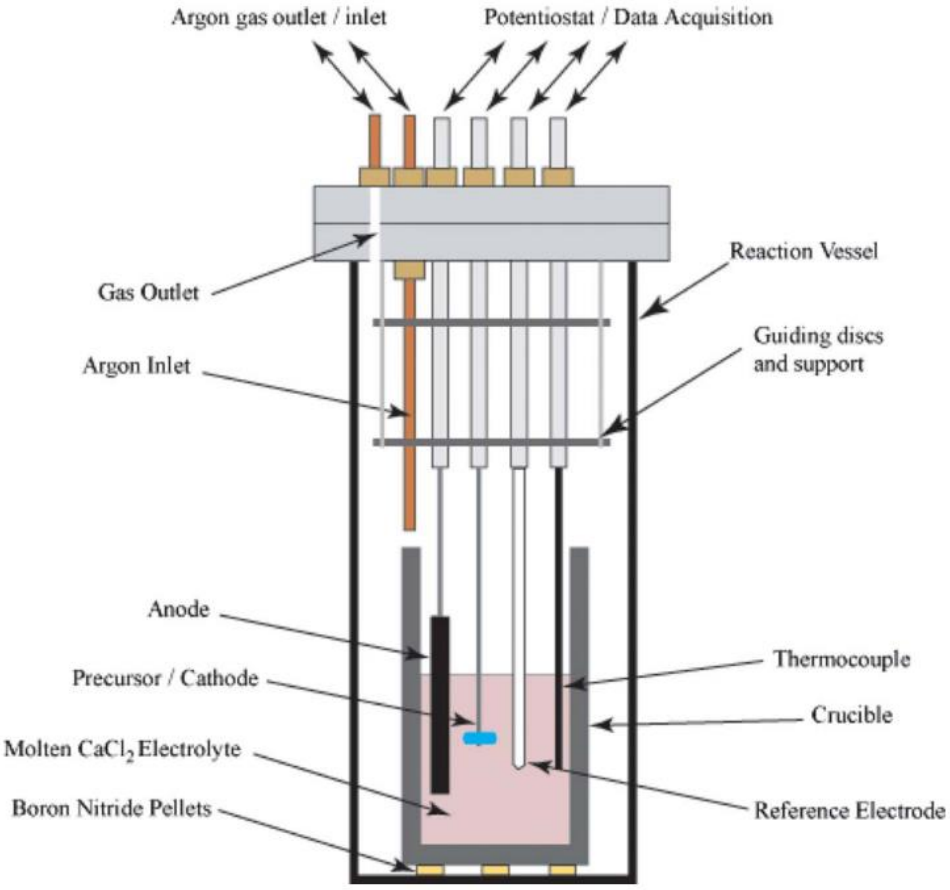


*Figure 2.2-5 Exemplary FFC Cambridge process laboratory scale assembly. The process reduces metal oxides (precursor on the drawing) into pure metal (Ti and alloys) in molten $CaCl_2$ electrolyte at 900$^{O}$C by means of electrochemical reduction. Adopted from [48].*

The cell and reaction schematics show that in this process Ca works as a carrier of oxygen ions, with the CaO as the intermediate specie formed during the process. This process requires precise atmosphere control, similarly to the previously discussed processes. The method described is a good example of how molten salt electrolysis processes can be used for electrochemical metal recovery from their oxides. Additionally, there is an option of valuable alloys formation, depending on the materials used as the precursor. However, this method has not yet been successfully up-scaled to the economically feasible scale.

### 2.2.1. Methods summary

The currently used methods for recycling of eWaste face a number of issues. Many of these processes are based on metallurgical technology, quite often repurposed mineral or metal processing methods. This limits the multi-component waste recycling capabilities, most often recovering one or two of the metals present. In example, lithium is not considered in the *Inmetco* process, and thus is completely lost during the waste stream processing. On the other hand, most of the methods purposely designed for batteries recycling are still in the early stage of the development, being tested only on a laboratory scale. Being evaluated in a clean laboratory environment with small amounts of waste of small diversity, it is unknown how these methods will handle a diverse waste material with a number of contaminations. The process efficiencies and quality of the deposits leave some room for improvement and vary depending on the metal recovered. Unfortunately, many of the methods are contamination-sensitive, e.g. pyrometallurgical methods are prone to have their efficiency reduced in case of carbon contamination, which is prevalent in battery industry. Similar issue exists with the acid-leeching methods, requiring precise pH control. Additionally, low concentrations of dissolved material are required for hydrometallurgical methods or otherwise the efficiency and yield can be significantly reduced, which in turn increases the amount of water waste produced, harmful for the environment. As a result, in order to recover most of the metals a number of steps must be introduced and combined, which increases complexity and lowers the cost-efficiency of the recycling process. Quite often, complex and expensive equipment is required to ensure the essential process control. Finally, as the battery chemistry is constantly changing and improving, recycling methods need to be modified and improved to handle the growing complexity of the waste stream [17,22,39]. The battery recycling methods are summarised by waste source in the Table 2.2-1.

*Table 2.2-1 Lithium-ion battery components recycling methods summary* [39]

| ***Waste source*** | ***Elements*** | ***Recycling method in use*** |
|---|---|---|
| Cell anode | Cu | Mechanical process |
| | C | Mechanical process, thermal treatment |
| Cell cathode | Co | Mechanochemical process, dissolution, thermal treatment, leaching, extraction, precipitation, electrochemical process |
| | Li | Mechanochemical process, thermal treatment, dissolution, leaching, extraction |
| | Ni | Mechanochemical process, chemical precipitation, electrochemical process |
| | Mn | Chemical precipitation |
| Electrolyte | Organic liquid | Thermal treatment, solvent extraction |
| Adhesive agent | PVDF | Thermal treatment |
| Current collector | Al | Mechanical process, acid leaching, chemical precipitation |
| Battery shells | Fe | Mechanical process, thermal treatment |
| | Plastics | Mechanical process |

To solve the issues described above (e.g. partial recovery, water waste generation), new recycling methods need to be developed. A uniform, scalable and flexible metals recovery process is required to address the growing industrial need for these metals, specific metals rarity and the largely monopolised rare metals market. Such a method would also need to offer minimalised waste output, as the disposal cost of contaminated water is growing, amplified by the pressure towards the green-technology approach and increasing governmental incentives towards cleaner production [50]. Additionally, as the eWaste stream is of increasing complexity and a significant metals variety is present, the method proposed would need to be able to recover a wide range of metals from diverse feed types. These objectives could be met by using molten salts electrodeposition systems, discussed in the next section.

## 2.3. Molten salts in (electro)-metallurgy

Many processes have turned away from the aqueous or organic environments towards molten salts, as they offer better chemical and electrochemical stability, as well as minimise the contaminated water output. Molten salts offer greater electrochemical window, the decomposition is less of an issue and their conductivity can be far better. However, there are issues with the higher operating temperature required and all the technological problems originating from that aspect, e.g. materials compatibility.

Molten salt processes encompass many of the major fields of and have found application in the areas of metals, materials and power [51]. Molten salts provide a diverse range of uses such as extraction [52], purifying [48], and/or coating [53] of metals, as well as carbon nano-materials production [54]. They also present good non-metal element retention, as is used in the steelmaking processes. On a particularly big industrial scale, molten salts are used in the basic oxygen steelmaking (BOS) process. In a steel refining process, steel is being molten under a very thick layer of slag in the aforementioned BOS converter. Metal droplets are ejected in the slag phase being pushed by a supersonic stream of hot gas. During the time metal spends in the slag, it is being cleared of phosphorus, and returns to the metal phase cleaner after the so called "retention time". Metal refining in this way is possible due to a high phosphorus partition coefficient between the salt and the metal [55].

A number of electrochemical processes require anhydrous environment. This may be due to the water-sensitivity of the product, to make the process cleaner, more efficient, or because the water readily reduces outside of a small electrochemical stability window. For such purposes molten salt systems are designed, eliminating the aqueous systems limitations. An exemplary case is the *Hall-Herolut* process [51], which is an industry-scale process of producing aluminium by electroplating in a molten sodium hexafluoroaluminate, more widely known as cryolite.

### 2.3.1. Molten salts definition

Molten salts are defined as salts that would be solid at the standard temperature and pressure, but due to the elevated operating temperature of the system considered, they are in a liquid phase. If the electro-negativity of the M-X pairs (where M is metal and X is another chemical element) is large the system is considered ionic, which is true in case of molten salts and so they are classified as a sub-system of ionic liquids. Temkin's activity model [56,57] describes

molten salts using mathematical relations for ideal systems, defining the activity of the molten salt elements with the following equation 2.3-1:

$$a_{MX} = \frac{M^{+}\ moles}{Moles\ of\ all\ cations} \frac{X^{-} moles}{Moles\ of\ all\ anions} \quad (2.3\text{-}1)$$

The molar free energy of mixing for such systems can be described by equation (2.3-2):

$$\Delta G_{mix} = \Delta H_{mix} - T\Delta S_{mix} = RT \sum_i N_i ln a_i \quad (2.3\text{-}2)$$

where: *a* is the activity, *N* is the molar concentration of the component *i*, while the rest of the terms hold their usual physical meaning.

The model properly describes fully ionised systems (e.g. molten halides [51]) and is commonly adopted due to its relatively simple application. However, molten metal oxides exhibit a strongly non-ideal behaviour due to their much smaller electronegativity differences between the elements. This results in a covalent character present in the bonds between the ions [58], which in consequence enables oxygen bridging creating a polymeric structure in the melt [59]. This case is relevant to the borate salts used in this work, as well as to the whole range of slags used in metal industry [60]. Such a structure results in a non-random ordering of the ions in the melt, negating the assumptions of the Temkin's model. Deviations from ideality are quite significant and other models are relevant instead.

Gaskell [61] described the non-ideal solution as one with activities unequal to the elements mole fractions, by introducing the activity coefficients:

$$y_i = \frac{a_i}{X_i} \quad (2.3\text{-}3)$$

where: *y* is the activity coefficient, *a* is the chemical activity and *X* is the molar fraction of the *i* element.

Further deviations from ideality are described by regular and sub-regular expansions, allowing for non-zero enthalpy and random or non-random entropy of mixing respectively, through power series expansions [56]. The coefficients in the expansions are empirical and need to be determined experimentally for the given system under evaluation. Still, these models fail to properly describe systems that exhibit strong structural ordering even in case of a large numbers of terms included. Such systems can be defined by quasi-chemical models, described by Guggenheim [62]. A quasi-chemical model can be derived for each considered system;

however, construction of such a model is non-trivial and is not the subject of this work. Molten borates chemical properties, their network structure and interactions with other metal oxides are described in greater detail in a following section.

### 2.3.2. Borates

Borate salts are of high interest to industry, mainly used in boronation [63–65] and glass forming [66,67], where they also show the capability of dissolving significant quantities of metals. However, the thermodynamic properties are not yet well understood and literature evaluating their behaviour is sparse. The high metal affinity of borate salts has been evaluated by Williams et al. [23]. In their paper a method of metal extraction from waste using borates is suggested. In the system described, waste feedstock is melted and dissolved in a molten borate solvent. All organics are pyrolysed, moisture evaporates, and impurities are dissolved. As a side effect of such systems liquid metal in the molten slag materials can experience an undercooling phenomenon before solidification [68]. It has been reported to work efficiently as an extraction method for Nd (over 25 wt% solubility) and Sm (over 58 wt% solubility) while using scrap metal (i.e. magnets) as an input [7,21]. Recovered metals can be subsequently extracted by electrochemical reduction [69]. Further work on other valuable metals such as Co has been suggested [21]. Borates inherent high resistance to water and other pollutions enables the processes to work under atmosphere in an open crucibles, which further makes the process easier and more viable [70]. These properties provide a good grounding for molten salt based metal recovery processes.

#### 2.3.2.1. Metals solubility in borates

A solution can be defined as a homogeneous mixture of two or more components [71]. Mixture formation introduces the Gibbs potential of mixing, in its basic form represented in the equation 2.3-2 as described earlier. In the simplest case the solution can be described by the Raoultian ideal model, in which the particles are assumed to not interact, the ions distribution is random and the enthalpy of mixing to be zero. In consequence the activity of the components is equal to their mole fraction. Because of the simple mathematical relations and feasibility, models based on ideal solutions are commonly used and are a part of the Temkin model [72,73], widely used to describe the thermodynamics of molten salts.

However, it is known that activities of the components deviate from being equal to the component concentration. Furthermore, the molten salt is an array of positively and negatively charged cations and anions, which due to strong Coulomb repulsion between ions of the same

sign, they have a preferred site, rather than a fully random distribution. This tendency of ordering is not the one of ideal solutions, nor of the regular solutions model that, while allowing nonzero enthalpy of mixing, still assumes a random distribution of ions, an assumption which has been proven not correct for our case when discussing the borate molten salts strong ordering abilities in the previous section. A model most closely describing the molten borate salt system is the quasichemical model of Guggenheim [62], which is a physical model for thermodynamic properties of ordered systems. A quasichemical model can be created separately for each considered system, which is however non-trivial and thus rarely used. Solution models are compared in Table 2.3-1 [56].

*Table 2.3-1 Solution models used to describe interactions in liquids. Temkin model is an example of an ideal model, while more complex models, e.g. Quasichemical model needs to be developed specifically for each system.*

| Model | Ordering ($\Delta S$) | Enthalpy of mixing ($\Delta H$) |
|---|---|---|
| Ideal | Random | 0 |
| Regular | Random | $\neq 0$ |
| Subregular | Non-random | $\neq 0$ |
| Quasichemical | Non-random | $\neq 0$ |

As tested by Williams et al. [23], borates show relatively good solubility for multiple metals, like Ni, Mg, Fe, Zn, Pb, Ca, Sr and Ba, providing good ground for metal-solution based processes. The system evaluated was based on NaCl-$Na_2O$-$B_2O_3$ composition, which formed a two-phase setup. The lower (borate) phase provided good solubility of metals which took the most thermodynamically stable form, which in this case was of metal oxides.

In the system coupled with chloride salt, metal distribution coefficients varied depending on the specific metal evaluated and the salts composition. The partition process thermodynamics are considered in the further part of this dissertation. During the dissolution process, no special precautions needed to be taken, neither water vapour removal nor special atmosphere. Instead an open crucible can be used, which shows the feasibility of this solution. It is suggested that borates can be used as a good extraction agent for a range of metals.

Molten slag materials can also be used to extract metals from alloys by the so-called glass-slag method. Saito et al. [74] successfully extracted Nd from Nd-Fe-B alloys, leaving less than 0.01 % of Nd in the alloy. The amount of Nd carried by borate glass exceeded 25 wt%. As the

metal took most thermodynamically stable form in borates, by means of chemical reaction neodymium formed oxide – $Nd_2O_3$. It is also suggested that Co can be easily extracted by the same method.

Similar approach was tested by Saito et al. [75], in regard to Sm-Co alloy, as well as Nd-Fe-B alloys, called rare earth metal magnets. By the time Sm amount in borate reached 58.28 wt%, its amount in the alloy was reduced to <0.05 wt%. The method was found suitable for the extraction of samarium and neodymium. This experiment was supported by the need of better method when compared to leeching, which creates significant amounts of waste water as was described earlier.

Fluxing in molten borates is proven to work well as a processing method for a range of metals, allowing to form alloys or undercool metals using such system. Xiao et al. experimented with Cu-Ni alloy in anhydrous $B_2O_3$, analysing melting, undercooling and crystallisation behaviour. Due to the differences in density, metal alloys go under the borate flux, causing full immersion and complete coverage with borate layer. This way many impurities as well as metal oxides can be easily dissolved in borate salts [74,76].

Alkali metals when introduced to borates are called *glass network modifiers* due to their influence on the structural forms in the network, changing slag properties and behaviour. Sodium borate is proven to be of good use in metal extraction and potassium borate present similar physicochemical properties, thus can be used in similar manner. Calcium borate, on the other hand, due to the calcium cation, form different crystallographic forms diminishing many of the alkali borate positive properties [23,77–79]. Therefore, sodium and potassium borates have been considered for the needs of this project, as will be described later.

The different metals solubility shown by various alkali borates is believed to be originating from the influence of the alkali metal oxide, e.g. $Na_2O$ on the boron oxide melt, as has been described by Rowell [59]. As the structure of liquid $B_2O_3$ is still not fully evaluated, it is theorized to be polymeric, not fully ionised. It is known that an addition of alkali oxide

imposes the oxygen atom on the network, resulting in the following change represented in Figure 2.3-1:

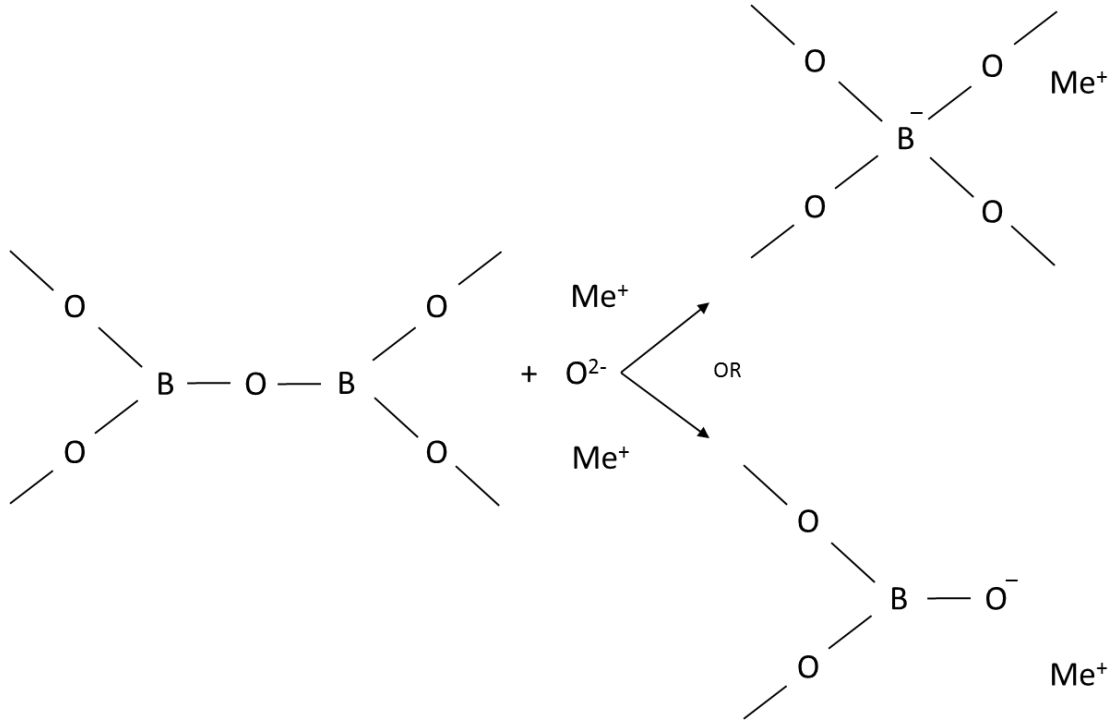


*Figure 2.3-1 Boron oxide network modified by the alkali metal oxide.*
*Addition of the modifier results in an increase in te positive exchange sites,*
*which results in higher metals solubility in the melt.*
*Adopted from* [51].

Such a structure causes an increase in the negative exchange sites present in the salt, with the borate phase acting like a liquid cation exchanger. This influences the metal cations affinity and the partition coefficient in case of more than one phase, which will be described later in greater detail. These effects seem to peak with 20-30 mol% of $Na_2O$ in the borate phase, due to the so called *borate anomaly* [23,59,77], described in section 2.3.2.6.

Utilising the metals solubility capabilities, borates are most commonly used as a glass-forming material, mixed with different metals for the optical and mechanical purposes. It is well known that adding alkali metals to the borate glass improves its resistance, but also decreases the viscosity and melting point [80]. While the glass-forming side of the borates has been quite deeply studied, not much beside it has been looked into [81–86]. As a result, there exist some information about individual metals solubility in borates, though mostly in regard to borate glasses, unrelated to metallurgy, and thus not focused on the reliability of this medium for metal industry processes. Based on the thermodynamical data of the species, simulations of

specific elements behaviour in molten borates can be modelled, filling some of the data lacks in this field. However, phase diagrams based purely on thermodynamical modelling and estimated data need to be validated in order to prove true, yet they can be used as a starting ground or supporting points of assumptions for experimentation if no other data is available.

#### 2.3.2.2. Phase simulations - binary plots

Using the FactSage™ chemical thermodynamics modelling system [24], with the most up-to-date available databases models and values, probable thermodynamic behaviour of the evaluated compounds and mixtures were plotted. Attention was focused on the limiting concentrations of metals in borate salts, their solubility and phases they might form. The phase diagrams created were analysed for a better understanding of processes that might occur, and to establish starting points for the experiments to follow, especially the melting temperatures of the systems evaluated and the metal solubilities assessed in order to establish a minimal amount of metal required for limiting solubility testing. However, there are big gaps in thermodynamic data about the species considered and some plots are incomplete and lacking. The created phase diagrams are presented in Figures 2.3-2 to 2.3-8 and analysed below.

The diagrams presented in Figure 2.3-2 and 2.3-3 show respectively potassium and sodium borate behaviour depending on the temperature and their composition. A number of points can be deduced from these plots. The melting temperature appears as low as 325 $^{O}$C for $K_2O$ and $B_2O_3$ in optimal ratio, and still quite low, down to 450 $^{O}$C as lowest possibility for $Na_2O$ and $B_2O_3$ eutectic. There is a distinct lack of information about the potassium oxide – boron oxide system is shown as straight lines of liquid formation are very unlikely. Instead, curved lines should be plotted representing more probable thermodynamic behaviour, as presented in the figure. This shows significant lacks in the thermodynamic data contributing to the databases regarding the systems evaluated. Finally, sodium borate is capable of forming significantly higher number of complex phases, which indicated that it would be a more problematic system to work with due to the diversity of possible reactions and thus potassium-based mix should be sued if possible.

Considering the process evaluated in this work, the most widely accessible potassium and sodium borates are $K_2O$-$2B_2O_3$ and $Na_2O$-$2B_2O_3$. While the melting temperature of potassium borate in this composition is relatively low at ~400 $^{O}$C, the sodium borate, or *Borax* compounds remains solid below 750-800 $^{O}$C. To avoid local precipitation and viscosity issues, process temperature of 900 $^{O}$C was used, as is explained in a later part of this thesis.

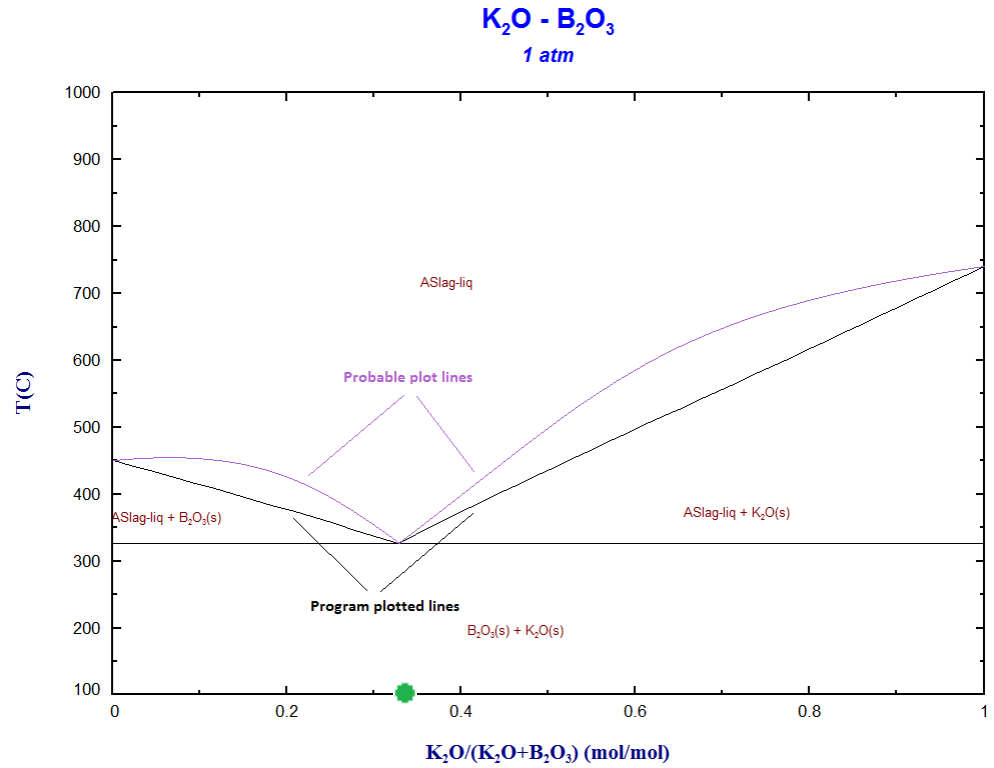


*Figure 2.3-2 Phase diagram for $K_2O$ - $B_2O_3$ mix. The difference between the program-calculated (black) and thermodynamically-probable (violet) lines is caused by the lack of experimental data. $K_2O$-$2B_2O_3$ is marked with a green dot.*

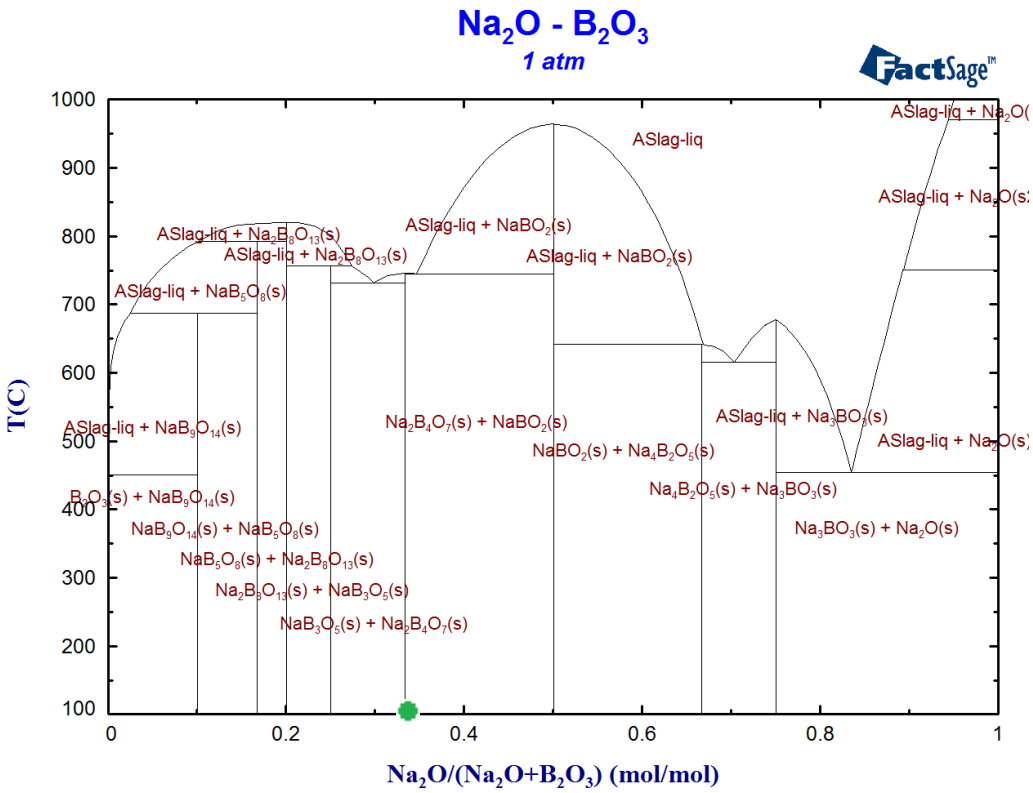


*Figure 2.3-3 Phase diagram for $Na_2O$ - $B_2O_3$. $Na_2O$-$2B_2O_3$ is marked with a green dot.*

Using the same method, non-alkali metals solubility can be plotted in order to estimate the expected dissolved metal amount in the molten salt. These specific metals considered as to the best of the author's knowledge were not evaluated in the literature at the time of writing, therefore the presented graph are plotted base only on the ideal-solution models [24]. The values need to be evaluated experimentally in order to confirm actual solubility values and enable comparison with the theoretical calculations. However, plotting of these values will be used as a starting point for the testing when considering the amounts of feed required to achieve optimum concentrations or assess limiting solubilities.

Cobalt oxide solubility in borate molten salt is presented in the Figure 2.3-4. It is of a considerably high value, reaching more than 30 mol% at 900 $^{O}$C. The plotted slope is steep, which indicates that the system would readily precipitate the metal oxide in case of the temperature change. On the other hand, slight increase in temperature can increase the solubility considerably, allowing for some flexibility if the need arise.

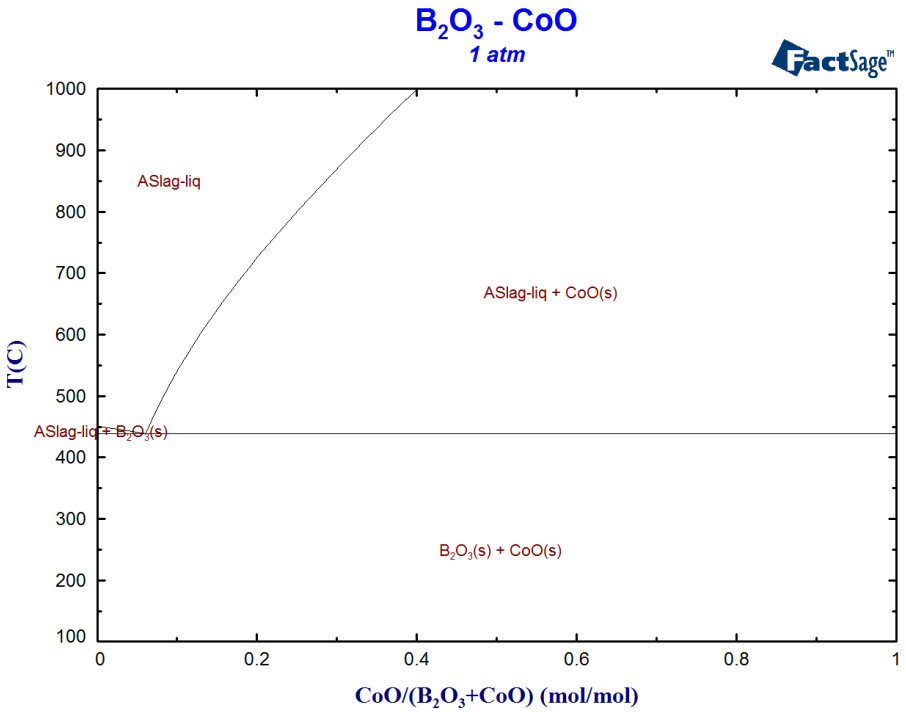


*Figure 2.3-4 Phase diagram for CoO in $B_2O_3$*

Phase diagram shown in the Figure 2.3-4 suggests that the copper oxide solubility is minimal up to around 1600 $^{O}$C. Additionally, the phase diagram slope is relatively steep up to around 2000 $^{O}$C, suggesting that there will be no significant solubility increase in that temperature region. This is a relatively poor solubility, i.e. when compared to cobalt oxide case.

Copper and manganese oxides, Figure 2.3-5 and 2.3-6 respectively show similar behaviour, while nickel phase diagram, shown in Figure 2.3-7 resembles the cobalt case. As presented on the plots, some of the metals considered show quite good solubility; however, not all of them. Nickel oxide and cobalt oxide can be dissolved in reasonable amounts while still at a relatively low temperature. To ascertain sufficient solubility in all cases, addition of alkali metal oxide would be in order since, as explained earlier, alkali metal oxides (e.g. $Na_2O$) change the polymeric structure of molten borate increasing the number of negative exchange sites. This in turn improves the metal cation affinity towards the borate network. Such a change would promote the metal solubility in the borate phase, potentially improving the efficiency of the system for the purpose of metal recovery.

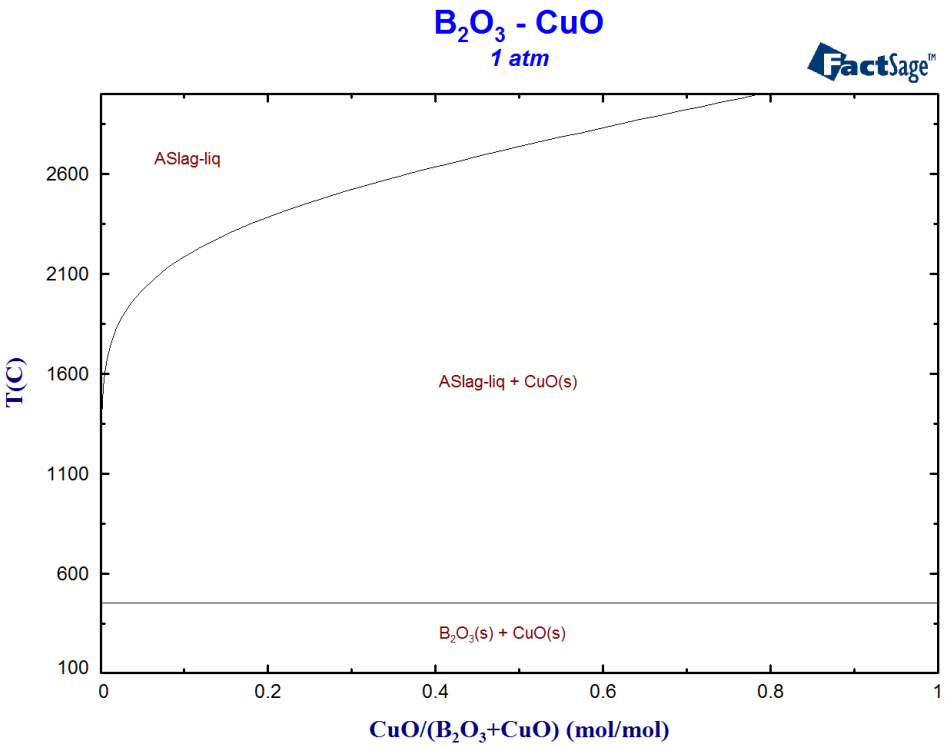


*Figure 2.3-5 Phase diagram for CuO in $B_2O_3$*

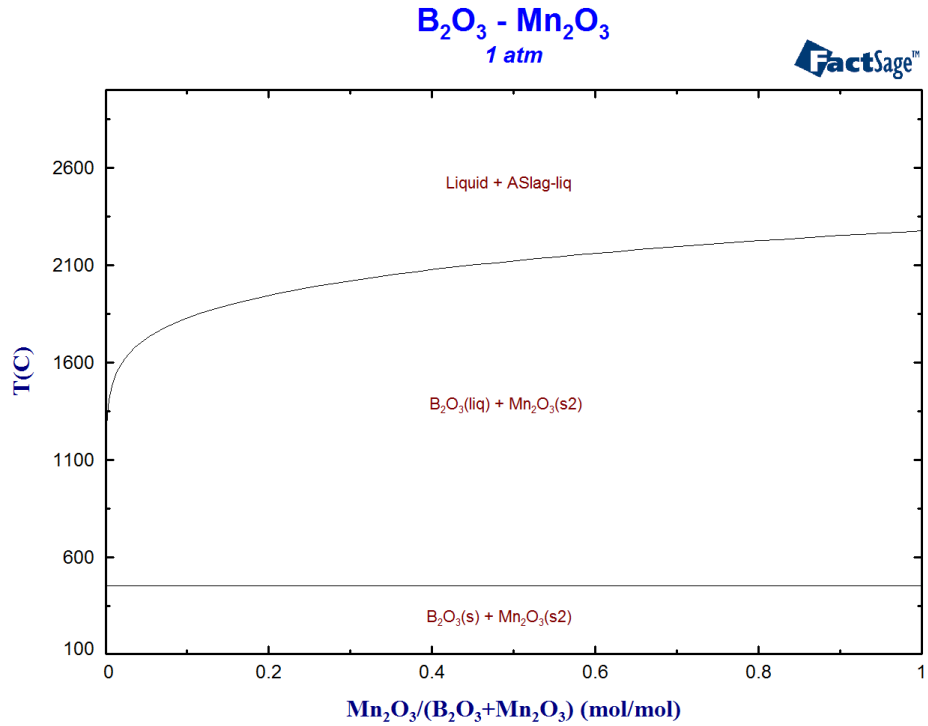


*Figure 2.3-6 Phase diagram for $Mn_2O_3$ in $B_2O_3$*

As a point of notice, the lithium phase diagram presented in Figure 2.3-8 is lacking essential thermodynamic data, as it is not forming any mixed phases, despite such being experimentally proven [67,84]. Some other metals, like niobium, were unavailable for this modelling due to the insufficient data in the databases accessible at the time of writing. The reason of such is that these metals appear to have been of little interest to the scientists who evaluated the considered molten salts systems, most often focused on the glassmaking industry. This indicates that more testing is essential for the understanding of the thermodynamics of these systems. Therefore, knowledge gap has been identified, and could be filled with this work's experimentation benefitting the molten salts knowledge base.

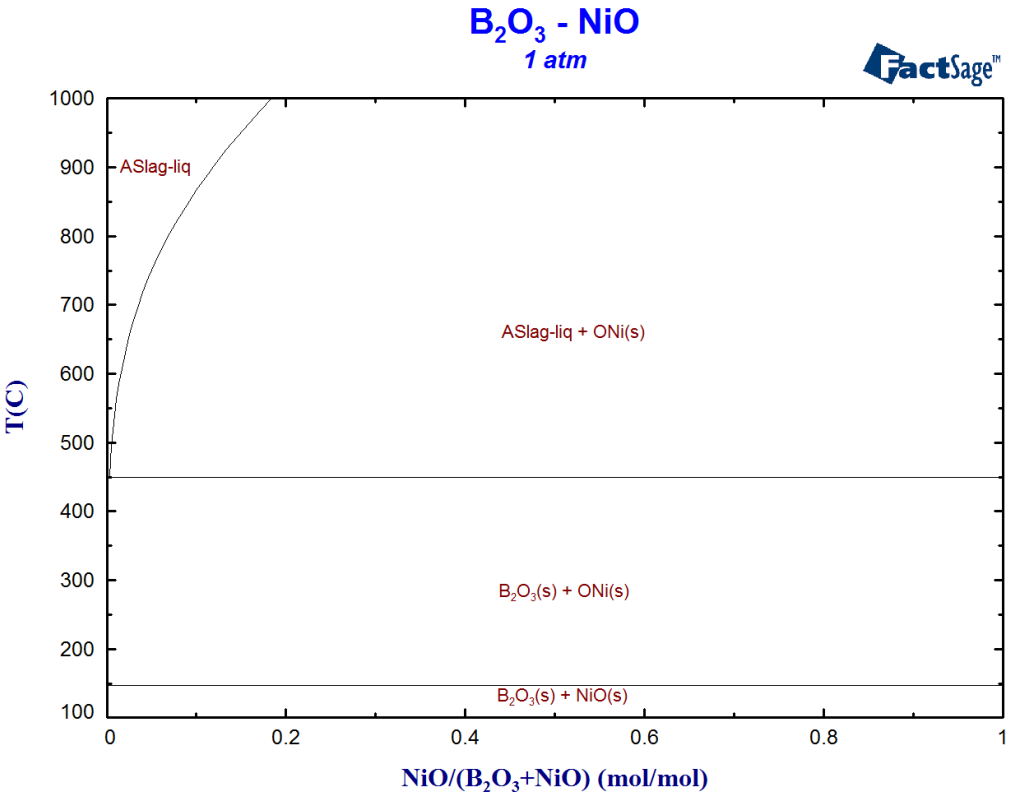


*Figure 2.3-7 Phase diagram for NiO in $B_2O_3$*

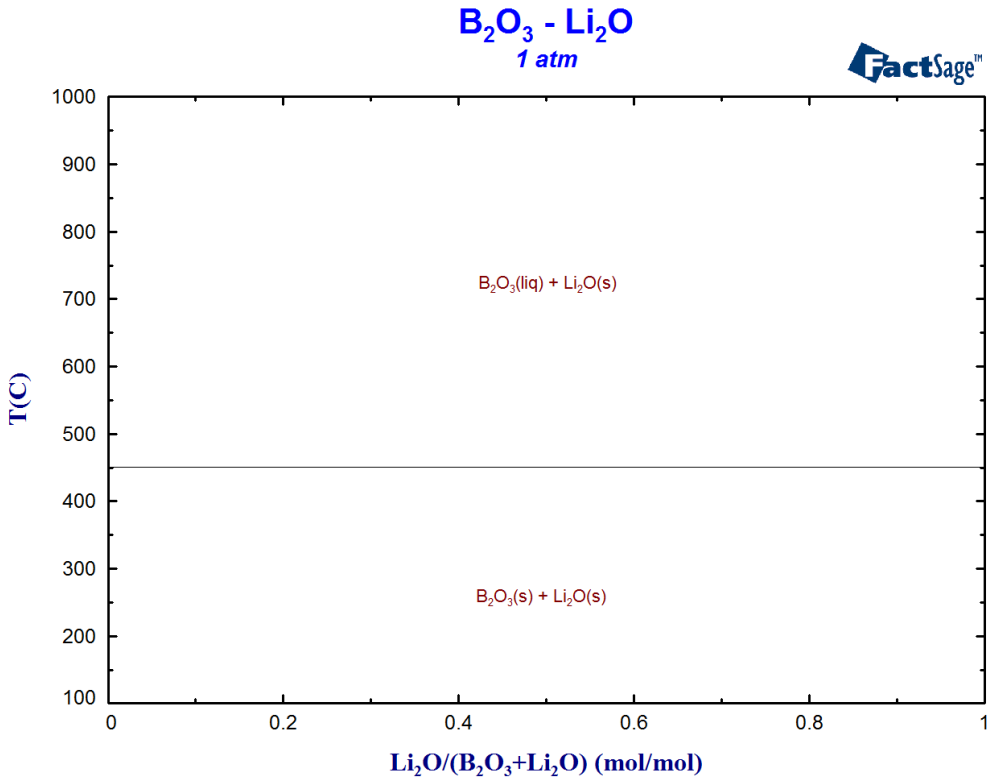


*Figure 2.3-8 Phase diagram for $Li_2O$ in $B_2O_3$*

### 2.3.2.3. Phase simulations – ternary plots

A ternary plot called a *triangle plot* or *de Finetti* diagram is a barycentre presentation of three variables. Such plots are based on equilateral triangles and created by plotting the possible phases stable in the system evaluated, while considering concentration of three elements or compounds in the mix, which sum must always equal 100%. Subsequently, constant temperature lines are added – isotherms that indicate the precipitation temperature for each phase, as indicated by the (s) subscript next to the compounds label. Each phase stability region is calculated by Gibbs energy minimisation [24,87]. Ternary plots can be used to observe or model more complex set-ups. The variables of interest for this research are molar concentrations of three components of the molten liquid. The components can be either pure chemicals, e.g. Na or Cu, or compounds, like $Na_2O$ or CuO. In case of a system with three constituents and constant pressure, temperature relation needs to be plotted as a projection. Interpretation of such plots does not differ much from basic plots, and gives us information about relative concentrations of three species and phases formation in relation to temperature, same as the binary plots. The difference is that in case of ternary plots there are three species changing in concentration, as well as the temperature, presented by the coloured contours. The modelling of a ternary plot is more difficult and requires more complete datasets. Below are presented some of the ternary plots for the system evaluated in this project.

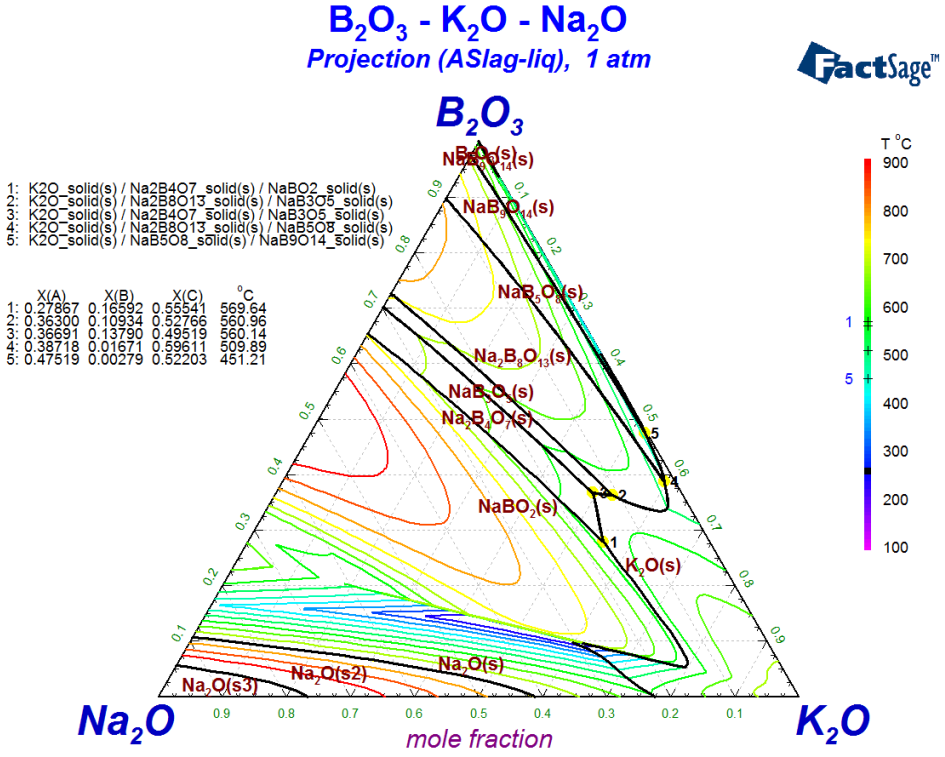


*Figure 2.3-9 Ternary phase diagram for $Na_2O$ and $K_2O$ with $B_2O_3$ (potassium borate)*

As shown in the Figure 2.3-9, a system with mixed potassium oxide and sodium oxide with boron oxide shows similarities to those systems put separately (Figure 2.3-2 and 2.3-3). Sodium causes the system to form a lot more complex phases, increasing the diversity of possible phases. Melting temperatures of most of these forms are below or close to 900 $^{O}$C, represented by the red isotherm on the plot, making it a relatively low melting point system. Additionally, potassium-dominated area of the plot shows that potassium oxide phases are of lower melting temperature than the sodium ones. Five triple points can also be spotted on the plot, marked by the yellow dots, between 400 $^{O}$C and 600 $^{O}$C. In order to evaluate further, simulations of potassium and sodium borate mixed with other metal oxides were evaluated, resulting in the following Figure 2.3-10 to 2.3-13.

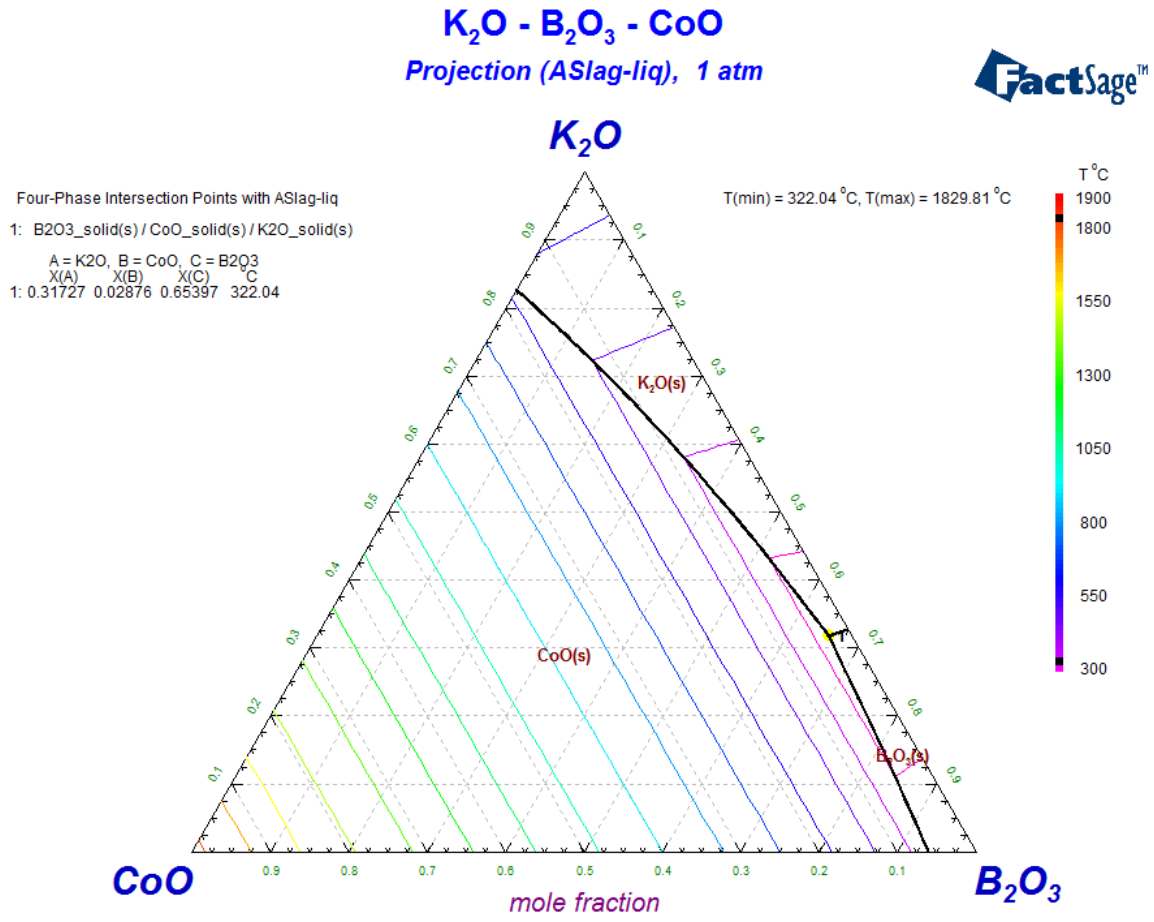


*Figure 2.3-10 Ternary phase diagram for CoO with $K_2O$ and $B_2O_3$ (potassium borate)*

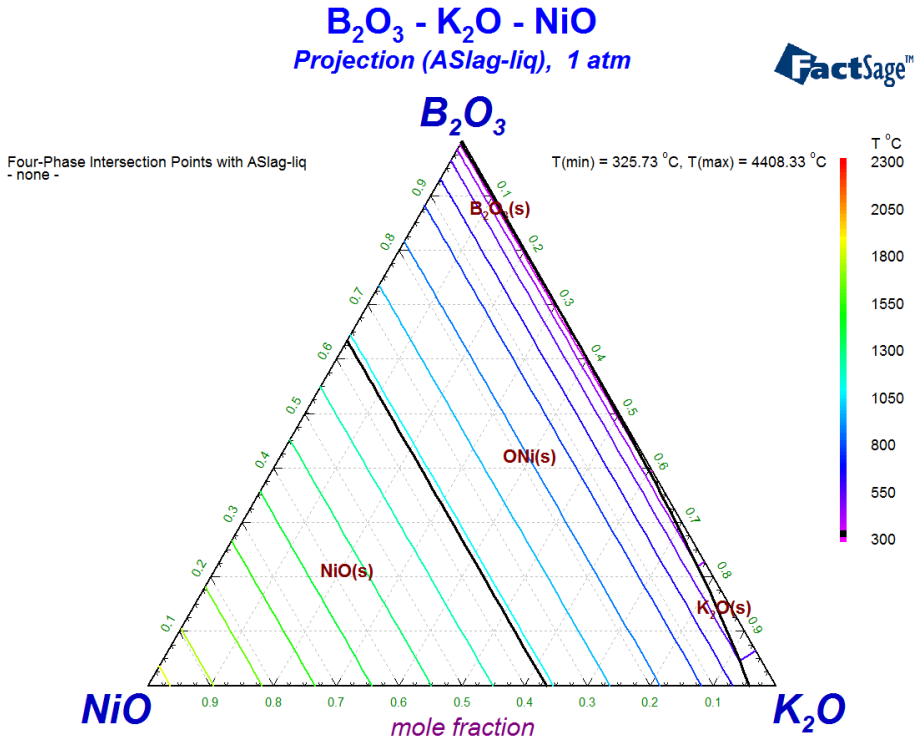


*Figure 2.3-11 Ternary phase diagram for NiO with $K_2O$ and $B_2O_3$ (potassium borate)*

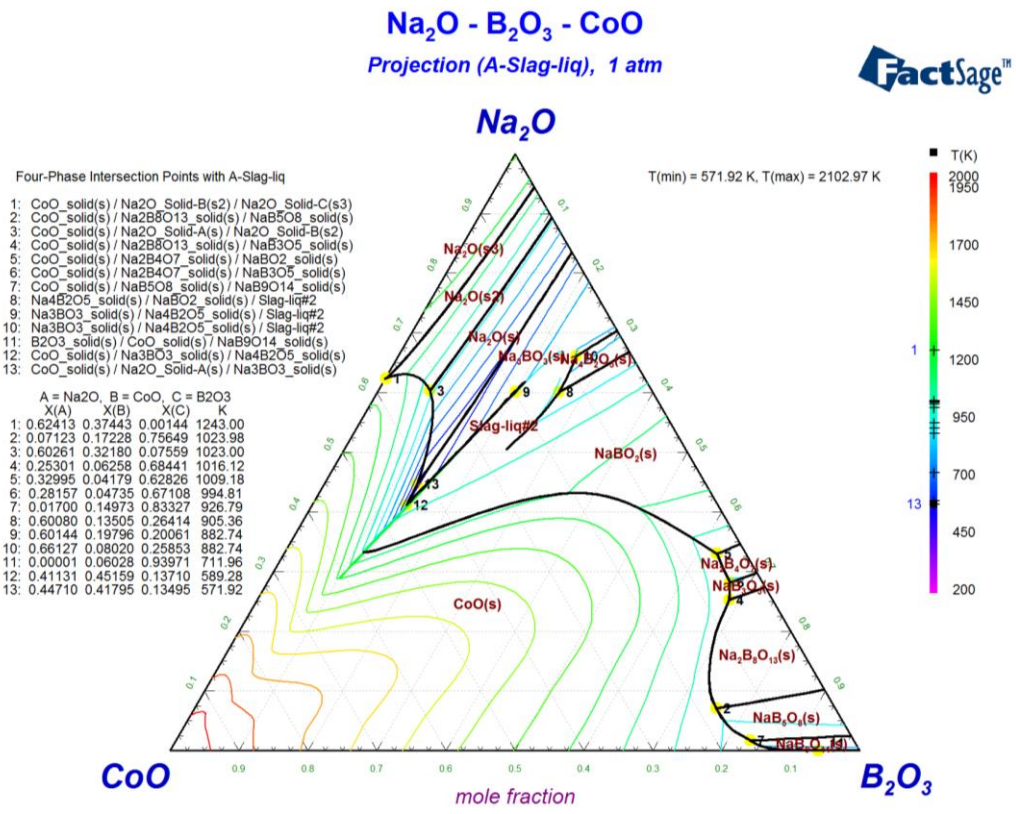


*Figure 2.3-12 Ternary phase diagram for CoO with $Na_2O$ and $B_2O_3$ (sodium borate)*

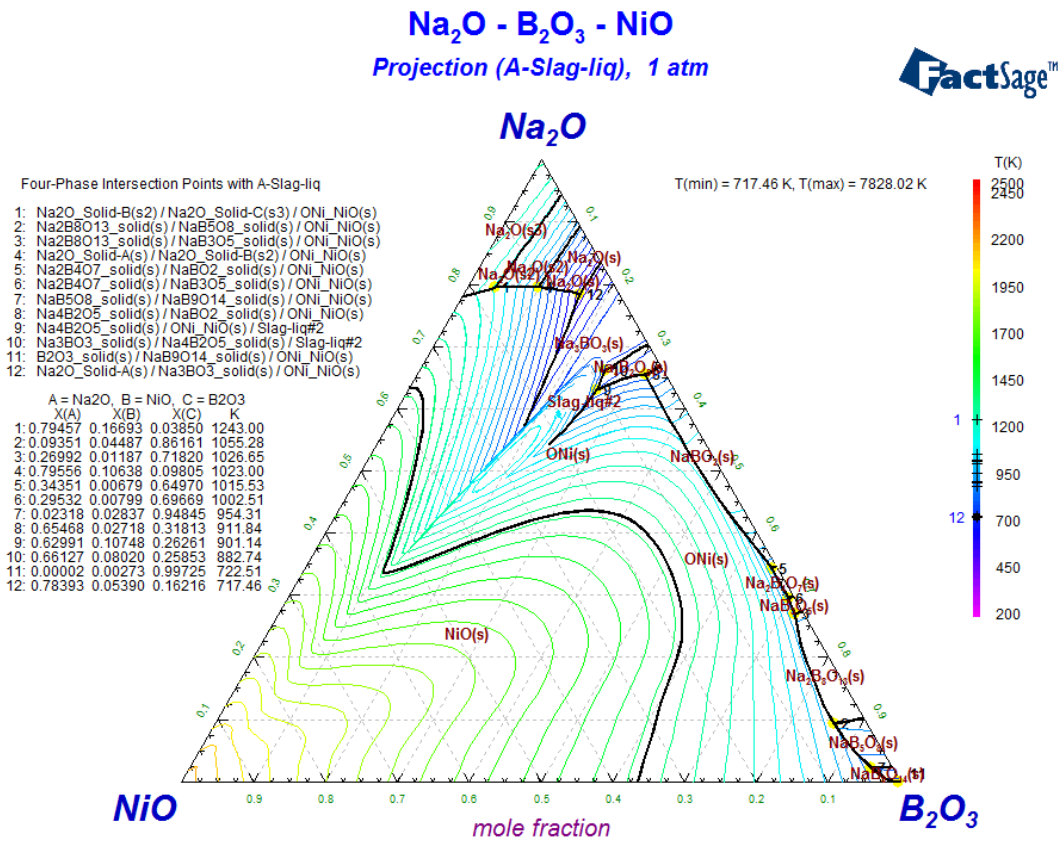


*Figure 2.3-13 Ternary phase diagram for NiO with $Na_2O$ and $B_2O_3$ (sodium borate)*

The plots presented are of the combinations that the databases were available for, while CuO and $Mn_2O_3$ data sets were lacking to the point of being unable to calculate a ternary phase diagram. The plots presented above suggest that the metal oxides behave comparatively in binary and ternary systems in case of boron oxide based salts. Solubilities and phase-temperature dependencies are shown as close to the binary models, e.g. under 900 $^{O}$C solubility of cobalt oxide in potassium oxide is over 30 mol%, and there is no influence from the amount of potassium or sodium oxide dissolved in the melt. However, it has been already mentioned earlier in this section that the alkali metal oxide presence can significantly change the solubility behaviour, potentially more than indicated by the plotted phase diagrams. Because of the lacks of data in the databases, copper, manganese and lithium oxide plots were invalid, which renders them unusable and shows a gap in the knowledge. It shows possible and necessary experiments, which needs to be conducted in order to provide full picture of metals behaviour in the systems being evaluated.

The author underlines that these are only simulations based on thermodynamic calculations, and need to be validated. The main errors are attributable to the lack of thermodynamic data

resulting in the phase diagrams being based on the ideal solution models. Some mistakes may occur due to the round-off error and/or estimation of values, as the database fitting is inherently complicated and subjective so can be very different depending on the style of the database builder. Gaps in data need to be filled with the values gathered during experiments, also making it easier for future phase diagram plotting of the considered systems, filling the identified knowledge gap for the befit of the molten salts research. Experimentation regarding these values will follow in the experimental section, with the methodology built using the analysed phase diagrams as the starting points of the experimentation and the operating temperatures selection.

#### 2.3.2.4. Borate glass

Borate glasses are of great interest to the industry, thanks to their optical properties and thermal resistance, as well as the number of possible modification and combinations. In the glassware industry, some research has been conducted mostly regarding optical properties of the product, as the influence of metals on light-changing features and crystallographic forms has been evaluated. While this project is not focused on the optical or thermal properties of the borate glass, the metal solubility and thermodynamic behaviour data is of use for the needs of the process developed. Some of the results are presented below, with focus on alkali and rare metals used in the glass-making process. The data on metals solubility is gathered while investigating glass properties, while not the primary focus of the reviewed papers, is of interest due to the information on metals solubility and influence on the borates properties.

- Manganese and vanadium borate glass

Ilonca et al. [88] managed to create manganese and vanadium borate glass: $x(MnO{\cdot}yV_2O_5){\cdot}(1\text{-}x)[2B_2O_3{\cdot}K_2O]$, where x ranges from 0-50 and y = 1. As source materials they used $H_3BO_3$, $K_2CO_3$, $MnCO_3$ and $V_2O_5$, processing the melt in the temperature of 1150$^{o}$C for 1h. It shows that manganese and vanadium can both be dissolved in the borate glass in appreciable amounts.

- Lithium borate glass with a wide range of lithium concentrations – calorimetric study

Matsuda et al. [89] focused on calorimetric studies of the glass transition dynamics in lithium borate glasses. Most of the testing has been conducted using the DSC (Differential Scanning Calorimetry) apparatus. A wide composition range of lithium oxide was studied, with precise data on concentration. A range of lithium borate glasses with following formula was created:

$xLi_2O\cdot(100\text{-}x)B_2O_3$, where *x* is the molar concentration of lithium, ranging from 0 to70. It was impossible to form glasses with *x* greater than 70, due to fast crystallisation. Sample preparation was conducted using $LiOH\cdot H_2O$ and $H_3BO_3$, in the following process:

i. Reaction in an aqueous solution in a Teflon beaker
ii. Drying in an oven for 1-3 days at 130$^o$C
iii. The obtained powder was fused in a Pt crucible (1050-1300$^o$C for $0<x\leq30$ and 950$^o$C for $30<x\leq70$) for 1.5 hour
iv. Plate quenching, resulting in glass formation

This shows that lithium oxide dissolved in borate in a wide range of concentrations, however the process complicates with the increasing lithium content due to faster crystallisation and lengthy drying step.

Other metal borate glasses are also mentioned in the literature, like nickel [90], copper and magnesium [66], sodium [86], potassium [88], titanium and cobalt [83]. Unfortunately, they are most often tested as a glassmaking material only. It means that mostly magnetic, crystallographic and optical properties were evaluated. These are not directly relevant to the metallurgical industry, and give little feedback and background for the metal recovery processes. However, it proves that a wide range of metals can be dissolved in borate glass in varying amounts.

**Glass wetting phenomenon**

Glasses being oxide materials can present significant surface wetting at high temperatures, especially on other oxide surfaces. It is based on the similarity of the binding forces of the glass to the solid oxide, and therefore a high degree of electronic continuity is present at the solid/liquid interface. Because of that we need to be aware of the possibility of extensive wetting by borate glass during experiments, when using oxide crucibles like alumina or zirconia [91].

### 2.3.2.5. Boriding

Borates are commonly used for a process called boronation, or boriding. Boriding is a process producing a layer of borides of many metals in their surface. Such surface treatment increases hardness and wear resistance, as well as protects against oxidation and corrosion. It is a widely investigated process, due to its influence on the boronized metal. During boriding, metals undergoing the process gain ceramic-like hardness and resistance, but also the stiffness and brittleness as well [53,63,92–95]. Boriding can be performed in more than one way, using solid, liquid and/or gaseous media, as shown below:

- Electrodeposition

Mechanism of the electrochemical boriding process is as follows [64]:

$2Na_2B_4O_7 = 2Na_2B_2O_3 + 2B_2O_3$ (dissociation) (a)

$Na_2B_2O_3 = 2Na^+ + B_2B_4^{2-}$ (ionisation) (b)

$B_2O_4^{2-} = B_2O_3 + ½O_2 + 2e^-$ ( anode reaction) (c)

$2Na^+ + 2e^- = 2Na^0$ (cathode reaction) (d)

$6Na + 2B_2O_3 = 3Na_2O_2 + 4B$ (on the cathode) (e)

However, according to Kaptay and Kuznetsov [93], in molten salts the electrochemical boronation mechanism is a single 3-electron reduction process:

$B^{3+} + 3e^- = B$ (one-step reduction) (f)

With a very wide range of current densities in which it appears (5-112 A $dm^{-3}$ on iron [53]), the actual process can start very early. Electro-boronation can be also performed at relatively low temperatures like 500 $^OC$, for example by using $B_2O_3$ and Mg boriding substrate, in order to obtain titanium borides [65]. Depending on the conditions, environment and expected result, the boriding process is evaluated in wide range of currents and voltages. The process itself can occur very rapidly, due to the chemical nature of the process which happens before the proper electrodeposition occurs [93]. This makes it difficult or even impossible to avoid this phenomenon when the boron reduction conditions are met. Example of industrial boriding conditions are shown in Table 2.3-2 below.

*Table 2.3-2 Exemplary boriding conditions. Boriding is a process of boron deposition on or into metal substrate* [93]

| **Electrolyte** | ***U [V]*** | ***i [A]*** | **Cathodic product** |
|---|---|---|---|
| $LiBO_2$-$NaBO_2$-$TiO_2$ $(Li, Na)_2TiO_3$ | 0.31 | 0.008 | $TiB_2$ |
| KCl-KF $K_2TiF_6$-$KBF_4$ | 0.6 | 0.2 | $TiB_2$ |

- Boronation from gaseous phase

As a pure chemical boronation, such process can be made using gaseous phase. Iron can be boronated from the gaseous phase using $BBr_3$-hydrogen mixture vapours, in 450-750$^oC$, under normal atmospheric pressure. As a result polycrystalline monoboride FeB is formed on and under the surface of the iron sample [92].

- Chemical boriding

Boronation can be also conducted by chemical means of reduction in a solution, like for chromium [96] or titanium [97], following simple chemical reaction:

$$Ti + 2BBr_3 + 6Na \rightarrow TiB_2 + 6NaBr$$

In this case, sodium plays the role of reducing agent. The whole process is conducted under 400 $^oC$, making it a low-temperature process in comparison to other metallurgy processes. The source material in this case is the boron tribromide with titanium powder. While the whole process takes 6 hours to complete, results can be seen long in early moments of the reaction, though with lower yield and high crystallinity [97].

Due to the various relatively easy ways boron atoms can be deposited on a metal sample, it is suboptimal to use boron salt as a medium or environment for electrochemical metal recovery. Electroplating of metals from borate salts results in the plated metal being inevitably contaminated with boron atoms [51]. In order to obtain pure metals from ions dissolved in a borate phase, another step with intermediate medium would have to be introduced into the process.

#### 2.3.2.6. Borate anomaly

Some of the borate glass properties are counter-intuitive, in significant part due to the phenomenon called *borate anomaly*. Physical properties of these mixtures do not follow the concentration changes, but rather form maxima and minima against their composition. Thus, it is difficult to predict the properties of complex systems with borate slag. The reason for this anomaly has been studied by other researchers and is present in the literature [59,77,84,98,99]. An example of such an anomaly is the material fragility index, which peaks at around 50% of alkali oxide concentration in borate glass and then the index value decreases [84]. Another example is given by Shelby where he analyses the influence of $R_2O$ (R – alkali metals) content on the thermal expansion coefficients of borate glass samples. It was concluded that the strongest effect can be observed around 20-30 % molar concentration of the alkali metal in the borate mix, above which the trend started to reverse.

The borate anomaly explanation considered most reasonable by the author is the one described by Doweidar [77] as well as Shelby [98]. In both of these works it is explained that $B_2O_3$ glass consists of flat $BO_3$ triangles. Addition of metal oxides results in transformation of $BO_3$ triangles into $BO_4$ tetrahedra. In other words, a change from 3- to 4-fold coordination of the boron atoms. If a more significant amount of an $R_2O$ is added, formation of NBO starts which results in a reverse of the initial effect. The formation of 4-coordinated borate tetrahedra is shown in Figure 2.3-1 in section 2.3.2.1.

While this theory is generally agreed upon and is a good indication for the reason of the properties change originating from the boron oxide network modifications, upon closer inspection it was discovered that a number of more complex, intermediate structural groups can be formed in alkali metal borates [98] causing competing effects. This explains the peak effects being slightly different for each specific property (e.g. thermal expansion, glass transition, metal solubility) as observed by other researchers. As molten borates are known to be highly polymeric [59], their network properties are retained in the liquid phase and so is the influence of alkali metal oxides.

### 2.3.3. Chlorides

Many useful chlorides are widely accessible, e.g. NaCl being an everyday consumable or AgCl being used as a vital reference electrode component across the world, and some of them have been thoroughly evaluated. Large amounts of sodium chloride are used across many industrial processes, which constitutes the dominant use of this chemical [100]. Chloride salts are widely used in the metals electrodeposition industry, e.g. for Ni and Mn [101], Ti[102], Al-Nb[103], Mg, Ce and Li [104], Ag [105], or even metals from the f-block [106]. The use of molten chlorides in electrochemistry requires atmosphere control, e.g. inert gases like argon and additional control measures due to the salt evaporation at high temperatures [107]. Chlorides are a common medium in electrochemical processes, as they are known to provide a stable medium for electrodeposition of a range of metals. They enable good process repeatability, efficiency and high quality of electroplated metals, and thus are of high interest for electrometallurgy [104,108,109]. Furthermore, with sodium chloride prices being relatively low, and its production and accessibility all over the world [110], its use can have a positive effect on the economic feasibility of the process considered.

**Chlorides high conductivity phenomenon:**

High temperature ionic liquids, due to their ionic form, are considered to be conductors of the second class – electric current is transferred by the cations and/or anions movement across the melt. However, there are melts of extraordinarily high conductivity, impossible to explain using the standard second class conductor models. It has been assumed that the electron component is being "superimposed" on the ion component, resulting in an *ion-electron* conductivity model. As an example, it has been reported that molten salt mixtures of the CuCl-$CuCl_2$-MeCl (Me = Li, Na, K, Cs) behave accordingly to the ion-electron conductivity model in a wide interval of concentration ration between copper and alkali-metal chlorides [111].

#### 2.3.3.1. Electrochemical potentials in molten chlorides

*Electrochemical potential* is a chemical specie thermodynamic property and can be defined as the work required to bring 1 mole of an ion from a standard state to a specific concentration. It is also the standard molar Gibbs free energy at the specified electric potential [112]. *Electrode potential*, which is relevant to this work, often called electrochemical potential to the confusion of the readers, is the electric potential on an electrode component, which appears as an interface between the electrode and the surrounding electrolyte. According to IUPAC

definition [113], it is defined as the electromotive force of a cell in which the left-hand electrode is a standard hydrogen electrode, and the right-hand electrode in the one under evaluation. *Electromotive force* of any cell is defined as the difference between its cathode and anode potentials, with the latter with negative sign. Alternatively, the *absolute* electrode potential is the potential versus a free electron in vacuum [114]. Electrode potential depends on the nature and composition of the phases, and for non-equilibrium state also on the kinetics of the reaction ongoing at the electrode's surface.

As a result, most of the experimental aqueous systems are referred to the standard hydrogen electrode (SHE) commonly assumed to be the 0 V point. This is not always the case with molten salt systems, as the SHE cannot be used above certain temperatures and the use of other standard reference electrodes can be impossible in a molten salt environment [115]. Review of alternative reference electrodes used to define the cell potentials in non-aqueous systems is included in section 2.3.3.2.

The electrochemical potential can be also calculated using basic thermodynamic calculations derived from the Gibbs free energy equation (2.3-4), and/or the Nernst equation (2.3-6), depending on the data available and the system in question. Most often validation by experimental methods is necessary, as these equations do not include some thermodynamic influences present and specific to each electrochemical cell.

$$\Delta G = -RTlnK = -nFE^0 \tag{2.3-4}$$

$$E^0 = \frac{-\Delta G}{nF} \tag{2.3-5}$$

$$E_{Nernst} = E^0 + \frac{RT}{nF} ln \frac{a_{Ox}}{a_{Red}} \tag{2.3-6}$$

where: $\Delta G$ – Gibbs free energy, $R$ – gas constant [$J\ K^{-1}\ mol^{-1}$ ], $T$ – temperature [$K$], $K$ – equilibrium constant, $n$ – number of moles of electrons, $E^0$ – standard cell potential [$V$], $F$ – Faraday constant [$C\ mol^{-1}$], $E_{Nernst}$ – cell potential [$V$] and $a_{Ox/Red}$ – activity coefficient.

In a non-ideal electrochemical cell, the electric potential that needs to be applied to overcome the desired reaction kinetic barriers needs to include a number of influences, like overpotentials. The required cell potential can be represented by the following equation (2.3-7) [116]:

$$E = E_c - E_a - |\eta_c| - |\eta_a| - i(R_{soln} + R_{circuit}) \tag{2.3-7}$$

where: $E$ – cell potential [$V$], $E_{c/a}$ – cathode/anode potential [$V$], $\eta_{c/a}$ – cathode/anode overpotential [$V$], $i$ – current [A], $R_{soln/circuit}$ – solution/circuit resistance [$\Omega$].

The difference between the thermodynamic potentials (calculated using Gibbs or Nernst equations) and the experimentally measured values can be different, due to a number of reasons. Firstly, a reference electrode is often used, resulting in a shift referred to as $E_{ref}$ when compared to the full-cell potential calculated with the Nernst equation. Secondly, each system has its specific overpotential composed of *activation overpotential* ($E_{act}$) often called reaction overpotential caused by the activation energy necessary to transfer the electron between the electrode and the electrolyte, *concentration overpotential* ($E_{conc}$) which accounts for the depletion of the reactant at the electrode surface and includes the diffusion overpotential, and *resistance overpotential* ($E_{\Omega}$), which includes junction overpotential, electrode capacitance and are specific to each cell design. These influences can be written as follows:

$$E_{exp} = E_{Nernst} + E_{ref} + (E_{act} + E_{conc} + E_{\Omega}) \tag{2.3-8}$$

$E_{act}$ is related to the electrochemical reaction happening at the electrode, so it is specific to each metal compound (same as the thermodynamic values $E^0$ and $E_{Nernst}$). The same would apply for the $E_{conc}$ values, which depends on each specific case. The difference between the thermodynamic value and experimentally measured potential caused by the use of the reference electrode is recognised as the $E_{ref}$ in equation (2.3-8). $E_{ref}$ value can be assumed consistent in the given cell set-up, as the electrode material is in most cases selected to be chemically stable in the given process environment and it is not taking part in the reaction, so its stability is not compromised by the passing electric current [115,117–120]. As for the $E_{\Omega}$, high temperature ionic liquids are considered to be conductors of the second class (current transferred by the ion movements across the melt). However, some molten salt mixtures, including CuCl-$CuCl_2$-NaCl were reported to show ion-electron conductivity due to the superimposition of the electron component on the ion [111]. For this reason, it cannot be ruled out that the metal chloride present in the melt has an influence on the cell resistance overpotential as well. To summarise, the shift in the electrochemical reduction potentials between the thermodynamic and experimental values can be caused by the activation, concentration and resistance overpotentials and the use of the reference electrode, with the last element consistent between the samples. Therefore, each new system has to be evaluated in order to obtain the non-ideal electrochemical red-ox reaction potentials. This way, a comparison against the calculated thermodynamic values is possible.

In regard to molten-salt systems, Gaur et al. [108] measured the reduction potentials for a range of metals at 475 $^{O}$C, using Ag(0)/Ag(I) as the reference point. In his analysis the electrode potentials for a number of transition metal based systems are evaluated. The salt used for the experimentation was a molten magnesium chloride-potassium chloride mix (32.5-67.5 mol%). As the Ag(0)/Ag(I) couple has been reported to obey the Nernst equation in molten chloride systems, it was possible to report the apparent standard electrode potentials for the evaluated metal-metal ion couples using the apparent standard potential of the silver system as a 0 V reference point. The values reported are listed in Table 2.3-3.

*Table 2.3-3. Apparent standard electrode potentials vs Ag(0)/Ag(I) as reference, at 475 $^{O}$C in molten $MgCl_2$-KCl* [108]

| ***System*** | ***Apparent standard electrode potential [V]*** | ***System*** | ***Apparent standard electrode potential [V]*** |
|---|---|---|---|
| *Mg(II)/Mg(0)* | -1.9213 | *Pb(II)/Pb(0)* | -0.4780 |
| *Mn(II)/Mn(0)* | -1.2078 | *Co(II)/Co(0)* | -0.3601 |
| *Zn(II)/Zn(0)* | -0.9262 | *Ni(II)/Ni(0)* | -0.1673 |
| *Ti(I)/Ti(0)* | -0.7554 | *Cu(I)/Cu(0)* | -0.1495 |
| *Cd(II)/Cd(0)* | -0.7168 | *Sb(III)/Sb(0)* | -0.0594 |
| *Cr(II)/Cr(0)* | -0.6546 | *Pd(II)/Pd(0)* | 0.3867 |
| *Fe(I)/Fe(0)* | -0.5364 | *Pt(II)/Pt(0)* | 0.5802 |
| *Sn(II)/Sn(0)* | -0.4836 | *Au(I)/Au(0)* | 0.8519 |

### 2.3.3.2. Reference electrodes in molten salts

Aqueous systems are usually referenced in relation to the Standard Hydrogen Electrode assumed to be at 0V, as explained in previous section. In non-aqueous systems however such an electrode cannot be used due to the lack of water and hydrogen, and considerably higher operating temperatures. This limits the range of feasible materials, and alternative reference systems, often called *quasi-references*, are used [115]. These will be discussed below.

The most commonly used reference electrodes found in molten salts systems are the electrodes of the first kind. These are based on a metal/ion relation, with the assumed metal activity of 1. According to the Nernst equation discussed previously, if the metal ion concentration remains

constant, and the solid metal activity of 1 can be removed from the equation, the electrochemical potential of such cell remains constant. Therefore, for such systems a non-reactive metals that take no part in the process reaction can should be used [115]. Examples of such systems are: molybdenum wire [121] or tungsten [118,120], both used by other researchers in molten halide systems.

Electrodes of the second kind can also be used in molten salt systems. These are based on a metal covered with that metal salt containing an anion common with the solution it is immersed in, e.g. silver-silver chloride systems. Due to the solubility issues especially at higher temperature and lack of anion concentration stability, such electrodes are not commonly used in molten salts electrochemistry [115]. As the electrode coating can dissolve in the system under evaluation, resulting in the electrode taking part in the reactions, electrochemical potential would vary invalidating the measurements.

There are some shortcomings inherent to the aforementioned systems, otherwise absent from the standard aqueous environments. High solution resistances can influence the measurements as reported by other researchers [122], although this is not relevant to the halide system used in this work, as previously discussed, due to their high conductivities. Nevertheless, care should be taken to avoid unnecessarily large distances between the reference and working electrodes. Secondly, the potential of each quasi-reference systems differs depending on the metal used and the environment/solution it is used in. Thirdly, such electrodes can show significant drift if the metal selected is not stable in the systems evaluated, which might prove challenging depending on the configuration under evaluation. Lastly, junction potential can be formed if used in mixed systems or in a sheathing [115].

Based on these considerations, the most feasible solution for the system evaluated in this work is a tungsten metal, due to its chemical, thermal and electrochemical stability [115,117–120]. Due to the borates ability to dissolve most of the metal oxides, no sheathing can be used as it would incur additional instabilities to the measurements.

#### 2.3.3.3. Electrodeposition profiles in molten salts

Electrodeposition process can be influenced by a number of parameters, including overpotential, temperature and diffusivity among others [114,123]. Each of these parameters can be changed resulting in different deposits being obtained. Firstly, potential applied to the electrolytic cell can result in the process being kinetically or diffusion limited, as shown in

Figure 2.3-14. This naturally leads to the diffusivity parameter, which controls the geometry of the deposits obtained. In a diffusion-limited region, the process is limited by the mass transport of the reagent, resulting in a typically highly dendritic deposits. This also allows for measurement of diffusion coefficients using electroanalytical methods, discussion of which will follow in this work. Alternatively, diffusion can be aided by convection by introducing mixing, which could limit the diffusion limitations resulting in a more uniform metal electrodeposition.

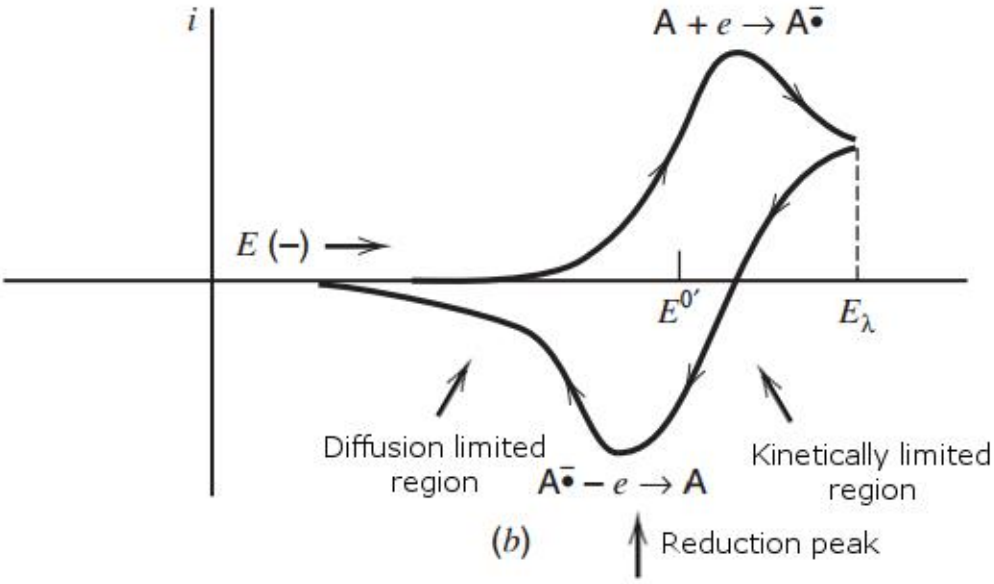


*Figure 2.3-14 Exemplary Cyclic Voltammetry curve of metal electrodeposition. Each peak corresponds to a redox reaction, anodic in the positive current region and cathodic in the negative. Preceding the peak current is the kinetically limited region, followed by the peak redox reaction potential and the diffusion limited region. The diffusion part is tailing, as the reaction is ongoing although at a lower rate due to the consumption of the analyte during the peak current. In the kinetic region no reaction happens as the reagents are kinetically locked in their current state and not enough potential is applied to overcome the energy barrier* [114].

Diffusion-limited electroplating behaviour has also been reported by other researchers in the molten salts research [70,124–126]. Example of such deposits is shown in Figure 2.3-15. One has to appreciate that the geometrical analysis of molten salt dendritic deposits is challenging due to the difficulty in retrieving the deposits, separating from the substrate without destroying the structure and sometimes water-sensitivity of the product, significantly limiting the applicable analytical methods.

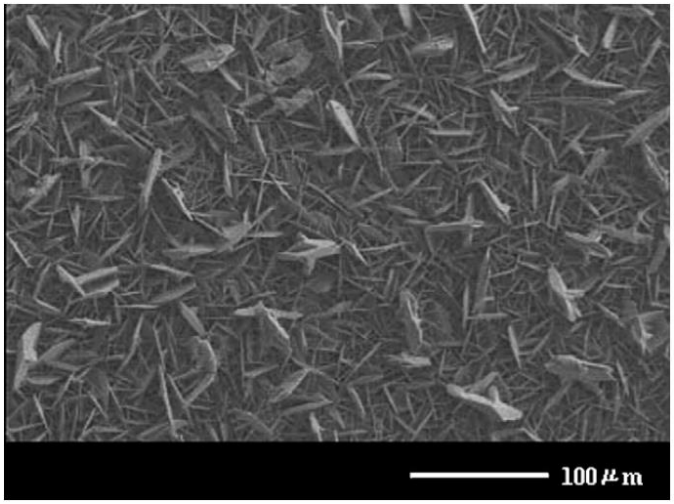


*Figure 2.3-15 SEM image of the needle-like deposits from the $BiCl_3$-$TeCl_4$ deposits. Deposition took place at 0.9 V vs $Al/Al^{3+}$ reference from the non-aqueous $AlCl_3$-NaCl-KCl mix at 423 K* [127].

Finally, temperature influences the viscosity and density of the considered mixture, which in turn influences the previously mentioned parameters like diffusion and overpotentials. Higher temperature generally lowers the kinetic barriers of the process, resulting in easier electrodeposition (lower electrodeposition potential), potentially more uniform deposits and/or more rapid processes by lowering the required electroreduction overpotential and increasing the reagents solubility in the mix. Alternatively, by increasing the temperature above the melting point of the deposits, liquid metal can be plated, resulting in almost-perfectly smooth drop-like deposits.

Cyclic Voltammetry profiles are also a good indication of the process *reversibility* [114]. Reversibility can be understood differently depending on the system evaluated and methodology, and can be defined as *chemical*; whether reversing the current flow in a cell reverses the chemical reaction on the electrode, *thermodynamic*; whether a reversible path exists between two states of the system, and *practical*; whether the system can attain equilibrium in a reasonable time in relation to the measurement time. The last definition is dependent on the observer's ability to observe disequilibrium and on the parameters of the experiment, e.g. reversible reactions might appear irreversible depending on the scan rate of a CV measurement. Usually, if a given reaction follows the Nernst equation, it is assumed to be thermodynamically reversible, or *Nernstian*. Reversible electrochemical reactions appear as a pair of redox peaks on a CV curve, and their reversibility can be estimated by the distance between these peaks – the potential difference required to reverse the redox reaction.

A commonly used sweep rate of 100 mV $s^{-1}$ has been reported by other researchers working with molten salts [125,128]. At higher sweep rates the nucleation step starts to have higher influence on the process as observed by Hills et al. [129], while at lower scan rates the current passing through the electrode become significant which may result in changed morphology of the electrode, e.g. formation of significant dendrites. Additionally, activity of the species on the electrode is different at different potentials and different concentrations, which influences the peaks shape, possibly obscuring the reaction onset. At higher scan rates the activity at the surface of the electrode would be much higher at the beginning of the process, resulting in higher peaks, while slower scan rate would form less pronounced, stretched peaks, as the specie have time to diffuse (resulting in higher current in the diffusion controlled zone), although their activity at the visible onset of the reaction would be lower [114]. Therefore, the usually applied rate of 100 mV $s^{-1}$ is a balanced choice.

#### 2.3.3.4. Electrodeposition of specific metals from molten chlorides

**Mg, Li and Ce electrodeposition**

A successful deposition of Mg, Li and Ce from molten chlorides has been described by Meng et al. [104]. In order to conduct the electrodeposition, a mixture of LiCl-KCl (50:50 wt.%) was melted in a quartz cell in an electrical tubular furnace, and kept to dry for 48h in 573K and 873K respectively. Magnesium and cerium were introduced into the mixture in a form of dehydrated chlorides. The electrolysis was performed using a molybdenum working electrode, and a graphite rod as a counter-electrode, at the temperature of 873K. The Cyclic Voltammetry scans produced are shown in Figure 2.3-16 and 2.3.-17.

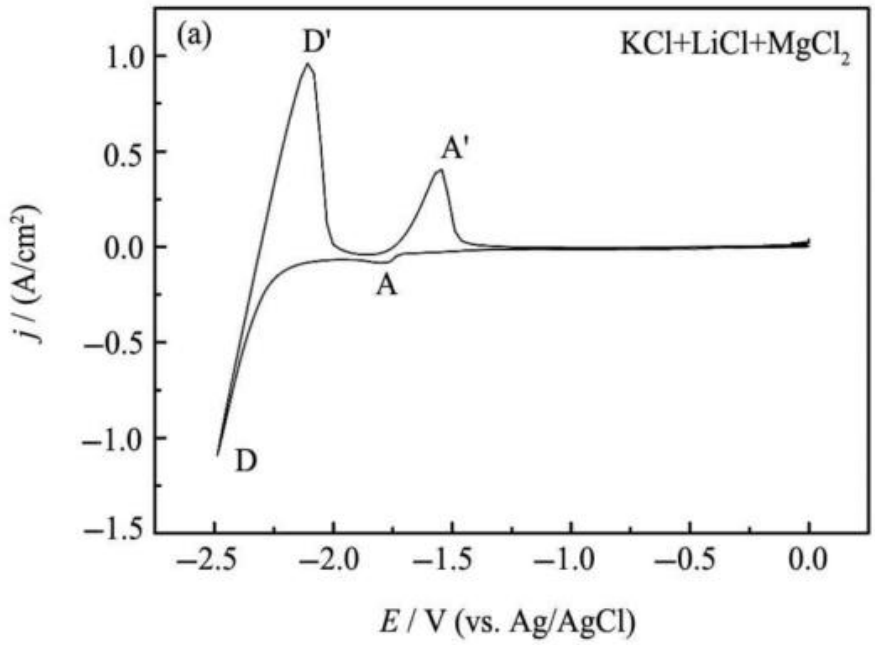


*Figure 2.3-16 CV scan of 1 wt% $MgCl_2$ reduction in the LiCl-KCl molten salt at 600 $^{O}C$. Molybdenum was used as the working electrode (0.322 $cm^2$), silver-silver chloride was the reference. Peak A corresponds to magnesium and peak D to the lithium redox reaction* [104].

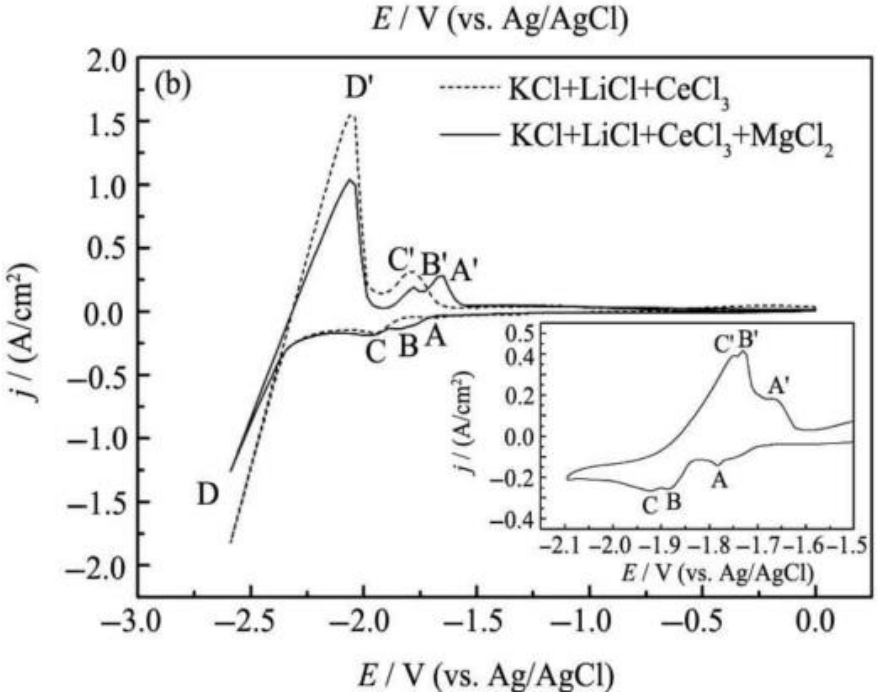


*Figure 2.3-17 CV scans of 1 wt% $MgCl_2$, 2.2 wt% $CeCl_3$ (solid curve) or 2.2 wt% $CeCl_3$ (dotted curve). Insert contains additional 1.1% of $CeCl_3$. The electrolyte was LiCl-KCl molten salt at 600 $^{O}C$. Molybdenum was used as the working electrode (0.322 $cm^2$), silver-silver chloride was the reference. Peaks are labelled as follows: A for Mg, B for Mg-Ce alloy, C for Ce and D for Li* [104].

It was proven that all of those three metals can be co-deposited directly from LiCl-KCL. However, as shown in Figure 2.3.-17, alloying might occur when metals present in the melt can form alloys and their reduction potentials are close to each other. Such phenomena need to be considered when trying to separate metals by electrolysis. Moreover, the composition can be controlled by the current density, changing the relative metal concentrations in the obtained alloy, turning an obstacle into a beneficial process.

Additionally, it is clearly visible that the oxidation/stripping peaks are significantly higher than the reduction curves. Such an effect comes from the charge transfer coefficient differences, as the process of reduction is limited by the analyte diffusing towards the electrode, while the reduced metal is readily available for the oxidation [114]. If integrated, the curves can show the charge passed, useful for comparison of cathodic/anodic current passed, providing additional insight into the process mechanics. Electrodeposited material was characterised and the deposits composition was analysed. Results are shown in the Table 2.3-4:

*Table 2.3-4 Mg-Li-Ce electroplating results* [104]

| ***Current density [A $cm^{-2}$ ]*** | ***Mg content [wt%]*** | ***Li content [wt%]*** | ***Ce content [wt%]*** |
|---|---|---|---|
| -4.66 | 92.82 | 3.51 | 3.67 |
| -6.21 | 75.51 | 18.46 | 6.03 |

**Uranium dioxide reduction in LiCl-KCl eutectic**

Brown et al. [130] analysed electroreduction of $UO_2$ species in molten halides, highly relevant for the nuclear fuel industry. Spent nuclear fuel in form of $UO_2$ needs to be reprocessed into pure uranium before it can be used again in a nuclear reactor. As a result, a reduction process in molten halides has been analysed using LiCl-KCl eutectic at 450 $^{O}$C. A CV sweep has been selected as a fitting method for the process analysis, as shown in Figure 2.3-18.

As seen in the graph, the reduction process is reported to be a single-step, 4-electron reaction, as indicated by the single C1 peak, with the A1 being the anodic oxidation response. Peak C2 corresponds to the electrolyte decomposition, while A2 represents the molybdenum electrode oxidation. P arrow marks the inflection current. In this work current density was not calculated due to the difficulty in assessing the immersion-defined area of the working electrode.

Additionally, it can be seen that the electrolysis in molten salts can inherently result in some relatively noisy readings, resulting in a difficult to analyse CV curves.

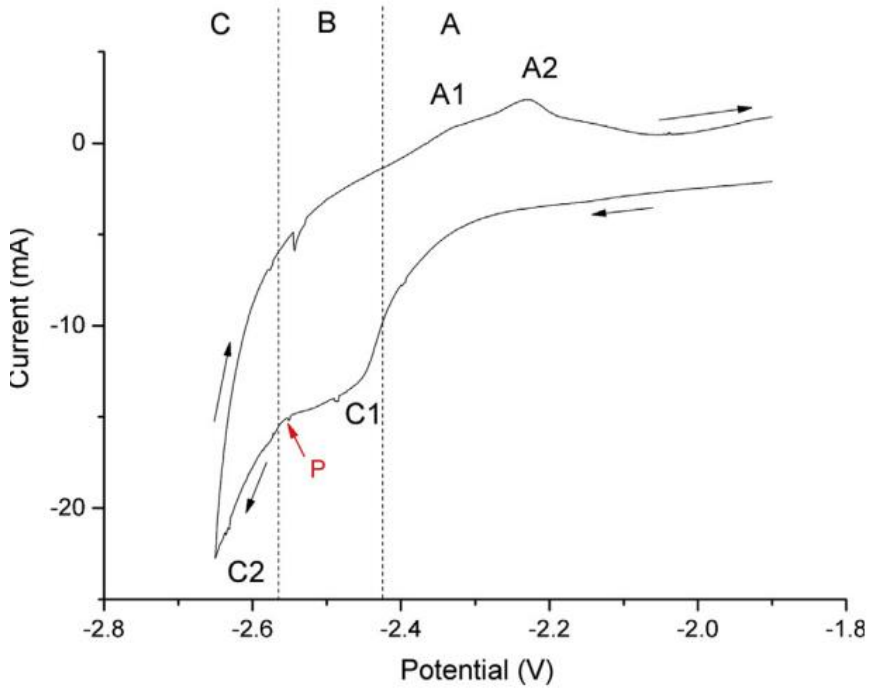


*Figure 2.3-18 Cyclic voltammogram of $UO_2$ reduction vs $Ag/Ag^+$ on a molybdenum electrode in molten LiCl-KCl at 450 $^{O}C$. Sweep rate of 10 mV $s^{-1}$ was used. The CV curve is divided into three regions: A before the electroreduction, B as the potential redox process region and C corresponding to the post-reduction area, where the electrolyte decomposition starts. P is the inflection point* [130].

**$PbCl_2$ electrolysis from molten LiCl-KCl**

Haarberg et al. [125] analysed the mechanics of metal chlorides electrolysis in molten halides eutectic mix of LiC-KCl. In his paper the metals were plated on a glassy carbon surface (crucible). Metal undergoing electroreduction worked as a reference located in a silica tube, with tungsten wire used for electrical connection. Molybdenum and tungsten were used as counter electrodes. The cyclic voltammogram produced is shown in Figure 2.3-19.

It can be seen that the $Pb^{+2}$ ion is reduced in a single 2-electron step as shown by a single peak, followed by a diffusion-limited tail. Moreover, similarly to the previous cases, anodic sweep results in a much higher stripping peak, as the availability of the reactant is significantly higher and not diffusion-limited, as the previously plated metal is not spread throughout the electrolyte. In this paper it is concluded that the process is diffusion limited, although can be

influenced by the nucleation phenomena, resulting in false diffusion coefficient readings if calculated from the transient electrochemical measurements. Important observation is also made that the foreign substrate used (carbon) resulted in a significant overpotential required in order to start the electroreduction process.

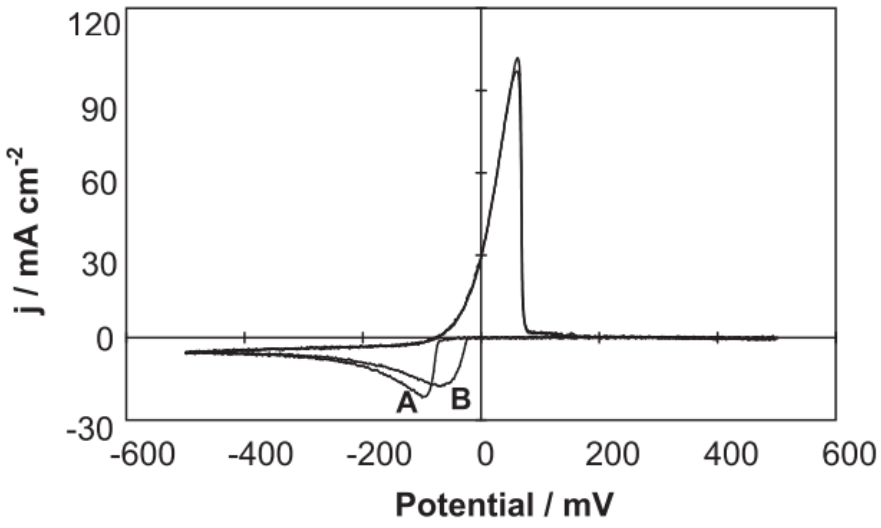


*Figure 2.3-19 CV plot of a $PbCl_2$ solution (0.031M) in an LiC-KCl eutectic at 400 $^{O}$C. Sweep rate of 100 mV $s^{-1}$ was used versus Pb metal. Glassy carbon crucible worked as the cathode. Curves A and B were produced after a scan with 1 V and 0.5 V anodic switching potential, respectively*[125].

**Other metals electrodeposition**

Electrodeposition from molten salts is very different from aqueous systems, due to lack of the solvation layer, full ionisation, relatively faster kinetics caused by significantly higher temperatures, among other reasons [72,131]. As a result, a number of metals and more complex components are obtained this way, e.g. Nb [132], Sm [133,134], Th [135], Ti-W alloys [48], Mg [124], or Nd [136]. However, none of the electroreduction systems available in the literature at the moment of writing this thesis adopted two- or multi-salts system, which is the key innovation in the system described in this work.

### 2.3.4. Borate-Chloride mixed system

As explained in previous sections, depositing a pure metal from borate using electrochemical methods is challenging, due to boron contamination present in the sample after processing and a relatively small electrochemical window [59]. Chlorides, which are commonly used for industrial electroplating processes [110], require strict atmospheric control during the process [101,104,108,137] and are not as resistant to impurities and water pollution as oxides (i.e. borates). As a solution, a mixed chloride-borate salts system has been used for metals leeching and/or extraction [51]. Such an environment would bear both salts positive properties if configured and used properly. A borate-chloride system has not been thoroughly examined, however it has been mentioned in the literature, as follows:

Molten alkali borates show immiscibility over a wide range of compositions when coupled with molten chlorides, as well as specific metal ions selectivity. Molten borates are considered to be highly polymeric when molten, unlike molten chlorides which are highly ionic. The reason behind the immiscibility of these two salts has been explained as caused by the difference in the molten phases ionic and non-ionic nature [59]. While molten electrolytes are usually considered to be fully ionic, the covalently bonded nature of borates causes the immiscibility. The immiscibility can be overcome by adding alkali oxides to the melt; however, the immiscibility region is quite extensive. While the phases are immiscible, ions of metals dissolved in the system are distributed between the two phases in proportions dependant on the nature of the ion itself and the salts composition.

Williams et al. [23] is first reported to evaluate this system to some extent. The observed system was created using NaCl, $Na_2O$, NaF, $B_2O_3$, and additional metals. Preliminary tests on the borate-chloride composition have shown that in such case free-flowing, immiscible, and easily separated liquids are formed. Most importantly, there is an ongoing ionic-exchange process between the two liquids, according to reaction (2.3-9):

$$MO_{(s)} + 2NaCl(l) + B_2O_3(l) = MCl_2(l) + 2NaBO_2(l) \qquad (2.3\text{-}9)$$

Knowledge of the reaction allow for thermodynamic estimations of the distribution coefficients for specific metals, if sufficient data on the species activity coefficients and concentrations in each phase was available.

The amount of metal ions dissolved in halide layer is usually very low, as the following reaction (2.3-10) Gibbs free energy ($\Delta G$) is large and positive:

$$MO + 2NaCl = Na_2O + MCl_2 \quad (2.3\text{-}10)$$

However, the following reaction (2.3-8) is capable of the oxygen removal from the halide phase and significantly lowers the activity of $Na_2O$ in the system [138], which would allow for increased metal oxide solubility. For such a reaction to happen, it requires $B_2O_3$ dissolved in the halide phase.

$$B_2O_3 + O^{2-} = 2BO_2^- \quad (2.3\text{-}11)$$

The amount of boron oxide present in the halide phase is related to the alkali metal oxide present in the mix, as shown in the phase diagram in Figure 2.3-20.

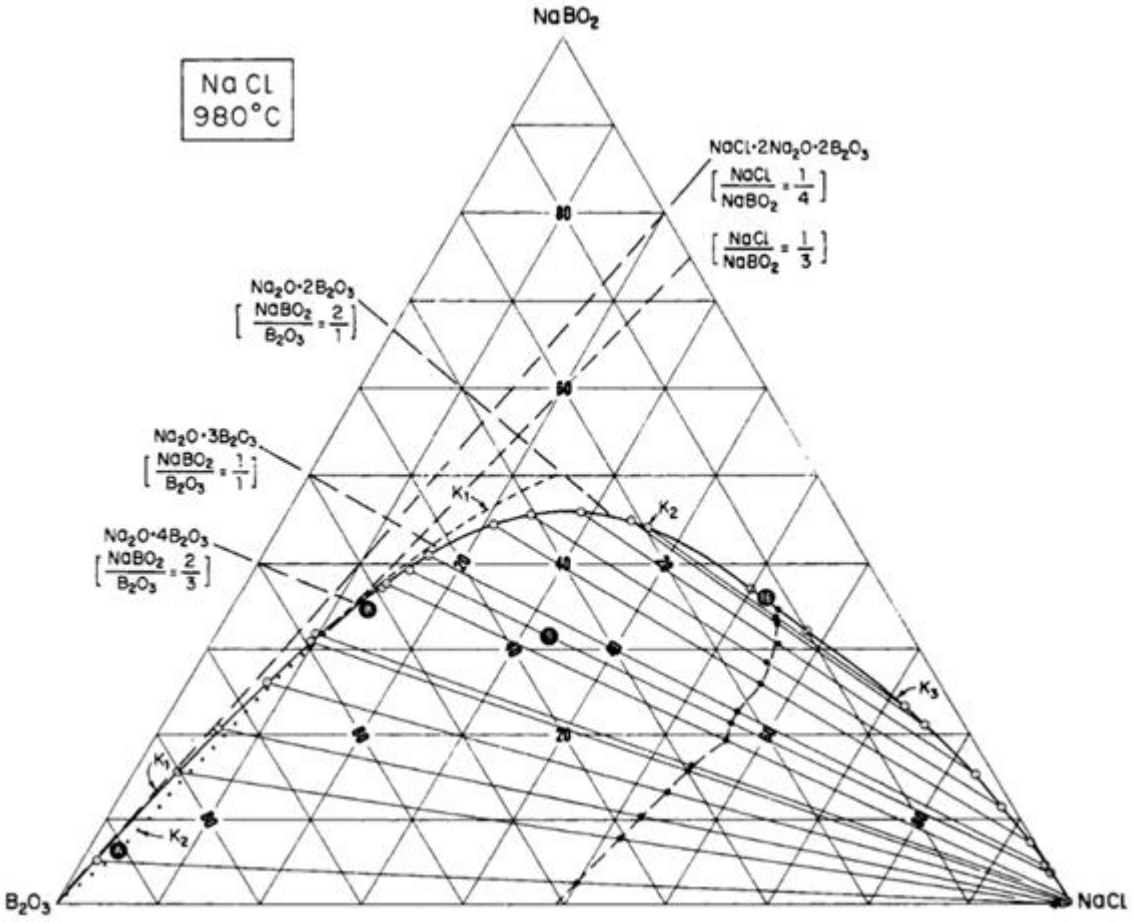


*Figure 2.3-20 Immiscibility diagram for the $Na_2O$-$B_2O_3$-NaCl system. The composition evaluated in this work is in the region resulting in immiscibility of the halide/oxide phases.. Redrawn from* [139] *with permission.*

It can be seen in the figure that the amount of $B_2O_3$ present in the halide phase is negligibly low for the compositions in the immiscibility region, as represented by the tie-lines orientation. This limits the $B_2O_3$ influence on the metal oxide solubility suggested by the reaction (2.3-10), for the immiscible phases configuration. Contributing to the partition coefficient is a second theory, considering negative exchange sites in the borate phase [59], as explained in the previous section. As the alkali metal oxide content rises (with the maximum effect at around 25 mol%), due to structural changes in the highly polymeric borate network, as represented by Figure 2.3-1, negative exchange sites are created capable of positive charge screening. This causes the metal ions affinity to shift towards the borate layer, reducing the amount of metal ions present in the halide layer for a range of $Na_2O$-$B_2O_3$-NaCl compositions.

An altogether different behaviour can be expected from metals capable of oxychloride formation. Such metals would form different compounds in the halide layer, diverging from the assumed reaction (2.3-9). As a result, specific partition coefficients can be expected for these cases, heavily reliant on the partial oxygen pressure in equilibrium with the melt. Metals reportedly forming oxychlorides in oxide-halide systems are chromium (Cr) and iron (Fe) [59].

In conclusion, metal ions distribution between the molten oxide (i.e. borate) and halide (i.e. chloride) phase vary in a significant range for different metals and environments. Some preference towards the borate phase has been reported in the literature as mentioned here and in previous sections. The distribution coefficients are closely connected with the valence of metals, showing a change in the magnitude of value between two- and trivalent metals, oxygen partial pressure, and alkali metal oxides presence [23,59,139]. It is also suggested that the considered molten salt system composed of sodium chloride and sodium borate phases could be used as metal extraction system for a range of metals.

### 2.3.5. Predominance diagrams

There are two main forms of predominance diagrams used in electrochemical sciences – Pourbaix diagrams [140] used to describe aqueous environments, and Littlewood diagrams [141] for the non-aqueous systems. Such diagrams depict regions of stability for various phases at certain conditions, usually represented versus oxygen levels or pH for Pourbaix (x-axis), and electrochemical potentials or another specie concentration/activity (y-axis). They can be used to thermodynamically define the system being evaluated, and subsequently predict the reaction routes based on the intermediate phases stability. This can be useful for corrosion or electrochemical redox reactions analysis. Additionally, levels of oxygen impurity in metals obtained can also be inferred. Predominance diagrams are constructed by stability prediction of certain phases based on their Gibbs free energy of formation of the compounds, which then subsequently can be used to estimate the electrochemical potentials via equation 2.3-5, as previously described in section 2.3.3. Resulting are diagrams like shown in Figure 2.3-21, drawn for the FFC Cambridge process, in this case describing reduction paths for titanium.

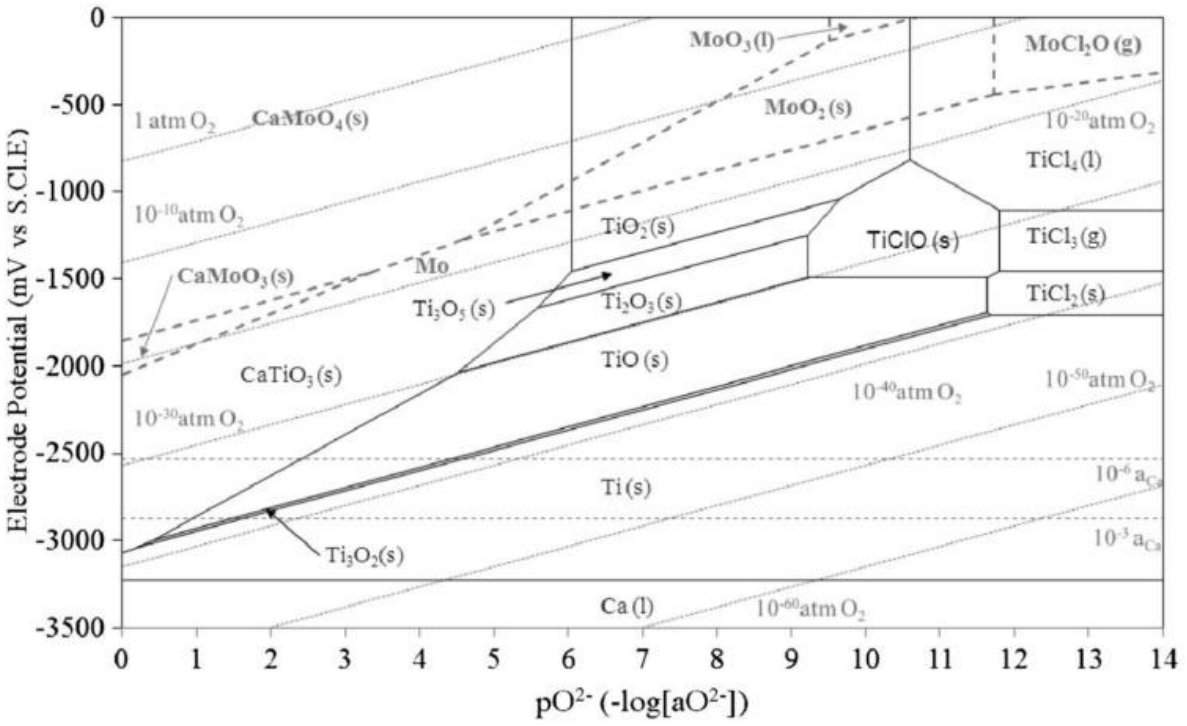


*Figure 2.3-21 Ca-Ti-O-Cl and Ca-Mo-O-Cl overlaid predominance/Littlewood diagrams. S.Cl.E. (y-axis) stands for standard chlorine electrode. This diagram describes the system used in the FFC Cambridge process, previously described in section 2.2. Adopted from* [49].

From the predominance diagram above it can be read that $MoO_2$ can be reduced directly to Mo in one reaction. It also shows that it is possible to reduce $CaTiO_3$ directly to Ti via reaction 2.3-12. Electrochemical potential of the reactions can also be read as described, showing that lowering the $pO^{2-}$ a more negative potential is required to obtain pure Ti. Alternatively, stability of oxychlorides at certain parameters is also theoretically confirmed. Analysis like this can help to optimise the process and better understand the reactions occurring.

$$CaTiO_3 + 4e^- \rightarrow Ti + Ca^{2+} + 3O^{2-} \quad (2.3\text{-}12)$$

The following Littlewood diagram for Ni-LiCl system [141] is relatively simpler, and more relevant to the work developed in this thesis. The diagram is shown in Figure 2.3-22. It is shown that $NiCl_2$, compound naturally stable at the temperature of 800 $^{O}$C, can be reduced to pure nickel metal in a one-step reaction with no intermediate phases in-between at the cathodic potential of -0.9 V from the given system. This can be a very useful information, as it suggests for example that in case of a Cyclic Voltammetry scan in such system only one reduction peak should be observed, for the reduction of $Ni^{2+}$ ion to Ni metal.

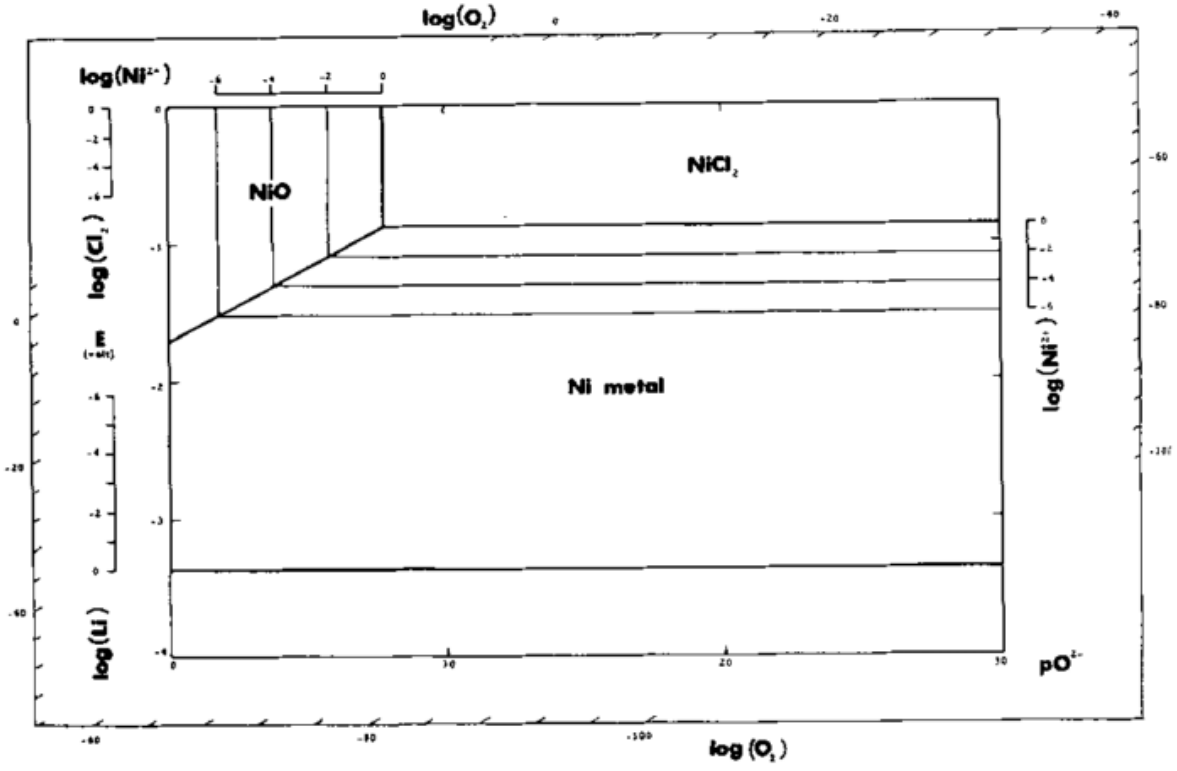


*Figure 2.3-22 Littlewood diagram for the Ni-LiCl system at 800 $^{O}$C. Stability of NiO, $NiCl_2$ and Ni metal at certain parameters can be inferred from this graph. Adopted from* [141].

As mentioned before, creation of predominance diagrams requires knowledge of certain thermodynamic values, i.e. Gibbs free energies, to estimate the stabilities of certain phases at certain parameters. The difficulty with the novel system evaluated in this work is a certain lack of thermodynamic data, similarly observed in case of phase diagrams, as described in section 2.3.2. Due to these gaps in knowledge, no other Littlewood diagrams relevant to the developed process were accessible at the time of writing this thesis. Presence of such would greatly benefit the understanding and optimisation of the processes occurring in the designed electrochemical cell.

### 2.3.6. Diffusion in molten salts

The diffusion coefficient is materials property, with a number of studies reported and various systems examined [142]. However, the data is quite often widely dispersed and the results vary depending on the experimental methods used. In electrochemistry, a range of methods is used for diffusion analysis: chronopotentiometry (CV), chronoamperometry, linear sweep voltammetry (LSV), polarography, rotating disc electrode and faradaic impedance [142]. For the needs of this project, chronoamperometry was selected as the most fitting method for the observation of the process kinetics. It allows for the process analysis and the potential side-reactions detection, as well as numerical correlation of the current variations with the progress of the electrodeposition.

In electrochemical processes, molten halides show high conductivities and charge transfer rates at elevated temperatures. Therefore, most commonly the diffusion is the limiting step for the whole process [51,125]. As such, this (diffusion) would be the parameter limiting the charge passing through the electrodes in a specific amount of time, and therefore possibly extracted from the data collected during the process of electrodeposition.

Chronoamperometry has been reportedly used for evaluation of the diffusion behaviour in molten electrolytes [124,125,143]. In order to assure the reduction of the reactant concentration on the electrode surface to a fraction of the bulk concentration, an overpotential needs to be applied of around -200 mV above the peak reduction value [125]. Correlation between the current and diffusion can be described by the Cottrell equation (2.3-13):

$$I = \frac{nFAc^{\infty}\sqrt{D}}{\sqrt{\pi t}} \tag{2.3-13}$$

Where: $c^{\infty}$ is the analyte bulk concentration [mol cm$^{-3}$], $n$ is the amount of electrons exchanged, F is the faraday constant, $A$ is the electrode area [cm$^2$], $D$ is the diffusion coefficient [cm$^2$ s$^{-1}$] and $t$ is time [s]. This equation can also be transformed to calculate the diffusion coefficients:

$$D = \frac{I^2\pi t}{(nFAc^{\infty})^2} \tag{2.3-14}$$

The standard Cottrell equation (2.3.-14) assumes flat electrode with equal current density distribution across the surface. Alternatively, other Cottrell equation forms can be created by differentiation equations and Laplace's transform, e.g. for a sphere electrode (e.g. for mercury

droplet electrode measurements) [114]. The reason is that diffusion to a flat surface is linear and equal for each surface element, while for more complex geometries it depends on the shape of the surface [123]. Additionally, the analyte accessibility is unequal in case of uneven surfaces resulting in preferential plating zones and current density variations.

In addition to that, Cottrell equation assumes that the system is semi-infinite, meaning that the process ongoing on the surface of the electrode does not have an influence on the bulk of the electrolytic cell. This is of course only true for a certain time, limiting the process time to which the equation can be applied. Moreover, electrode size needs to be minimal when compared to the volume of the solution. This further limits the time of the process as with the ongoing electroreduction the surface of the electrode becomes metal-coated, changing both its geometry and surface area.

However, electrochemical measurements can be quite often influenced by side effects/reactions, like nucleation and deposition of a metallic phase [125]. In Cyclic Voltammetry (CV) there are significant deviations possible caused by the deposits failing to form nucleation sites at sweep rates, too high to allow for the process to occur properly, causing shifts towards more cathodic values. In chronoamperometry, fractions of the current spent on parallel reactions cannot be separated from the collected data, and requires highly clean environment to rule out co-deposition of other elements. Similar challenges are present in case of chronopotentiometry, as well as other electrochemical methods [125]. Thus, diffusion coefficients calculated from the values measured, especially at high temperatures and in complex systems, can show significant deviation from the expected values, with the process still being directly dependant on the diffusion step.

Diffusion controlled electrodeposition processes are reported to show dendritic growth of the deposited material [114,126,144]. Macroscopic growth of the deposited material can result in an increase of the effective electrode surface area in contact with the electrolyte, causing an increase in the current flow. However, the effect cannot take place in an elevated temperature environment where the melt temperature is higher than the specific metal melting point. It can be also avoided by using smaller currents or smoother distribution of the metal ions across the solvent, e.g. by emulsification or mixing. The deposited dendritic structures could be evaluated using the X-ray transmission analysis [145], enabling correlation with the process parameters and offering deeper analysis of the process kinetics.

### 2.3.7. Solvation in ionic liquids

Solvation is a process of association of solvent molecules (here: molten salt) by a solute. Solvation shells and mechanisms are relatively thoroughly evaluated in water systems; however, they differ from the ionic liquid systems, and therefore need to be considered as a separate case. In water, solvation layers are usually formed by dipoles of water particles, forming a shell around the solvated ion. In molten salts though the solvent is usually completely ionic, thus dissimilar to the aqueous models, resulting in different influences and reactions [112,114].

Solvation mechanisms differ for various ionic liquids, and even some researchers suggest that there can be transient complexes present in ionic molten salts, although such an opinion is receding [146]. The solvation layers depends on the ionic liquid in use, and it has been reported than up to seven solvation sub-layers can be formed for some complex ionic-liquids, with the number determined by the composition of the electrolyte [147]. These layers are reported to be sensitive to even small amounts of other elements presence in the liquid. It is however commonly agreed that the solvation energies (referred to as $\Delta G_{solv}$) can influence the activities of the ionic species considered, and subsequently the electrochemical reactions involving these species and their potentials.

Born-Haber cycle [112], primarily used to calculate lattice energies (enthalpy change involved in formation of a compound from ionised/atomised species) by applying Hess law is one example on how to include the solvation layers' influence. It considers atomisation, ionisation and dissociation energies, and by creation of a closed cycle (therefore the name) one can assess the apparent difference in the energies balance, when comparing the standard enthalpy of formation of a given compound and the calculated path, as shown in Figure 2.3-23. However, according to the Hess law, the energy required to form a compound is same regardless of the path taken. Therefore, the apparent energy difference is caused by a certain phenomenon, like the solvation of the ions, with its energy equal to the difference calculated. However, for such calculations to be possible, extensive thermodynamic databases are required and, at the moment of writing this thesis, such were unavailable for the system considered.

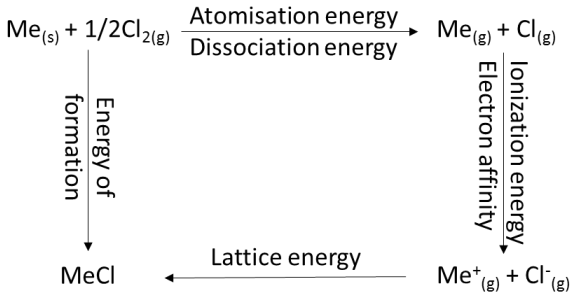


*Figure 2.3-23 Born-Haber cycle representation. Adopted from* [148].

The solvation layers formed by liquid electrolytes, when used in electrochemical cells can influence dissolved ions as well as the electrolyte/electrode interface, both strongly dependant on the chemical composition of the electrolyte. Therefore it is important not to regard ionic liquids as neutral solvents, as they can have a significant influence on the electrodeposition processes and ion transport mechanisms [149]. As an example, much higher solvation enthalpy of $Cu^{2+}$ when compared to $Cu^{1+}$, results in a one-step reduction reaction to copper metal in water system. However, in case of molten salts, different solvation mechanisms could lead to a more stable $Cu^{1+}$ ion, resulting in the ion shuttling between the electrodes.

Another interesting example has been observed by analysing the $LnCl_3$-(LiCl-KCl) system at 500 $^{O}$C in an electrochemical cell [150]. The elements evaluated (Al, Ce, Cy, Gd, Nd and Sm) were used at a concentration of 3-5 wt% of their respective metal chlorides. Solvation of lanthanides in LiCl-KCl has been evaluated, and it was reported to result in clusters of $[Ln(KCl)_n]^{3+}$ and $[Ln(LiCl)_n]^{3+}$, where n varied from 4-9. This subsequently caused shifts in the reduction potentials due to the specific stability of the clusters formed in the melt. It is predicted that presence of multiple lanthanide components would significantly affect the solvated clusters and result in lower stability, subsequently causing shift towards less negative reduction potentials.

In Figure 2.3-24, a CV scan of $CeCl_3$ + $LaCl_3$ system in a eutectic LiCl-KCl melt is shown. It is clearly visible that not only additional metals result in the reduction peaks shift, but also the anodic peak, corresponding to the chlorine evolution, has shifted when the composition changed. This is in line with the solvation influence discussion above and shows that both anodic and cathodic reactions can be influenced by this phenomenon and the changes in the melt composition [150]. These influences have to be kept in mind, when analysing similar systems.

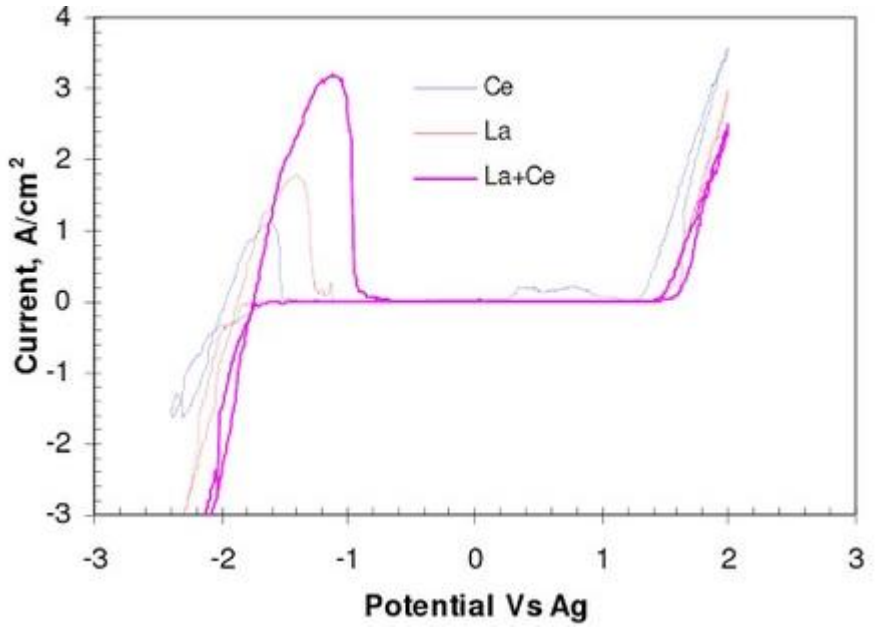


*Figure 2.3-24 Cyclic Voltammetry scan of the $CeCl_3$ + $LaCl_3$ system in a eutectic melt of LiCl-KCl at 500 $^{O}C$. Scan rate of 20 mV $s^{-1}$ vs Ag/AgCl reference was used. Tungsten was used as the inert cathode. Both cathodic and anodic reactions peaks shifts can be observed with the changing feed composition* [150].

# 3. Problem approach

## 3.1. Objectives

The aim of this project was to create a completely new system capable of efficient and clean electrochemical reduction of metals residing in Li-ion and Ni-MH batteries, based on molten salts system. As stated in the literature review, there are valuable metals like lithium, nickel, cobalt, manganese, copper and other, which can be found in scrap batteries/electronics, commonly called the eWaste. The concept was used to evaluate a process base capable of stable, continuous recovery of valuable and rare metals from a variety of sources, with the possibility of applying it to wider metal waste recycling streams. Therefore, the system considered should be chemically resistant to a variety of potential pollutants, e.g. traces of water, solutions, number of organic compounds from the electrolyte and other metals and compounds.

The considered system needs to meet the following requirements:

- Good resistance to various chemicals, both non- and organic based
- Good metals/metal oxides solubility
- Good diffusion coefficient, for efficient migration of ions
- Chemical stability
- Electrochemical stability
- Wide electrochemical window
- Thermal stability
- Low vapour pressure

Also preferably:

- Low melting temperature
- Low viscosity
- Easy to retrieve metal deposits

In order to meet the requirements, a multi-salt system is needed. Good electrolytes (i.e. halides) are usually not stable in open air environment and thus require strict atmosphere control, while good metal solubility and thermal stability is a feature of oxides. Since in recovery from waste streams pollution resistance is crucial, the process should be capable of withstanding an amount of surplus, undesirable compounds. Finally, to create a multi-phase

system with separate molten salts, the composition must be chosen as to assure the immiscibility of the phases, allowing to retain required properties of the system while not hindering the process efficiency by introducing mechanical interface barriers.

## 3.2. Process design

The proposed process would consist of three main steps. Firstly, metal containing waste would dissolve in the borate melt, and diffuse towards the liquid-liquid interface created by the oxide-halide phases. The temperature of the melt (900 $^{O}$C / 1173 K) is a balance between the melting temperature of the melt components and their stability, as well as thermal resistance of the vessels and available metal electrodes and the melting temperatures of the metals considered for recovery. Secondly, metal ions would transfer through the interface by a chemical reaction (2.3-6) [23], as explained in previous section. As the inorganic chemical reactions are known to be faster with the increasing temperature, the exchange reaction is expected to occur relatively rapidly.

Lastly, transferred metal ions would diffuse towards the electrodes, where electrodeposition would occur on a metallic electrode. The process is shown as a graph in Figure 1.2-1 in section 1.2, and illustrated in Figure 3.2.1. below. The proposed process could be evaluated in a three-vessel setup, each vessel corresponding to each of the three main steps, or in a simpler single-vessel setup, discussed below.

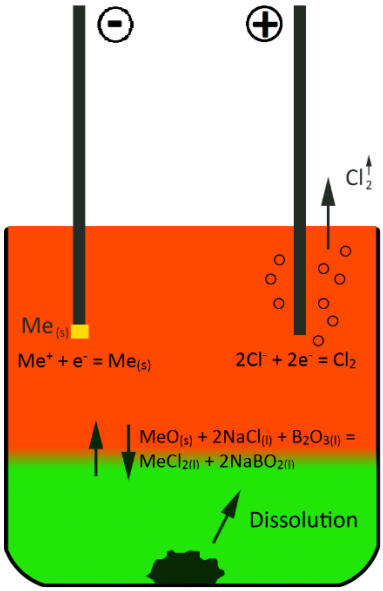


*Figure 3.2-1 Illustrative depiction of the process designed in this work. Using metal oxide pellets as the feed, the final products are pure electroplated metal and chlorine gas. The reactions ongoing (liquid-liquid interface exchange, electrolysis, etc.) are described in closer detail in text. Colours of the melt are only exemplary and will depend on the specific composition and metal feed used.*

Two potential process set-ups are suggested. In a three-vessel system shown in Figure 3.2-2, the batch is fed to the first crucible, where it undergoes melting, dissolution and pyrolysis. Borates are resistant to pollutions and water/organic residues, thus working like a buffer shielding the chlorides phase in the middle vessel. In the intermediate crucible two salt phases are in contact, creating interphase layer through which ionic exchange occurs, transporting metal cations. The last vessel is an electrolyser, in which the proper electrolysis process is conducted in the chloride melt. The final product is the metal electroplated on the negative electrode.

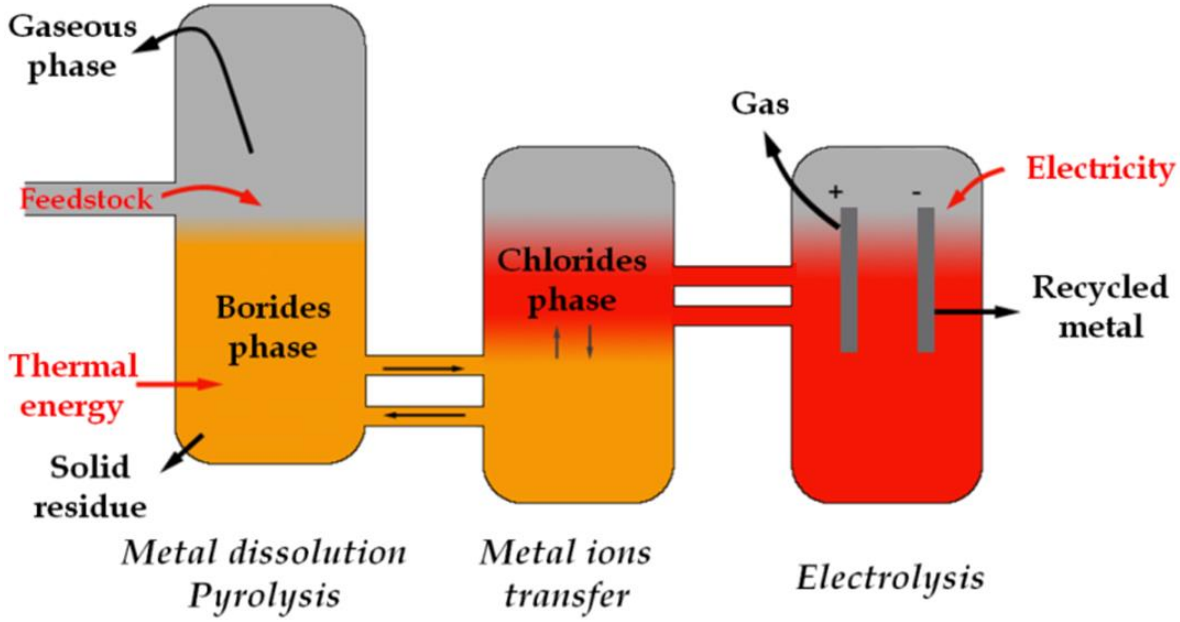


*Figure 3.2-2 The concept of a three-vessel industrial molten-salt metal recovery apparatus. Each vessel corresponds to one of the three steps, respectively: waste dissolution/metal ions extraction, liquid-liquid interface transfer, and electrolysis.*

Figure 3.2-3 represents the single-vessel concept of the process vessel. This is a simpler construction as due to no liquid flow there is no need for pumping of a high-temperature liquid and the leakage risk is significantly reduced. Such a setup would be less costly to create, and relatively more easily contained in smaller space.

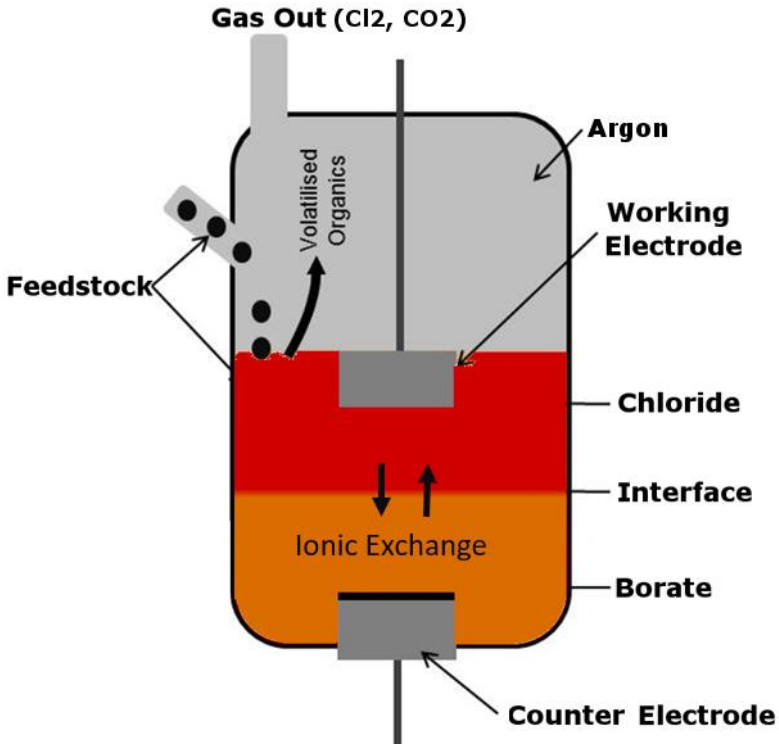


*Figure 3.2-3 Single-vessel molten-salt metal recovery apparatus concept. Unlike in the previous concept, all of the steps occur in one vessel. The division of phases occurs naturally, as the salts are immiscible. Waste feed falls to the bottom where it dissolves, metal ions diffuse and are transferred to the halide layer at the top and are electroreduced on the electrodes.*

Regarding the potential up-scale of the process, each assembly design has its benefits. As the generated heat of the process would grow with the scale, which is discussed more closely in chapter 7, it would reduce the amount of external heat required for the reactor to work [151]. Therefore, the single-vessel setup would benefit from the process heat contained within one cell, although energy balancing would be required to avoid overheating. However, keeping the vessel sealed/argon filled when feeding in the waste source would be highly challenging. Simply put, upscale of this concept would result in a more efficient energy-heat balancing, however its (semi-)continuous operation would be challenging due to the atmosphere control requirements.

When the three-vessel setup is considered, the aforementioned process heat would need to be transferred from the electrolytic cell to the metal dissolution vessel, e.g. by heat pumps. However, that vessel cold be open to air as it does not require tight atmosphere control, significantly simplifying the feed introduction process, making the (semi-)continuous process operation easier to achieve. On the other hand, separate vessel setup would imply pumping of

the salts between the chambers, risking leaks and significantly increasing the initial construction cost by introduction of the high temperature molten salt pumps. At the same time such a solution could potentially hasten the process by adding convection which would aid the otherwise diffusion-limited process, shortening the mass transfer step between the feed and the electrodes.

In summary, each concept offers different benefits and challenges when an upscale is considered, and their applicability would depend on the environment/neighbouring facilities and the needs of the region. While the lower initial cost and leakage risk of the single-vessel setup could be appealing to a smaller attempt at the recovery process, smaller setup can be sacrificed for the benefit of easier waste feed access, easier atmosphere control and cleaner product.

## 3.3. Hypotheses

In this work, a metal recovery method is proposed, offering an alternative to the current battery recycling systems. For the method to work, a number of requirements have to be fulfilled, which is the main topic of this study. The following suppositions of relevance to the process studied were formed and evaluated:

- Molten boron oxide based salts are chemically stable at high temperatures and capable of dissolving significant amounts (>5 wt%) of metal oxides representative of the rechargeable batteries waste, with the alkali metal oxides modifying the structure of the melt possibly enhancing these capabilities

- Molten borate and chloride can show a large miscibility gap due to their different ionic structure, allowing for the formation of two stable distinct layers with no need of separator enforcing the division. The liquid-liquid interface between the oxide and halide phase allows for metal ions transfer based on a chemical reaction (2.3-9) as described earlier, resulting in a metal-rich oxide layer capable of feeding the metal ions to the halide layer

- The amount of metal ions transferred to the chloride layer through the liquid-liquid interface would be sufficient for the electrolysis process, allowing for metal recovery. The metal can be therefore recovered by means of electroreduction from the two-phase molten salts system by dissolution in borate phase and electrolysis in chloride phase. The deposits obtained would be of high purity without boron contamination, proving that the liquid-liquid interface transfer can provide metal ions while not enabling the chloride and borate phases to mix

- The electrodeposition process is diffusion limited, resulting in a dendritic structure of the metals plated. Since the assembly used in this study requires no mixing, the limiting current should be correlative to the diffusion coefficient of the specific metal deposited. The dendritic deposits would allow for simple mechanical separation from the electrode enabling easy retrieval of the metal from the system.

# 4. Methodology and Equipment

To determine the most viable configuration of the electrolysis cell, salts and process parameters, a series of tests has to be conducted. Parameters like metals solubility, mass diffusion, limiting current and optimal electrical potential need to be validated, along with evaluating the thermodynamics and mechanisms of the processes involved. Due to the novelty of this solution, the data present in the literature available at the time of writing this work is lacking and many parameters are hard to predict or model, highlighting the need of the experimental validation.

## 4.1. High-temperature experimentation equipment

To evaluate the high-temperature thermodynamics of the system, two types of furnaces were used. A simple muffle furnace *Carbolite® RHF1500* with no atmospheric control, allowing for rapid extraction of the sample and cooling by liquid nitrogen quenching if required, and an atmosphere-controlled vertical-tube furnace *Carbolite® 12/300 GVA*. Both of the furnaces were fitted with resistive heating elements allowing for the temperature of 1500 (muffle furnace) and 1100 (tube furnace) degrees Celsius, controlled by *Eurotherm* temperature control units.

To contain the samples, two high-temperature crucibles were mainly used. For smaller scale thermodynamic equilibrium testing, small 12 mm diameter platinum-iridium crucibles were used (*Pt/Ir 97/3 Ögussa*). For testing requiring bigger crucibles, 100 ml alumina crucibles were used (*Coors™*).

## 4.2. Electrolytic cell set-up

In order to experimentally evaluate the feasibility of the proposed solution, a test set-up resembling the proposed industrial system needed to be constructed. By cause of the immiscibility and other properties of the salts described in the *Literature review* section, a single-vessel laboratory configuration is possible. The furnace used for the process was the *Carbolite®* tube furnace. The testing chamber size has been selected based on the possible sizes and arrangements of the electrodes used for the process. The sizes of the rest of the elements are designed in relation to the crucible and furnace tube sizes. The tests were conducted inside a gas-tight *Inconel®* tube, with the atmosphere controlled through pipes connected at the water-cooled brass top plate. The heavier argon displaces air out of the testing chamber, allowing for $O_2$ levels as low as 50 ppm. The electrolysis occurred in an alumina

crucible (*Coors™*, 100ml) with the melt, precisely 35 g of sodium borate ($Na_2O$-$2B_2O_3$, *Sigma-Aldrich®*, anhydrous, >98.0 %) and/or 65 g of sodium chloride (NaCl, *Sigma-Aldrich®*, *Redi-Dri™*, anhydrous, >99 %), and metal chloride or metal oxide pellet inserted at the bottom, depending on the test conducted. The borate salt was allowed to equilibrate with the metal oxide prior to adding the chloride phase, following which it was equilibrated again for 1 h directly before the tests. The salts were gravitationally arranged, with the lighter chloride salt (1.50 g/cm$^3$)[152] on top of the borate (2.06 g/cm$^3$)[153]. The process is mainly diffusion controlled, however natural heat convection can happen which would promote faster equilibration. The specific composition depended on the test configuration, shown in Figure 4.2-1 and 4.2-2 for single- and two-phase electrolytic cell respectively.

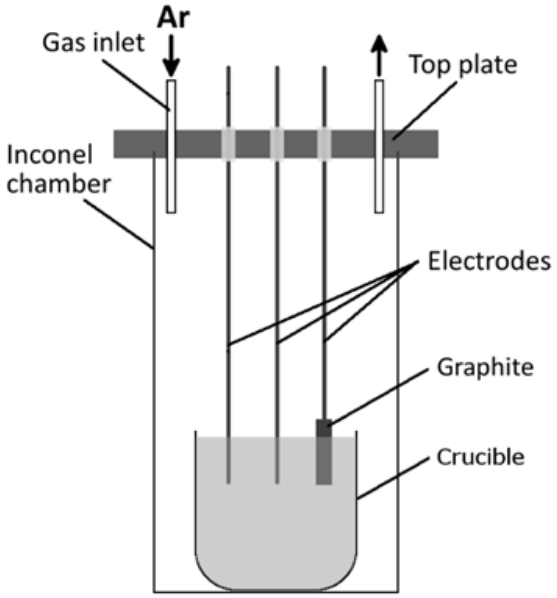


*Figure 4.2-1 Single-phase electrolytic cell*

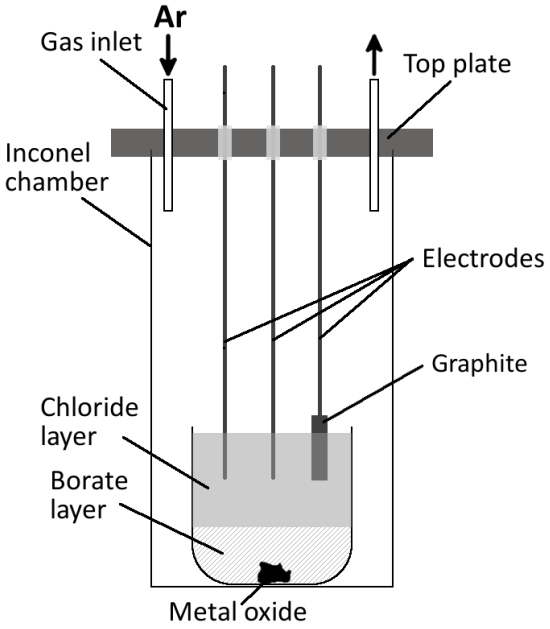


*Figure 4.2-2 Two-phase electrochemical cell*

Electrodes used in the process were selected depending on their chemical, thermal and corrosion resistance, and low thermal expansion essential for high-temperature testing [115,117–120]. Plating was performed on a 2 mm tungsten rod used as the working electrode (WE), the counter electrode (CE) was a 6 mm graphite cylinder screwed onto a stainless steel current collector. As a quasi-reference electrode (QRE) a tungsten rod (2 mm diameter) was adopted. The electrode surface area depended on the rod immersion level and was assessed after every test. The average value varied around 0.3 cm$^2$. The electrodes were in equidistance to the reference electrode with ~1.7 cm between them. The electrodes were cleaned and polished with successively finer grades of silicon paper until a mirror-like surface was

obtained before every test. The graphite blocks were treated as one-use consumable to avoid cross-contamination. Electrode fittings were machined from *MACOR*® machinable ceramics for the electrical and thermal insulation.

While parts of the system can work under open air atmosphere, the chamber has been made gas tight to allow for gas control. This also enables exhaust gas collection and control. The furnace tube is supported by a thermal brick, in order to contain the crucible at the centre of the furnace hot zone. The gas leaving the furnace needs to be cooled down before it reaches the plastic tubing, for which purpose a copper coil has been connected directly to the top plate gas outlet. Finally, a probing hatch allows for the access to probe and/or observe the melt. CAD drawings of the custom made assembly elements are shown in the Appendix 1. Figure 4.2-3 shows a complete working assembly.

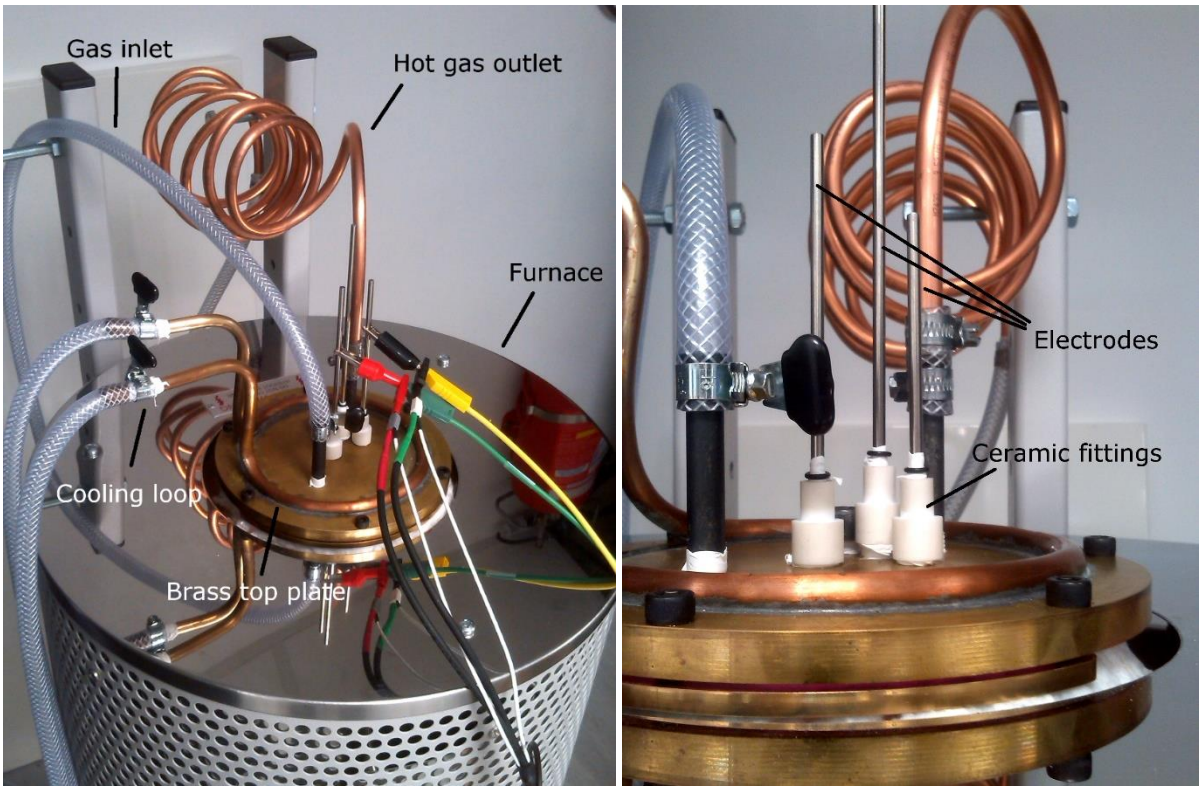


*Figure 4.2-3 High temperature electrochemical assembly photography. Visible are the top plate with water cooling loop, gas cooling coil and, gas connections and potentiostat wires connected to the electrodes*

For the electrochemical measurements, i.e. chronoamperometry, cyclic voltammetry, linear sweep voltammetry, the potentiostat used was *10A/VersaSTAT 3* which is a boosted version of *VersaSTAT 3* by *Princeton Applied Research*, with the *KEPCO* power source/booster. The range of the apparatus is ±10 amps at ±20 volts in the boosted mode and ±650 mA at ±10 V

maximum in the normal (non-boosted) mode, on a single 3-electrode channel. The software used for the control of the potentiostat was *VersaStudio 2.42.3* on a PC connected to the channel through a USB wire.

## 4.3. Characterisation techniques

### 4.3.1. Chronoamperometry

A constant voltage method, where the current is recorded as a function of time is called chronoamperometry. Through chronoamperometry, electroreduction processes can be evaluated regarding their current stability or electroreduction kinetics [114]. It is also commonly used as an industrial scale electroplating/electrolysis method [39], and similarly it was used for this project for metal electrodeposition. To ensure the removal of the initial surface concentration of the reagent to allow the process kinetics analysis [125], evaluated metals were plated at the potential value higher than the peak value obtained with the use of Cyclic Voltammetry.

The tests were conducted using *VersaSTAT 3* potentiostat (*Princeton Applied Research*) with 10 ampere booster (*Kepco*) in a three electrode setup, controlled by *VersaStudio* software. The test parameters were selected depending on each sample and the desired effect.

### 4.3.2. Cyclic Voltammetry (CV)

To observe the electrochemical reduction reaction kinetics, cyclic voltammetry (CV) can be applied. CV is a measurement method recording electrode currents as a function of the voltage applied to the electrolysis cell. It is commonly used to observe the reaction kinetics, i.e. reduction potentials and reversibility. Figure 4.2-1 represents a typical CV profile. The scan rate used for the considered investigation was 100 mV $s^{-1}$ and constant across all tests for the repeatability, unless stated otherwise. The analysis of current/voltage curves can provide essential information about the process dynamics and step characteristic [154,155]. Exemplary literature CV scans are discussed in section 2.3.3.3. The tests were conducted using *VersaSTAT 3* potentiostat (*Princeton Applied Research*) with 10 ampere booster (*Kepco*) controlled by *VersaStudio* software, in a three electrode setup.

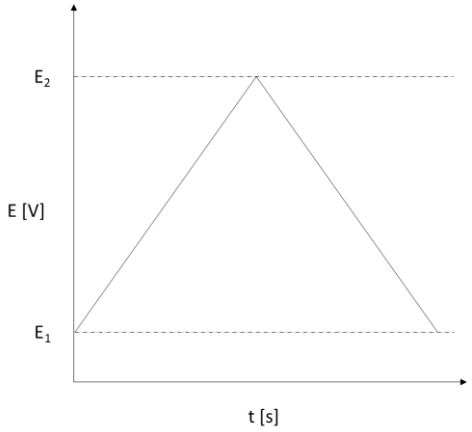


*Figure 4.3-1 CV single scan profile – the scan is repeated for a defined number of cycles*

### 4.3.3. Differential Scanning Calorimetry (DSC)

Differential Scanning Calorimetry (DSC) thermal measurements evaluates the difference in temperature between the sample and an inert standard reference during a programmed heating or cooling regime. Therefore, a difference between the enthalpy-temperature relation of a sample and the standard reference is observed. As a result, the enthalpy variation can be observed during the heating/cooling process, providing information about a possible physical and chemical reactions occurring in the sample [156].

The DSC apparatus used was DSC-TGA *Simultaneous Thermal Analyser NETZSCH STA 449 F3 Jupiter* with a silicon-carbide furnace with the maximum working temperature of 1650 $^{O}$C. The stage was calibrated against melting points of known pure metals. The DSC was used to obtain information on the phase changes in the evaluated glass forming salts.

### 4.3.4. Inductively Coupled Plasma (ICP) Optical Emission Spectroscopy (OES)

Metals can be analysed qualitatively and quantitatively using the Inductively Coupled Plasma Optical Emission Spectroscopy (ICP-OES). It uses a radio-frequency induced argon plasma, which vaporises the injected liquid sample and energises it through collisional excitation at high temperature. Excited atoms emit radiation at specific wavelengths, which intensity depends on the concentration of each element. This allows for rapid and precise identification and quantification of the elements present in the sample [157]. The analysis for this project was outsourced to an external company *Exeter Analytical (UK) Ltd*, Warwick Analytical Services division.

### 4.3.5. Scanning Electron Microscope (FEG-SEM) with X-ray Energy Dispersive Spectroscopy (X-EDS)

Samples were analysed using FEG-SEM (*Carl Zeiss Gemini*®) with X-ray Energy Dispersive Spectroscopy (X-EDS, *Oxford Instruments*®) and Electron Backscatter Diffraction (EBSD). This analysis was used to assess the chemical composition, metals distribution and concentration across the sample. X-EDS can determine the presence and quantity of chemical element by detecting X-rays emitted from atoms, specific for each element. X-rays are released when a beam of accelerated electrons hit the atoms present in the sample undergoing evaluation. Measured energy of the X-rays emitted enables chemical identification. X-EDS is a quasi-quantitative analysis, allowing for proportional analysis; however, facing difficulties

in the detection of light atoms, like boron. Backscatter electron image mapping included within the same analytical apparatus allows for uniformity confirmation of the elements distribution across the sample, which indicates whether the samples analysed were at the compositional equilibrium state with the metals concentration uniform throughout the bulk matter [145].

Parameters of the FEG-SEM X-EDS during the analysis were as follows, unless stated otherwise: EHT 20 kV, aperture 60 µm, high current enabled, carbon coating.

### 4.3.6. X-ray Computed Tomography (X-CT)

A non-destructive post-mortem evaluation of the recovered metal deposits in 3D was done using X-ray Computed Tomography (X-CT). In this method, emitted X-rays travel through the sample and are either attenuated or pass through. Grey-scale image is produced by a detector on the other side of the sample, collecting the passing X-rays. Darker regions correspond to the denser areas of the sample. Images were taken through 360 degrees that were then reconstructed using filtered back projection to produce a 3D volume of the sample for evaluation [158,159]. The CT system used in this project was the *Zeiss Versa 520* with the parameters selected to provide the optimum image and magnification for each test conducted. The detector used was a Charge-Coupled Device (CCD) consisting of a 2000 *x* 2000 pixel array.

### 4.3.7. X-ray Diffraction (XRD)

To determine the crystal structure of the materials, and thus the chemical compounds constituting the sample, X-ray diffraction analysis was used. The X-ray beam scans the sample at a range of angles, counting when constructive interference of the diffracted beams occur. This happens depending on the crystal lattice parameters, which allows for phases identification thanks to the *Bragg's Law*, which defines the relation between the two. Interference peaks are then registered against the beam angles for identification of the phases present in the evaluated sample [145]. The COD database (Crystallography Open Database) was used for phases identification.

The instrument used was PANalytical Empyrean X-ray Diffractometer with a cobalt source. The scan was evaluated on a spinning stage with the parameters as follows, unless stated otherwise: Scan range 8-100 °2Th, step size 0.013 °2Th, scan step time 2000 s, cobalt X-ray source.

### 4.3.8. X-ray Photoelectron Spectroscopy (XPS)

X-Ray Photoelectron Spectroscopy (Axis Ultra DLD, *Kratos*®) was used to cross-confirm the metal solubility in evaluated samples. XPS works by analysing the electrons ejected from the electron shell of an atom, as a result of X-ray photon absorption. The binding energies of the electrons to the atoms have characteristic, fingerprint values allowing for identification of each chemical element. As in X-EDS method, XPS allows for elements quantification by comparing detection peaks intensity, directly related to chemical concentration [145].

# 5. Experimental section

## 5.1. Molten salts thermodynamics

### 5.1.1. Borate salts melt preparation and optimisation

As previously described, the salt system selected as a suitable one for this project has not been closely evaluated. The most significant gaps in knowledge are located around the borate salts, and subsequently two-phase system, which forces the author to focus on them primarily. The basic thermodynamics of borate melt behaviour and alkali metal additions influence needs to be evaluated accordingly, before the electrochemical testing could be commenced.

As was described in section 2.3.2. borate salts can show significant wetting phenomena, which can lead to loss of sample mass/creeping out. This has been reported by other researchers for borate-rich salts and described as challenging to study [91,160], The behaviour of the sample (boron oxide $B_2O_3$, *Alfa-Aesar*, 99%) during heating and melting caused surprisingly high loss of mass, with the melt pouring out of the test vessel. This issue had to be resolved in order to be able to create a usable set-up, which will not lose the test sample. The case of the spillage was evaluated and the optimised heating regime was established in order to enable testing with the borate-rich salts considered in this study.

**Test procedure**

The following "fast" and "slow" heat treatments, Figure 5.1-1 and 5.1-2 respectively, were repeated in a range of crucibles: carbon (glassy carbon crucible, *Sigradur® G series*), alumina (cylindrical alumina crucible, *Fisher Scientific International®*) and platinum (*Ögussa*).

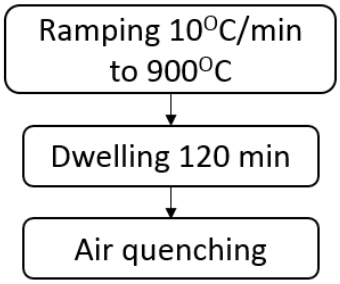


*Figure 5.1-1 Fast heating regime testing diagram*

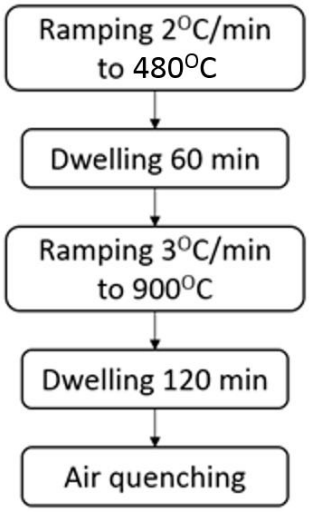


*Figure 5.1-2 Slow heating regime testing diagram*

Analysing the observed sample mass loss phenomena, a number of mechanisms of the sample escape has been proposed, driven by physical or thermodynamic processes:

- Capillary wetting (due to the alumina crucible porous wall surface)
- Reaction driven wetting (reacting with the active sites on the graphite crucible walls)
- Moisture boiling out of the sample (possibility removed by using anhydrous salt)
- Foaming (due to gas trapped in the powder during sample packing and glass transition)

For the better understanding of the salt-escaping mechanism, a visual of the process has been recorded. To enable the observation, a set-up consisting of a brass top-plate with a see-through hole, a mirror and a heat-resistant goose-neck camera was used, as shown in Figure 5.1-3.

*Figure 5.1-3 Salt behaviour visual observation setup*

Additionally, differential scanning calorimetry (DSC-TGA, *Simultaneous Thermal Analyser NETZSCH STA 449 F3 Jupiter*) was used to correlate the observable changes with thermochemical processes, i.e. phase transformations. Results of the testing conducted are discussed in the Chapter 6.

### 5.1.2. Metal oxides solubility in borates and the borate-chloride system evaluation

The solubility of specific metal oxides ($Co_3O_4$, $Cu_2O$, CuO, NiO and $Mn_2O_3$) in molten alkali borates ($B_2O_3$, $Na_2O$-$2B_2O_3$ and $K_2O$-$2B_2O_3$) has been evaluated at a temperature of 900 $^{O}$C under atmospheric conditions. The concentration and distribution of the dissolved metal ions were determined using X-EDS and XPS elemental analysis, as well as backscatter electron image mapping.

#### Samples preparation

Metal oxide pellets were formed from metal oxide powders [NiO (99,8 %, <50 nm particle size), $Co_3O_4$ (99,5 %, <50 nm particle size), CuO (98 % <425 µm particle size), $Mn_2O_3$ (99 %, <44 µm particle size) from *Sigma-Aldrich*® by compressing for 1 minute under 1 tonne of pressure in a 13 mm diameter die. After pressing the pellets were sintered (NiO preform was sintered in 800 $^{O}$C for 5 h, $Co_3O_4$ in 900 $^{O}$C for 5 h, $Mn_2O_3$ in 900 $^{O}$C for 17 h and CuO in 1050 $^{O}$C for 4 h) each metal oxide on a separate alumina boat in order to avoid cross-contamination. Metal oxides stability was evaluated prior to the testing with the use of the *FactSage*™ thermodynamic suite (*Reaction module*) [24], and further supported by literature research [161–163], as described in the *Literature review* section. The starting metal oxides structure was confirmed using XRD *(PANalytical Empyrean X-Ray diffractometer)*. The sintered pellets were furnace-cooled to room temperature to avoid cracking due to thermal shock. $Cu_2O$ (>99 % as confirmed by XRD analysis) pieces were obtained by oxidizing copper rod (5 mm) in 900 $^{O}$C in air. Sintering times and temperature were selected based on each material thermal properties to obtain hard pellet without decomposing the material. The pellets were shaped to fit the test crucibles using high-speed precision saw with high-density diamond blades.

**Solubility test procedure**

Platinum crucibles were used (*Ögussa*®, Pt/Ir 3 % mini crucible), filled with either $B_2O_3$ (*Alfa Aesar*®, 99 %), $B_4Na_2O_7$ *(Sigma-Aldrich*®, ≥99.5 %) or $B_4K_2O_7$ (*Sigma-Aldrich*®, ≥99.5 %) depending on the test conducted. The metal oxide quantity in the crucible was based on the solubility prediction made with FactSage™[24] thermodynamic suite [*FactSage*™ 6.4, FToxid database was used], using the *Phase Diagram* module of the software. This step is more closely explained in section 2.3.2.2. However, as the database is lacking experimental data regarding borate salts, as was mentioned in the literature review, the simulations were not fully reliable. Hence, the values presented by the model were increased in order to ensure that enough material was present for the dissolution process. Crucibles with the test samples were placed in thermal brick holders manually shaped for added stability and placed in a muffle furnace. The test procedure is represented in the Figure 5.1-4.

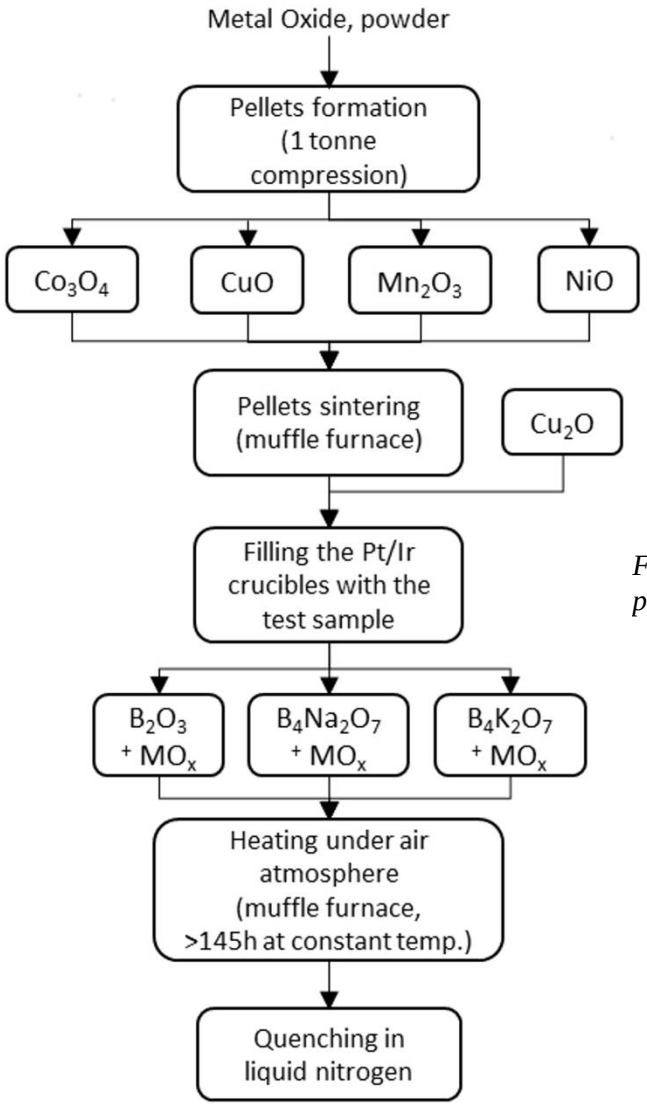


*Figure 5.1-4 Test procedure flowchart*

To avoid the borate salt foaming and loss of the sample, specific thermal cycle needed to be introduced, as borate-rich salts have been reported as likely to show loss of mass due to the sample escaping the test vessel [160]. This has been overcome by the author by introducing a slow heating regime with a dwell step, as described in the previous section. The heating procedure used for these experiments is shown in Figure 5.1-5. Samples were preheated to 480 $^{O}$C at 2 $^{O}$C/min, kept for constant temperature for 60 minutes to allow sample de-gassing, and finally heated to the desired testing temperature of 900 $^{O}$C or 1050 $^{O}$C at 3$^{O}$C/min, depending on the test.

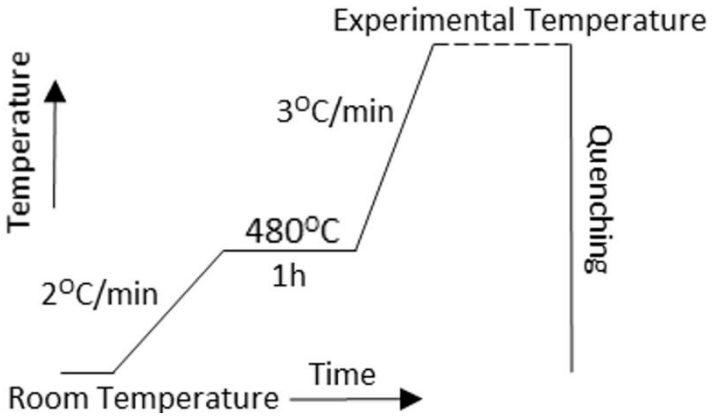


*Figure 5.1-5 Temperature profile of the experiment*

Samples were kept at constant temperature of 900 $^{O}$C or 1050 $^{O}$C for at least 145 hours to reach the equilibrium. Afterwards, the samples were quenched in liquid nitrogen to instantly stop the process and avoid metal precipitation. No atmosphere control was enforced as the crucibles were open in air, similarly to other studies [23].

The quenched samples were analysed using FEG-SEM (*Carl Zeiss Gemini*®) with X-ray Energy Dispersive Spectroscopy (X-EDS, *Oxford Instruments*®) and Electron Backscatter Diffraction (EBSD). This allowed to assess the metal distribution uniformity and concentration. Backscatter electron image mapping was used to confirm the uniformity of the metal distribution in the sample, indicating the sample thermodynamic equilibrium state at the time of quenching. This results in uniform metal concentration throughout the glass sample, and allows for obtaining representative results by evaluating any fragment of the glass. X-Ray Photoelectron Spectroscopy (Axis Ultra DLD, *Kratos*®) has been used to cross-confirm the increased solubility in the $Na_2O$ doped samples when compared to pure $B_2O_3$ solvent case.

X-EDS has been used by other researchers for quantitative analysis and reported in literature [164–167]. When the electron beam hits the sample, a pear-shaped interaction volume is

formed, with its depth varying from nanometres to microns, depending on the material used and the acceleration voltage applied [168]. The X-rays analysed with the EDS detector come from the lower part of that pear-shaped volume, therefore providing bulk-analysis rather than the surface composition. The interaction depth can also be calculated, e.g. using the Monte Carlo simulations [169]. Material evaluated in this work is highly polymeric [51] and the selected acceleration voltage of 20 kV relatively high [145], therefore the penetration depth is expected to be relatively high.

As the samples are sensitive to water, a thin film of hydroxide can be formed on the layer when exposed to moisture, therefore extreme care should be taken when such transporting the samples, preferably directly after the samples preparation. Samples in this work were polished using oil-based solutions and covered in oil to be cleaned only prior to analysis.

**Metal ions distribution evaluation in the two-phase system**

To evaluate the metal partition between the borate and the chloride phase, the following test was conducted. The test was similar to the previous experiment, with the following differences; the salt selected for the highest metal solubility during the previous experiment, $B_4Na_2O_7$, was pre-melted with a metal oxide pellet (NiO, $Co_3O_4$, CuO or $Mn_2O_3$) and left to equilibrate. After quenching, the crucible was topped with NaCl and the procedure was repeated. Figure 5.1-6 represents the experiment flowchart.

The samples obtained were analysed using FEG-SEM X-EDS as previously described, and also an X-ray Diffraction apparatus. As the interface between the two immiscible salt phases remains clearly defined after the solidification, it was possible to easily separate the oxide layer from the chloride one. Unlike the glassy borate salt, the chloride layer was highly crystalline, which allowed for an X-ray Diffraction analysis. The instrument used the *PANalytical Empyrean* X-ray Diffractometer. The scans were conducted on a spinner stage in a range of 8-100 2θ angles, using cobalt X-ray source. The database used for phases identification was *Crystallography Open Database* (COD). Results of these experiments are discussed in the following chapter 6.

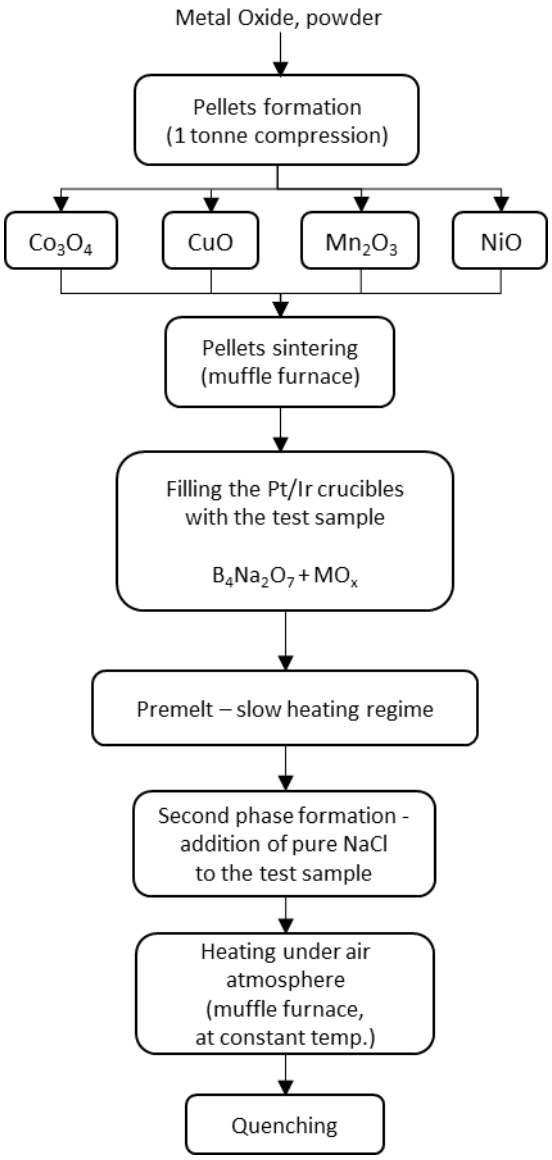


*Figure 5.1-6 Two-phase system metal partition test flowchart*

## 5.2. Electrochemical measurements

### 5.2.1. Metal recovery by electrodeposition from a two-phase molten salt cell

The electrochemical recovery method of Co, Cu, Mn and Ni from a two-phase electrolytic cell was characterised through voltammetry and chronoamperometry. The two immiscible phases in the electrolytic cell were molten NaCl and $Na_2O$-$2B_2O_3$ at 1173 K. The metal feedstock used for the recovery was either metal chlorides or metal oxides of Co, Cu, Mn or Ni. Metals were recovered successfully in the form of plated metal deposits, and the formal potentials of the redox reaction were obtained. Thermodynamic process differences between the cells were analysed. The purity of the metal deposits was evaluated.

The objective of this particular section was to assess whether the two-phase sodium borate-sodium chloride system is capable of providing the metal ions from the oxide phase while preserving the desired electrochemical attributes of the chloride layer, i.e. electrochemical stability, and to compare the system with a single-phase cell containing molten sodium chloride. The two-phase cell system would enable the recovery of high purity metals by electrodeposition from the sodium chloride molten salt, while at the same time benefiting from the sodium borate phase allowing for various metal sources use as the process feed.

**Test procedure**

The basics of the experimental set-up are explained in section 4 of this work. Two-phase electrolytic cell set-up was used. Metal oxides were used as the feed, present in their most stable form [24,162] at the experimental temperature of 900 $^{O}$C: NiO (*99,8 %*), $Co_3O_4$ (*99,5 %*), CuO (*98 %*) and $Mn_2O_3$ (*99 %*) from *Sigma-Aldrich*®. All the metals were tested separately.

Alternatively, to enable comparison to a single-phase chloride-only electrolysis cell was used. The chlorides used were as follows, selected for their stability in the test environment: $NiCl_2$ (*>99.0 %*), $CoCl_2$ (*>99.0 %*), $CuCl_2$ (*>99.0 %*) or $MnCl_2$ (*>99.0 %*) from *Sigma-Aldrich*®. As metal chlorides were used instead of metal oxides, there was no liquid-liquid oxide-chloride interface present.

### Electroplating

After filling the test chamber with argon, the assembly was dried at elevated temperature for 24 hours prior to melting. The experimental temperature of 900 $^{O}$C was achieved at a rate of 10 $^{O}$C min$^{-1}$, and at least 1 hour was given for equilibration at constant temperature. After melting the mix was cleaned with a CV sweep between 0 – 1V at 100 mV s$^{-1}$, after using which the background curve presented in section 6.3. was obtained as well, validating the cleanliness of the system. Due to the constraints of the assembly, the reagents have to be present from the beginning of the test, limiting the amount of possible pre-processing. Background current achieved, as is explained in section 6.3, was around the level of 5 mA.

Cyclic voltammetry was applied in order observe the electrochemical redox reaction thermodynamics. The CV scan rate applied was 100 mV s$^{-1}$, which is a balanced choice commonly used in molten salts electrochemistry [125,128], as was mentioned in section 2.3.3. At higher sweep rates the nucleation step starts to have higher influence on the process as observed by Hills et al. [129], while at lower scan rates the current passing through the electrode become significant which may result in changed morphology of the electrode, e.g. formation of significant dendrites. A slower, 10 mV sweep rate scan was also evaluated. The current vs voltage curves provide essential information on the process dynamics and steps characteristics [154,155]. The obtained electrolysis potential values were compared against thermodynamic values to enable deeper analysis of the system evaluated. Metal was then deposited potentiostatically at the reduction potential value higher by around 200 mV than the peak value observed using the CV analysis, in order to remove the initial surface concentration of the reagent. While this is a common practice [125], one has to be aware that applying significant overpotentials can further perpetuate the diffusion-control of the process, as described in section 2.3.3.3.

### Post-mortem analysis

After the electrodeposition the electrodes were lifted and cooled under argon atmosphere, to limit re-oxidation. The metal deposits were analysed using FEG-SEM (*Carl Zeiss Gemini*®) with X-ray Energy Dispersive Spectroscopy (X-EDS, *Oxford Instruments*®). This allowed for both chemical identification [145] and optical analysis of the samples.

### 5.2.2. Mechanistic analysis of electrodeposition from the molten salt cell

This metal electro-recovery process limiting step and the deposited metals structures were analysed. The diffusion is expected to be the slowest step of the process, as explained in section 2.3.5. This results in a dendritic deposition of the metals, which influences the electrode surface area.

The following experimentation analyses the increasing electrode surface area and the electric current changes in case of copper and silver electrodeposition. Copper is expected to grow dendritically on the electrode in the current system [51,125,126], while silver is plated as a molten phase, removing the rapid surface growth effect. The surface area change will be quantified using the X-ray Computed Tomography (X-CT), Cottrell equation and Stokes-Einstein diffusion model, which allows for correlation analysis with the electric current change observed during the chronoamperometric plating process.

**Test procedure**

The experimentation was carried out in a vertical tube furnace with controlled atmosphere, as described in the *Methodology and Equipment* section, using the single-phase electrolytic cell setup. Alumina crucibles were filled with the sample consisting of the sodium chloride and the relevant metal chloride in its most stable form, respectively $CuCl_1$ (*>99.0 %*) and AgCl (99.999%) from *Sigma-Aldrich®*. All the metal chlorides were evaluated separately, at similar concentrations of ~0.11 M for the comparativeness of tests.

For the needs of this specific testing, planar flat-disc electrodes were made for the simplification of the diffusion analysis, and for the compliance with the assumptions of the Cottrell equation. The small surface flat-disc electrodes were produced manually using 2 mm tungsten rods and alumina paste (*Ceramabond™ 569*). The flat tip of the electrode was cleaned and polished before each test until a mirror-like surface was obtained. The resulting flat-disc electrodes had the working surface area of a 2 mm diameter circle ~ 0.0314 $cm^2$.

Metals were plated potentiostatically, at the temperature of 900 $^{O}C$ and 1000 $^{O}C$ for copper and silver case respectively. This way copper was deposited as a solid, while silver created a layer of liquid metal. The electrodes were under constant electric potential of the evaluated metal peak reduction potentials, obtained as explained in the previous section, plus around 200 mV to remove the initial surface concentration effect.

The method of electroplating at a potential value higher than the peak reduction potential has been used by other researchers [125], in order to eliminate the surface concentration effect and potential kinetic effects present before the peak reduction potential. However, it has to be mentioned that such a significant overpotential can further perpetuate diffusion effects, such as dendritic growth, and cannot be done in case of multiple metals present in the melt as could result in co-deposition.

**Diffusion values calculations**

Diffusion coefficients were obtained using the Stokes-Einstein equation [170]. This diffusion model assumes a diffusion of a sphere as a simplified description of a metal ion, and derives from the Fick's first law of diffusion. With the above assumption, the following equation 4.4-1 can be obtained for spherical particles moving in a medium made of proportionally small molecules, e.g. high-temperature molten salts. The Stokes-Einstein Law for Diffusion in Solution is a specific case of the Einstein-Smoluchowski relation[171], which is accurately describing the system defined above, and is relevant to our case of metal ions in molten sodium chloride.

$$D = \frac{kT}{6\pi\eta r} \tag{4.4-1}$$

where: $\eta$ – dynamic viscosity $[Pa\ s]$, $k$ – Boltzmann's constant $\left[\frac{m^2\ kg}{s^2\ K}\right]$, $r$ – particle radius $[m]$ and T – temperature $[K]$.

The thermodynamic values required for the calculations were taken from the literature [172,173]. With the aforementioned assumptions, the following parameters were used for the calculations: $\eta$ = 0.871*10$^{-3}$ $[Pa\ s]$, $k$ = 1.3807*10$^{-23}$ $\left[\frac{m^2\ kg}{s^2\ K}\right]$, $r$ = 7.3*10$^{-11}$ $[m]$, $T$ = 1173 $[K]$, $D$ = 1.35*10$^{-4}$ $[cm^2\ s^{-1}]$. The resulting value was: $\boldsymbol{D = 1.35 * 10^{-4}}$ $[\boldsymbol{cm^2 s^{-1}}]$

The obtained values are comparable to the diffusion coefficients reported in the literature for similar metals in the same medium [142]. The experimental diffusion coefficient values for other transition metals vary around 10$^{-5}$ and 10$^{-4}$ $[cm^2\ s^{-1}]$ in molten halides. This confirms that the evaluated system complies with the Stokes-Einstein diffusion model assumptions. The obtained diffusion coefficient values were used as input for the Cottrell equation, as will be explained in the following section, which allowed for the comparison of the experimental and theoretical electrode surface area increase.

### Cottrell equation

Cottrell equation (4.4-2) has been reportedly used for the evaluation of the diffusion behaviour in molten electrolytes, in conjunction with chronoamperometry [124,125,143].

$$I = \frac{nFAc^{\infty}\sqrt{D}}{\sqrt{\pi t}} \tag{4.4-2}$$

where: $I$ – current [$A$], $c^{\infty}$ – analyte bulk concentration [$mol\ cm^{-3}$], $n$ – amount of electrons exchanged, F – Faraday constant [$C\ mol^{-1}$], $A$ – electrode area [$cm^2$], $D$ – diffusion coefficient [$cm^2\ s^{-1}$] and $t$ – time [$s$].

Equation (4.4-2) can be used to calculate the surface of the electrode if the diffusion coefficient is known, as shown by equation (4.4-3).

$$A = \frac{I\sqrt{\pi t}}{nFc^{\infty}\sqrt{D}} \tag{4.4-3}$$

It needs to be noted that electrochemical measurements can be influenced by the side reaction and other effects, such as the nucleation phenomena and deposition of a metallic phase [125]. In case of too high sweep-rate cyclic voltammetry, significant deviations can be caused by the deposits failing to create nucleation sites, which would result in a peak reduction potential shifts towards more cathodic values. In chronoamperometric methods, parallel reactions cannot be separated from the collected electric current data, which requires a highly clean testing environment to avoid co-deposition of other elements. Other electroanalytical method show similar challenges [125]. Thus, experimental values can show some deviation especially in case of high-temperature complex systems. However, the system considered is relatively simple chemically and still directly dependant on the diffusion, allowing for the required correlation analysis.

### Post-mortem analysis

After the electrodeposition, the electrode rods were lifted and argon cooled. Formed deposits were retrieved from the electrodes mechanically and analysed using FEG-SEM (Carl Zeiss Gemini®) with X-ray Energy Dispersive Spectroscopy (X-EDS, Oxford Instruments®) to identify the elements electroplated. X-EDS allows for both chemical identification and quantification, based on the energy of the X-rays emitted and the observed peaks intensity [145].

Non-destructive observation of the dendritic metal deposits was available using the X-ray Computed Tomography (X-CT). Images were taken through 360 degrees and reconstructed using filtered back projections, resulting in a 3D volume representation of the sample [158,159]. The X-CT system used was *Zeiss Versa 520* with the parameters shown in Table 4.4-1. The selected parameters provided the optimum image and maximum magnification while keeping the sample within the field of view. CCD detector consisting of 2000 *x* 200 pixels in conjunction with a 0.4*x* optic allowed for a 5.3 micron voxel size while analysing the deposited metallic dendrites. The 3D volume models obtained were used to evaluate the dendritic deposits structure, and to calculate the surface/volume ratio. This allowed for further calculations, i.e. correlation of the theoretical electrode surface increase over time with the observed electric current increase.

*Table 5.2-1 X-CT scan parameters*

| | |
|---|---|
| Voltage (kV) | 140 |
| Current (μA) | 72 |
| Source/sample distance (mm) | 22 |
| Sample/detector distance (mm) | 120 |
| Exposure (s) | 1.0 |
| Voxel size (μm) | 5.3 |

# 6. Results and Discussion

The following results sections are reflecting the layout of the experimental section, that is – it follows the steps of the metal recovery process studied. From the molten borates behaviour and metal oxides dissolution, through the analysis of the electroreduction process thermodynamics to the evaluation of the deposited material. The latter half of this chapter examines the thermodynamics of the melt, while the latter discusses the electrochemistry of the process and the deposits produced. The limiting parameters of each step were identified, some optimisation was introduced and potential engineering solutions were suggested. The subsequent chapter 7 considers the costs of the process and attempts a simplified feasibility study.

## 6.1. Borate salts pre-melt optimisation

In this subsection, the stability of borate salts at elevated temperatures is considered. The thermostability of the system is essential for the process studied, although the borate salts were reported to pose certain difficulties in containing within a test vessel and a mass loss was observed by other researchers [160]. A proper heating procedure needs to be established to avoid the mass loss of the bulk salt.

The specific heating regimes were evaluated and the resulting sample behaviours were analysed. The fast-heating regime was found to cause the loss of the salt ($B_2O_3$ as well as $Na_2O$-$2B_2O_3$) resulting in the salt misplaced from the crucible to the surrounding thermal brick forms. Similar result was observed for all the crucible materials evaluated. A slow heating regime was evaluated using the same crucibles range, resulting in zero mass loss of the salt during the pre-heating stage, for each of the materials considered. When compared with the fast heating regime, the temperature increase step time is significantly longer extending the process time; however, the uncontrolled test sample loss is averted and the salt is retained within the test cell.

During the visual observation of the pre-heating process, it has been found that the salt is foaming out at around 480 $^{O}$C. When the foaming was noticed, the furnace was rapidly lowered to allow for air-quench of the sample. The resulting sample in the foaming state can be seen in Figure 6.1-1.

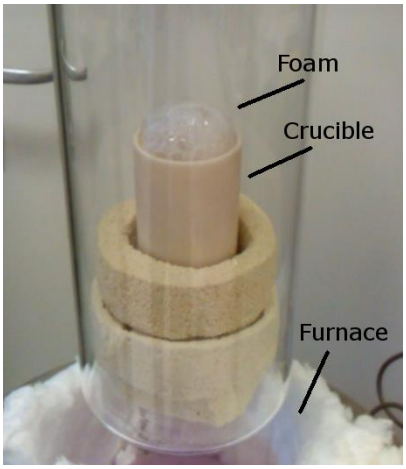


*Figure 6.1-1 Alumina crucible with borate salt foaming out. The picture was taken after the sample started foaming out (around 480 $^{O}$C) by rapidly lowering the furnace and exposing the sample.*

This correlates with the DSC measurement showing a significant endothermic shift at that temperature, which is ascribed to the glass transition process [174]. It is known that the glass transition temperature can depend on the temperature change rate, although weakly, thus the testing was commenced with the constant rate of 10 K/min, as is commonly used. The obtained DSC curve is shown in Figure 6.1-2.

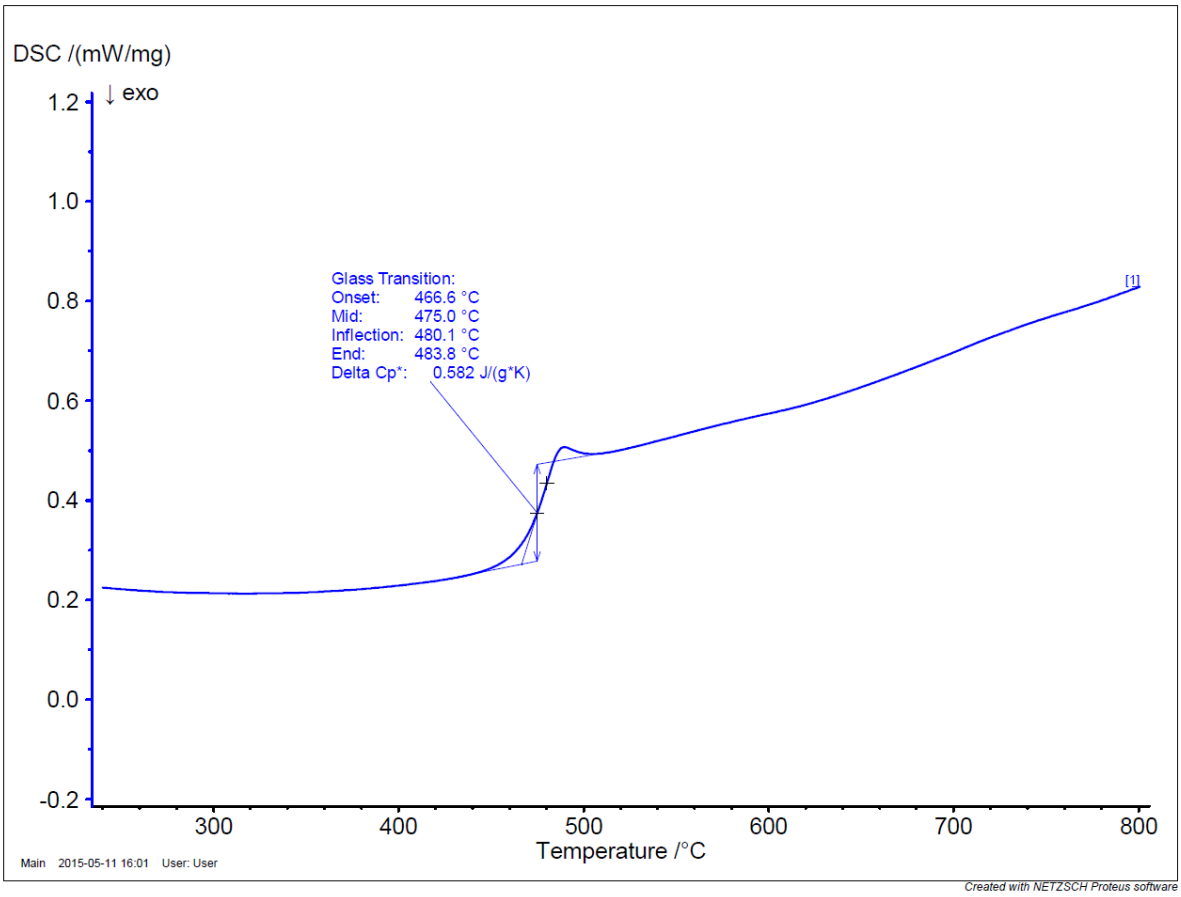


*Figure 6.1-2 DSC curve of the sodium borate salt. Phase transition step is clearly visible in the middle of the scan. Heating rate of 10 K/min was used*

It has been established that the sample foaming phenomena was the main reason for the sample mass loss, and in order to enable work with the borate salts the foaming has to be avoided. It can be achieved by introducing the slow heating regime with the dwell step at around 480 $^{O}$C, which allows for the sample outgassing during the glass transition/early melting stage. In consequence, the temperature increase step of the process takes longer time; however, it is essential for the optimal use of the borate salt for high temperature processing.

The thermostability of the salt was confirmed, and the mass loss reported by other researchers was successfully prevented. The established temperature increase profile was used for the subsequent experimentation, as described in section 5.1.2.

## 6.2. Metal oxides solubility in selected molten borate and borate-chloride systems

The following subsection evaluates the hypothesis of high metal oxide solubility in borate salts, and the influence the alkali metal oxides have on the metal affinity of the borate phase. The metal ions could then transfer to the halide phase through the liquid-liquid interface, resulting in a concentration dictated by the partition coefficients specific to the system studied. The metal ions concentration in the melt is important for the process studied, in order for the electro-recovery studied in the subsequent section to be feasible.

During the tests conducted, the oxygen fugacity was not enforced but set by ambient conditions in the crucibles open to atmospheric air by design. With the exception of $Cu_2O$, all of the used metal oxides were stable at the experimental temperature in atmospheric conditions. When heated up in air $Cu_2O$ will eventually turn to the most stable copper oxide, CuO. This resulted in an interesting relation, where the metal oxide solubility was greater in case of less stable oxide used as the feed for the dissolution process. For all other metals, the starting oxides and associated metal valences ($Cu^{2+}$, $Mn^{3+}$, $Ni^{2+}$, $Co^{2+/3+}$) remained stable during the complete thermal cycle of the test.

**Solubility in boron oxide**

The dissolved metal quantity resulting in the metal oxide dissolution in $B_2O_3$ at 900 $^{O}C$ is presented in Table 10. It can be seen that the solubility in pure $B_2O_3$ is negligible. X-EDS line-scan (Figure 6.2-1) shows the metal content drop instantly after crossing the interface between the metal oxide pellet and $B_2O_3$ glass. Additionally, colouration of the sample varied depending on the metal dissolved in the glass, as listed in the Table 6.2-1.

*Table 6.2-1 Metal oxides solubility in $B_2O_3$ at 900 $^{O}C$ as measured by X-EDS*

| Metal Oxide Formula | Metal Species Concentration (wt%) | Colouration |
|---|---|---|
| $Co_3O_4$ | 0.2 | Pink |
| $Cu_2O$ | 0.6 | Turquoise |
| $CuO$ | 0.3 | Turquoise |
| $Mn_2O_3$ | 0.4 | Colourless |
| $NiO$ | 0.5 | Green |

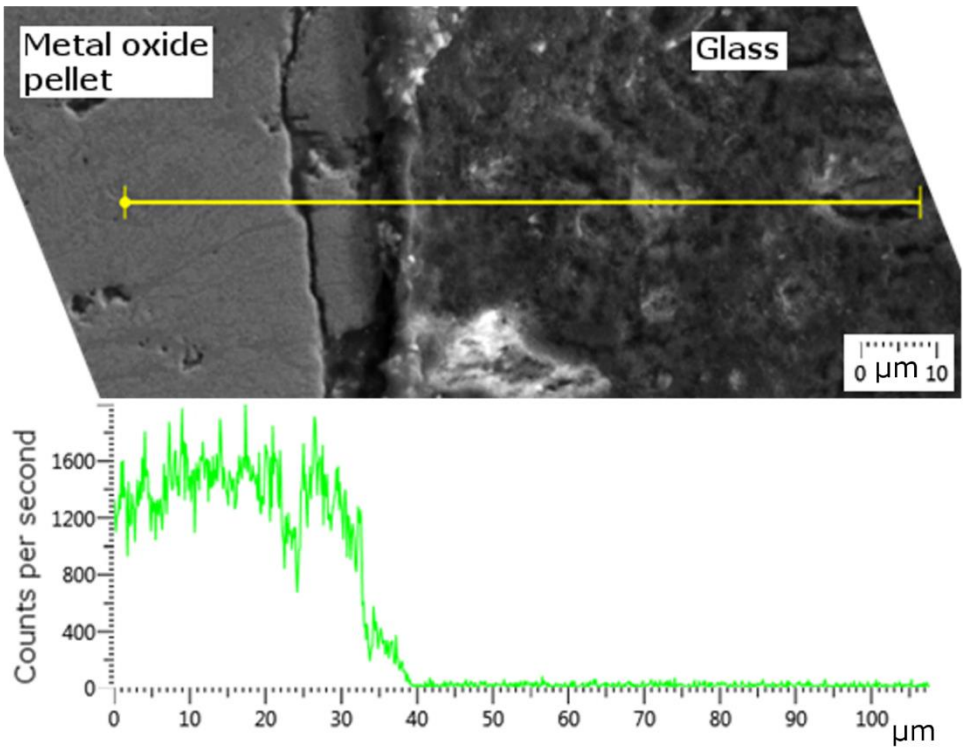


*Figure 6.2-1 Secondary electron image (SE2) and X-EDS line-scan line scan showing nickel element distribution. Metal pellet is on the left side showing high nickel concentration, while the adjacent glass sample shows negligible nickel content suggesting a lack of dissolution.*

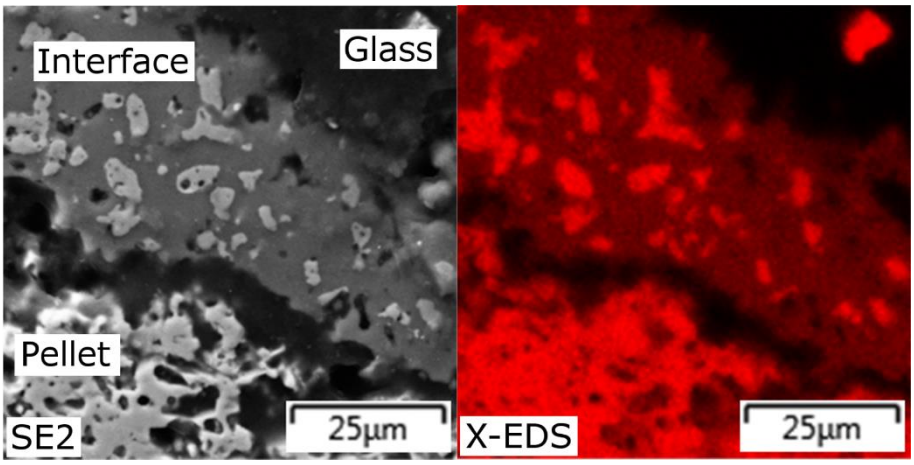


*Figure 6.2-2 SEM Secondary electron (SE2) image and the corresponding X-EDS map of manganese distribution on the salt-pellet interface. Possible interface can be seen between the glass and pellet regions, with broken-off pieces of metal oxide pellet mixed in it.*

Negligible diffusion of the metal into the borate phase, as indicated in Figure 6.2-1, could be ascribed to the *solubility gap* often present in similar systems, such as $B_2O_3$-$FeO_x$ [175]. Solubility gap is a phenomenon possible when the mixture composition is located in the two-phase region of the phase diagram, resulting in high- and low-concentration zones forming an immiscible interface, as there is no stable homogenous mixture at the given composition [176]. If such is the case, there would be a layer of high concentration mixture surrounding the metal oxide pellet, while the bulk concentration would remain low despite long equilibration times in the experiments. Potentially, in such case forced convection could increase the metal concentration in the bulk material. However, no high-concentration layer usually present in such case was found around the pellets nor in any other regions, except for $Mn_2O_3$. Figure 6.2-2 suggests existence of a high- metal concentration film on the interface between the borate phase and metal oxide pellet, which could be an effect of the aforementioned solubility gap. As the samples were held at constant temperature for significant number of hours, the equilibration time eliminates the possibility of kinetics limiting the achieved metal dissolution. This means that the dissolved metal amount is limited thermodynamically.

**Solubility in sodium borate**

Sodium oxide presence in the sample ($Na_2O$-$2B_2O_3$) was found to have a significant impact on the metal oxides solubility, as shown in Figure 6.2-3 representing comparison of $B_2O_3$ and $Na_2O$-$B_2O_3$ solvent cases. There is a substantial increase in the solubility, from eight times to more than seventy times for NiO and $Co_3O_4$ respectively. The reason behind this observation

lies within the previously described *borate anomaly* in section 2.3.2. Alkali oxide additive changes the structure of the highly-polymeric borate glass, which subsequently changes it properties, additionally creating more negative-exchange sites (section 2.3.2.1). As a result, much stronger metal ion affinity is featured. This allows for much higher metal ions concentration achieved in the melt, which is highly beneficial for the process developed in this work. The uniformity of the metal distribution in the glass phase is shown in Figure 6.2-4, confirming that the system has reached thermodynamic equilibrium and uniform metal distribution throughout the oxide phase during the testing.

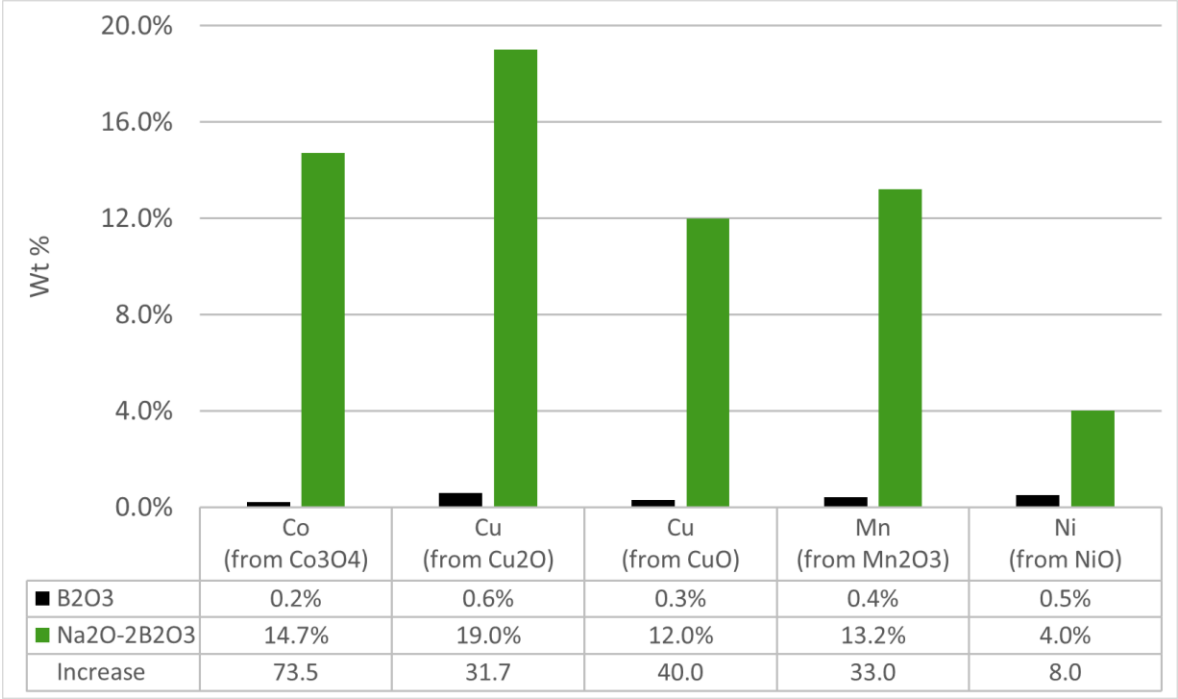


| | Co (from Co3O4) | Cu (from Cu2O) | Cu (from CuO) | Mn (from Mn2O3) | Ni (from NiO) |
|---|---|---|---|---|---|
| B2O3 | 0.2% | 0.6% | 0.3% | 0.4% | 0.5% |
| Na2O-2B2O3 | 14.7% | 19.0% | 12.0% | 13.2% | 4.0% |
| Increase | 73.5 | 31.7 | 40.0 | 33.0 | 8.0 |

*Figure 6.2-3 Metal oxide solubilities in pure $B_2O_3$ and sodium oxide doped $Na_2O$-$B_2O_3$ at 900 °C. The results were obtained using X-EDS after equilibrating the system for 145 hours at the experimental temperature and subsequent liquid nitrogen quenching. The numbers shown represent relevant metal species/element amount in each sample. Standard deviation of these measurements is within $\sigma$=0.1.*

Interestingly, it was observed that feeding less stable copper oxide $Cu_2O$ resulted in higher metal concentration in the glass after dissolution. CuO is the thermodynamically stable oxide at the experimental conditions, to which $Cu_2O$ should oxidise at the elevated temperature, however the process has been reported to be slow [161]. This allows for the presence of the $Cu_2O$ pellet in the melt for the beginning of the dissolution process, remaining in this form for a period of time. Considering $Cu^+$ cation dissolved in the slag, it is required for the $Cu^+$ ion to be transported in the melt for oxidation to be completed, before the final equilibrium is

reached. If this process is slow and the $Cu^{+}$ ion presents higher solubility than $Cu^{2+}$, this could explain the current results of higher solubility after feeding $Cu_2O$ into the melt as the copper metal oxide.

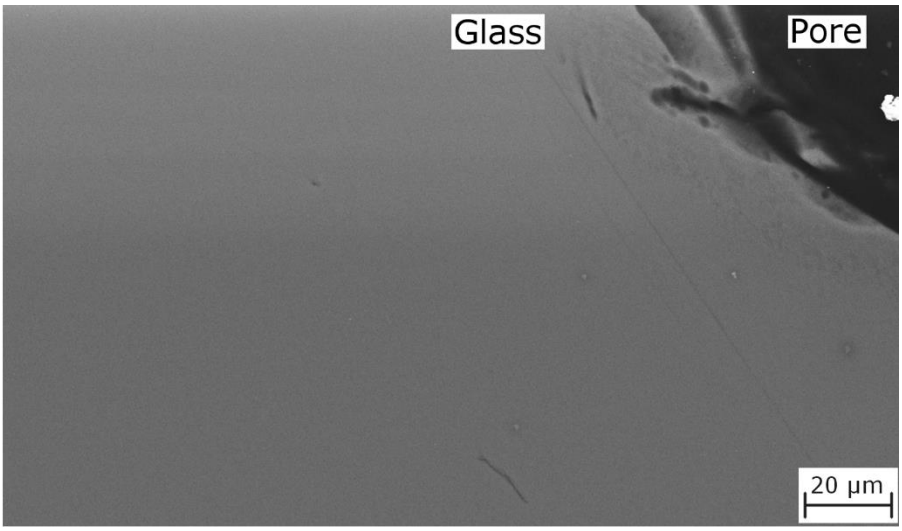


*Figure 6.2-4 Backscatter electron image of the $Na_2O$-$B_2O_3$ sample with $Cu_2O$ dissolved, after equilibration and quenching. Uniformity of the grey area confirms the even metal distribution as no higher-concentration areas can be seen.*

To understand the greater solubility of the $Cu_2O$ over CuO, we need to assume a solution model. Temkin [72,73] described a model in which molten salts are assumed to be completely ionised, which rules out the Ionic Strength influence (difference in the overall ions concentration in the solution), which would directly influence the different salts solubility, as it does for water-based solutions. As we stay below the Upper Critical Solution Temperature (temperature above which the components of a mixture are miscible in all proportions) in our experiments [72], the limiting factor for the solubility is the positive enthalpy of mixing, which stays positive up to the UCS Temperature. The existing Temkin and Forland models could be theoretically used for calculation of the thermodynamics of mixing, potentially explaining the difference between the two copper oxides; however, these two models assume the chemical species present in the melt to behave as pure components, ignoring their oxidation states [72]. Additionally, ideal models assume random initial distribution of atoms and the enthalpy of mixing equal zero, rendering the calculations based on the aforementioned models highly inaccurate in our case. Quasi-chemical solution models created by Guggenheim address this issue [56,177,178], as they consider both non-zero enthalpy of mixing and non-random distribution of atoms. Such model could potentially be built for the system being evaluated,

and help describe the thermodynamic behaviour of the two copper oxides, explaining the difference.

However, it remains speculative and further investigation would be required in order to properly explain the dissolution solubility difference between $Cu_2O$ and CuO. Experimental identification of the oxidation state of the Cu dissolved in the sample would be required, which is non-trivial.

**Other evaluated influences on solubility**

It was evaluated whether a higher temperature would significantly improve the metal oxide solubility with the use of $Mn_2O_3$ in the $B_2O_3$ melt at 1050 $^{O}$C. It was observed that the temperature increase of 150 $^{O}$C caused a negligible change in the solubility, suggesting that the slope of the phase diagram is very steep in this region. Further examination is suggested to gain a better understanding of the thermodynamics of metal oxides dissolution in borate salts, and fill the experimental data gaps in the related phase diagrams.

$K_2O$ was another alkali metal oxide experimented with as a dopant for the molten salt solvent. $K_2O$-$2B_2O_3$ was evaluated using $Mn_2O_3$ as the metal oxide feed to compare the solubility, following the same experimental procedures. It was found that $K_2O$ shows little impact on the considered metal oxides dissolution, resulting in a negligible change in the solubility values. The exact reason for the difference between the $Na_2O$ and $K_2O$ influence on the $B_2O_3$ as the solvent remains unknown; however it can be related to the way each alkali metal oxide modifies the borate melt's polymeric network [59]. Further testing under different conditions and with other metal oxides would have to be done in order to develop greater understanding and a more complete picture of the phase formation and metal (oxides) solubility in molten borate salts.

**Metals distribution in the borate-chloride system**

As described in section 2.3.4, while the borate and chloride phases are immiscible at the considered composition [59], dissolved metal ions are distributed between the two phases depending on the ion and the salt composition. The resulting system has a clearly defined interface with two differently coloured phases, as shown in Figure 6.2-5. The metal concentrations were evaluated as described in section 5.2.1, and the values achieved in the chloride layer were as follows: Cu 3 wt%, Co 0.7 wt%, Mn 0.4 wt%, and Ni 0.1 wt%. The distribution between the two phases has been evaluated and is presented in Figure 6.2-6.

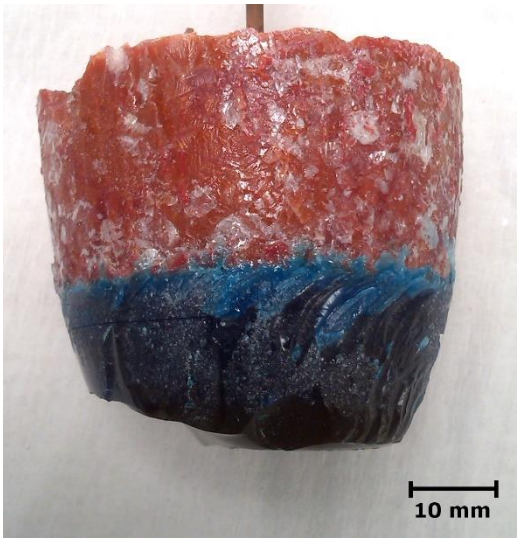


*Figure 6.2-5 Sodium borate – sodium chloride sample with dissolved copper oxide. The borate (lower) and chloride (upper) phases are clearly defined, supporting the immiscibility theory. Different colours also suggest different metal compounds present in each phase.*

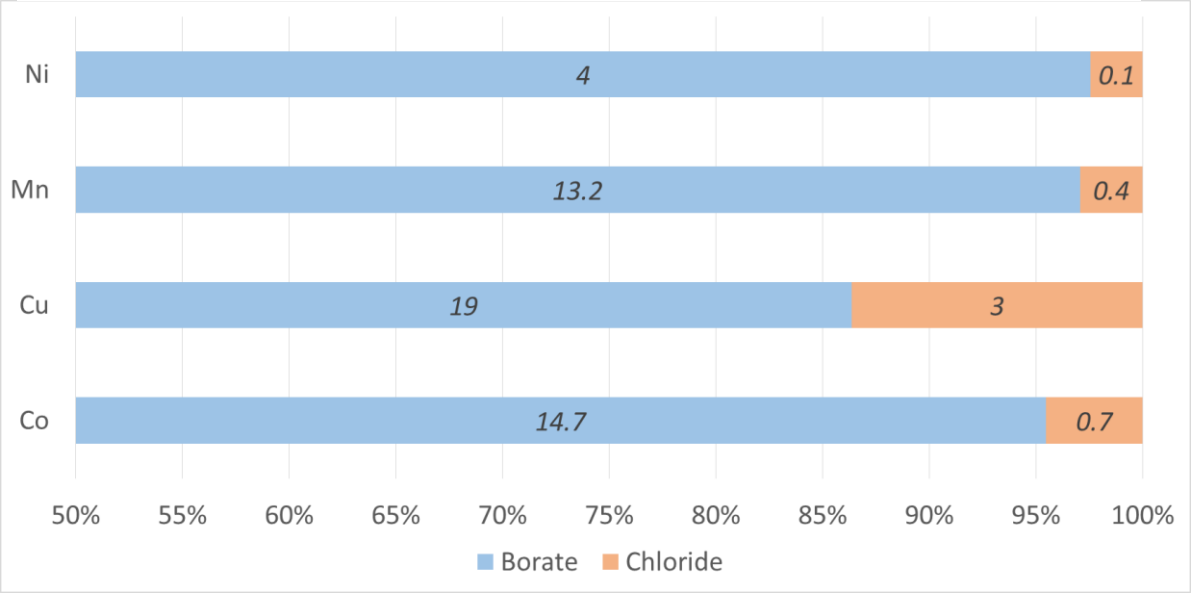


*Figure 6.2-6 Distribution of the metal species in the two-phase system ($Na_2O$-$2B_2O_3$ + NaCl) after equilibration at the elevated temperature of 900 $^{O}$C. Numbers on the bars represent the weight percent of the metal in the given phase. The x-axis shows the contribution each phase had in relation to the overall amount of the metal dissolved.*

As was previously described in the *Literature review*, the amount of metal ions present in the halide layer can be significantly lower than in the oxide layer, which is further enhanced by the high number of the negative exchange sites present in the sodium borate phase. This is due to the specific composition of the mix containing alkali metal oxide $Na_2O$, which modifies the

structure of the highly polymeric molten borate, increasing its affinity towards metal ions. This causes the partition coefficient bias towards the borate layer, which results in a limited metal concentration in the chloride phase. However, as the interface exchange mechanism is based on the chemical reaction (2.3-9) described in section 2.3.4. at the elevated temperature of the process it is not expected to be the limiting step of the process, which is usually the diffusion in case of molten salt processes [51].

Copper sample shows an exceptionally high concentration in the halide layer, when compared to the other metals. This behaviour can be ascribed to the copper oxychlorides formation, which is a phenomenon previously reported for molten salts containing copper chloride [51]. Oxychlorides were detected in the post-processed samples using the X-ray Diffraction analysis, and identified as $Cu_4O_4Cl_4$. The specific oxychloride formed can originate from a different precursor, precisely copper oxide instead of copper chloride, the particular composition of the melt and the chemical reaction occurring at the liquid-liquid molten salts interface. However, the mechanism of the oxychlorides formation from the metal oxide is not explainable by the assumed liquid-liquid interface transfer reaction at the time of writing this work.

As the borate phase is expected to supply the metal ions for the evaluated metal recovery process, its high metal solubility is essential for the system considered. In case of a diffusion limited process, an assumption which is evaluated later in this work, the relatively low amount metal ions in the chloride layer will be constantly re-supplied by the lower borate phase through the liquid-liquid interface by a chemical reaction, allowing for the continuity of the process considered.

The hypothesis of significant metal oxide solubility in borate salts stated at the beginning of this section was confirmed; however, it does not apply to all of the salt combinations. It was concluded that the sodium borate system offers the highest limiting solubility. Metals distribution between the two molten phases is unfavourable towards the chloride layer, due to the high metal affinity of the modified structure of the borate resulting in a high number of negative exchange sites. However, the borate phase working as a buffer feeding the metal ions into the chloride phase should allow for the metal extraction process to occur, as is evaluated in the following section.

## 6.3. Electrolytic metal recovery from the two-phase molten salt cell

For the studied method to work, the system needs to provide a sufficient amount of metal ions through the liquid-liquid interface for the electrolysis, while keeping the phases separate to avoid boron contamination and de-stabilisation of the phases structure. The following subsection evaluates the feasibility and thermodynamics of the metal electrodeposition from the two-phase molten salts system and the purity of the metals recovered.

Electrolysis occurring in the top chloride layer of the electrochemical cell can be described by the following reactions (6.3-1) to (6.3-3):

$$Cathode: \ Me_{(l)}^{x+} + xe^- = Me_{(s)} \tag{6.3-1}$$

$$Anode: \ xCl_{(l)}^- = \frac{x}{2} Cl_{2(g)} \uparrow + xe^- \tag{6.3-2}$$

$$\text{Cell:} \quad MeCl_x = Me_{(s)} + \frac{x}{2} Cl_{2(g)} \uparrow \tag{6.3-3}$$

The reactions above describe the complete process occurring in the single-phase setup. The processes happening in the two-phase cell would also include, in addition to the electrolysis reactions, dissolution of the metal oxides in the borate phase, mass transport to the liquid-liquid interface, transfer across the interface and diffusion in the chloride layer towards the metal electrode. The metal oxides solubility was evaluated by the author previously, as described in section 6.2, and it was concluded that the highest metal solubility was achieved by using $Na_2O$ doped borate salt, resulting in a 6-23% dissolved metal concentration in the sodium borate. This analysis focuses on the electrolytic cell as a whole, and the comparison of the single- and two-phase molten salt systems.

**Electrochemical cell background analysis**

A background scan curve was obtained by scanning the pure two-salt system (NaCl + $Na_2O$-$2B_2O_3$), with the following electrode setup: WE: tungsten, CE: graphite, QRE: tungsten, at 900 $^{O}$C. As is shown in the CV scan Figure 6.3-3, there is a flat plateaou corresponding to the stability region of the salt system. The stability window spans between ~ 1.5 V to 0.5 V, which allows for the recovery of the metal evaluated, as is described in a later part of this section. As the background is free of peaks there is no interference with the electrochemical measurements. Background current of ~5 mA can be observed observed as presented on the

enhanced insert. Additional pre-electrolysis at -1 V for 2 hours had negligible influence, therefore validating the assumed method of purification, as described in section 5.2.1.

Another important feature of the background curve is the onset of the anodic reaction - chlorine evolution. Since a quasi-reference electrode is used, repeatable reference reaction point could offer an additional validation mechanism/reference point. However, as the gas evolution leads to dynamic bubbles formation, the onset of the reaction varies slightly depending on what is agreed as the inflection point. The presented graph is uniquely free of perturbances in the gas evolution region, and still the onset values can be assumed as 0.2, 0.5 or 0.75 V. Additionally, overly-positive potentials could lead to the cathode dissolution, metal plating on the counter-electrode and gas bubbles stuck to the surface of the working electrode, changing its characteristic. Finally, each metal features different overpotential for gas evolution reaction, resulting in the measurements varying with the reduced metal present on the working electrode. Therefore, such method might be useful, although it is not free of challenges and potential variations.

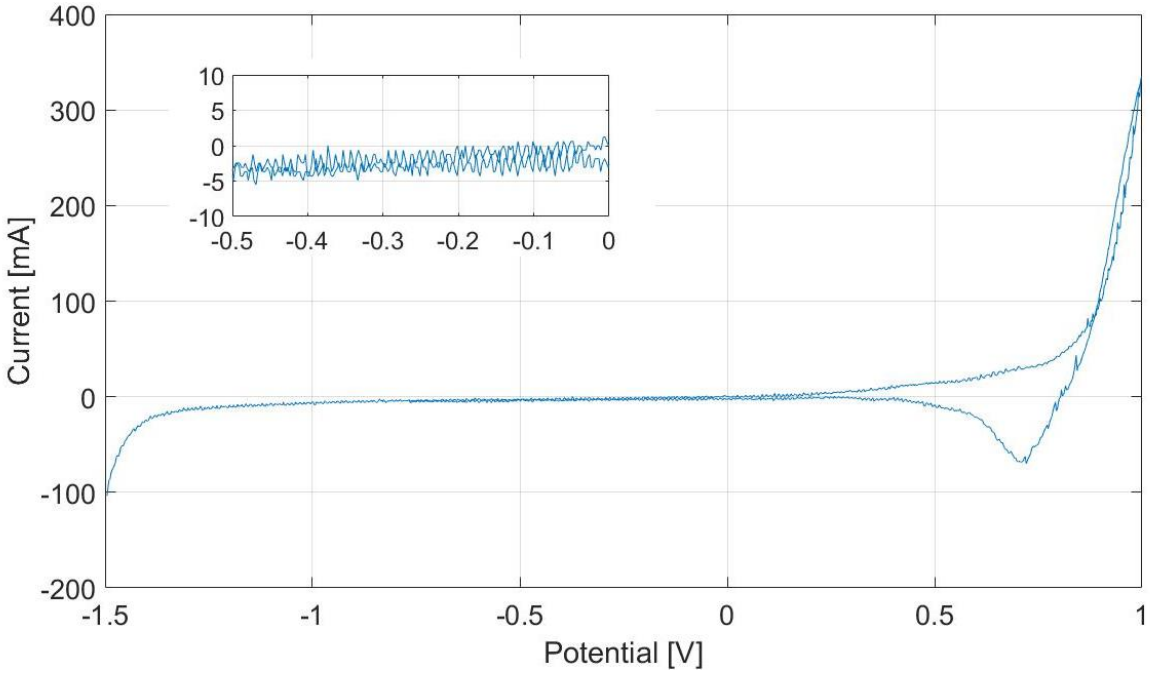


*Figure 6.3-1 Electrochemical stability window of the studied molten salt cell (NaCl + $Na_2O$-$2B_2O_3$) at 900 $^{O}$C. Sweep rate 100 mV/s. WE: tungsten, CE: graphite, QRE: tungsten.*

### Electrochemical analysis

The cyclic voltammetry profiles are presented in Figure 6.3-4 and 6.3-5 for the single- and two-phase cells respectively. It needs to be noted that due to the chlorine evolution reaction (6.3-2) readily happening at the positive potentials, the electric current values observed can be altered by the process when scanning in that range. The formal redox reaction potential values are listed in Table 6.3-1 and 6.3-2. The experimentally obtained potential values were compared against the thermodynamic values of the metal chloride electrolysis, resulting in a correlation described further in this section. This allowed for deeper analysis of the system evaluated.

All of the considered metals were plated and their cyclic voltammetry profiles plotted, obtaining data on the redox reactions happening at the working electrode. The metal deposits retrieved are shown in Figure 6.3-1, the corresponding chronoamperometric profiles are shown in Figure 6.3-2. The metal electroreduction peaks are within the electrochemical stability window of the used salt [-1.5 V to +0.5 V vs tungsten Ref], as shown in Figure 6.3-3. This allows for the considered metals recovery without breaking the bulk salt. Re-oxidation peaks are also visible on the CV scans, confirming the reversibility of the electroplating process in the evaluated system, and enabling the formal potentials analysis. The flat plateau preceding the peaks is attributed to the kinetic barrier of the reaction, while the peak tailing represents the diffusion controlled area of the CV scan [114]. Additionally, care should be taken to analyse the early/first scan of the Cyclic Voltammetry measurement, as potentially highly-dendritic growth can compromise subsequent readings by changing the electrode geometry and process kinetics, shifting the apparent reduction peaks. Dendritic growth is evaluated in the next section of this thesis.

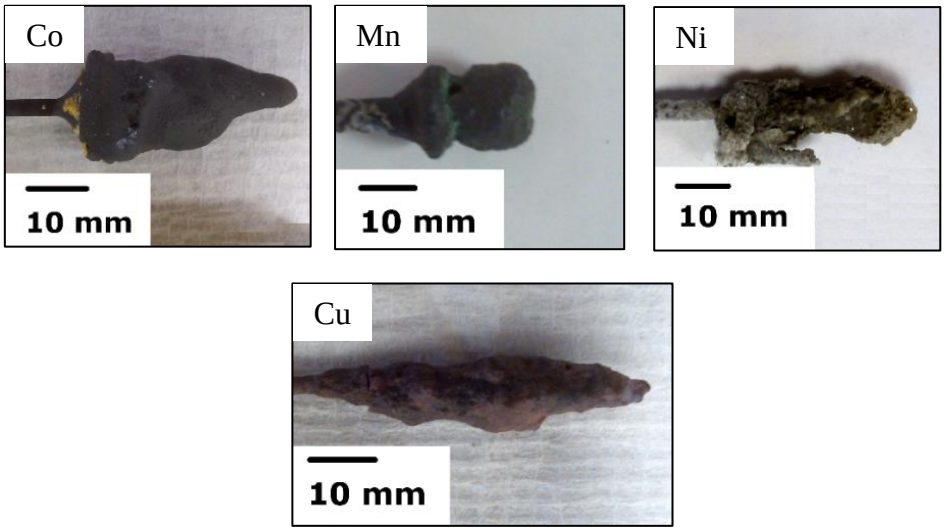


*Figure 6.3-2 Plated metal deposits of cobalt, manganese, nickel and copper. Plating potentials: Co: -500 mV, Cu: -450 mV, Mn: -950 mV, Ni: -300 mV at 900 $^{O}$C. WE: tungsten, CE: graphite, QRE: tungsten. Plating time varied depending on the current increase rate. Relevant SEM pictures of the deposits are analysed in a further section of this work.*

The chronoamperometric profiles obtained during long-term constant-potential electrodeposition (Figure 6.3-2) show definite increase in current over time, a phenomenon that will be discussed more closely in the next section. The possible explanations of this behaviour originate from the electrode growth, resulting in an increased electrode surface, more complex geometry, variations in current density and lower kinetic barriers due to the modified electrode geometry. It also underlines that any measurements influenced by the electrode surface should be taken early in the process as to avoid incorrect readings. Due to the electrode surface varying with the level of the rods immersion, current density could not be reliably calculated. Finally, because of the complex and fragile dendritic deposits, the current readings are noisy possibly influenced by the dendrites breaking off dynamically changing the electrode surface.

Analysis of the plated material and its correlation to the charge passed through the electrode would be beneficial. However, due to the form in which the metal is retrieved – heavily dendritic form encapsulated in a solidified salt, conventional methods are challenging. Brunauer–Emmett–Teller (BET) [179] method that estimates the surface of material on a basis of adsorption of gas molecules cannot be used, due to the fragile metallic dendrites being surrounded by the solidified mass. X-ray computed tomography [145] is capable of

differentiating between the salt and the metal offering some analysis capability, although tungsten, used here as the electrode, attenuates the rays to the point of invalidating the measurements. Nevertheless, such analysis has been conducted on copper after long-time plating and successful recovery of a properly preserved piece of the deposit form the electrode. The attempt is described and analysed in section 6.4 of this thesis.

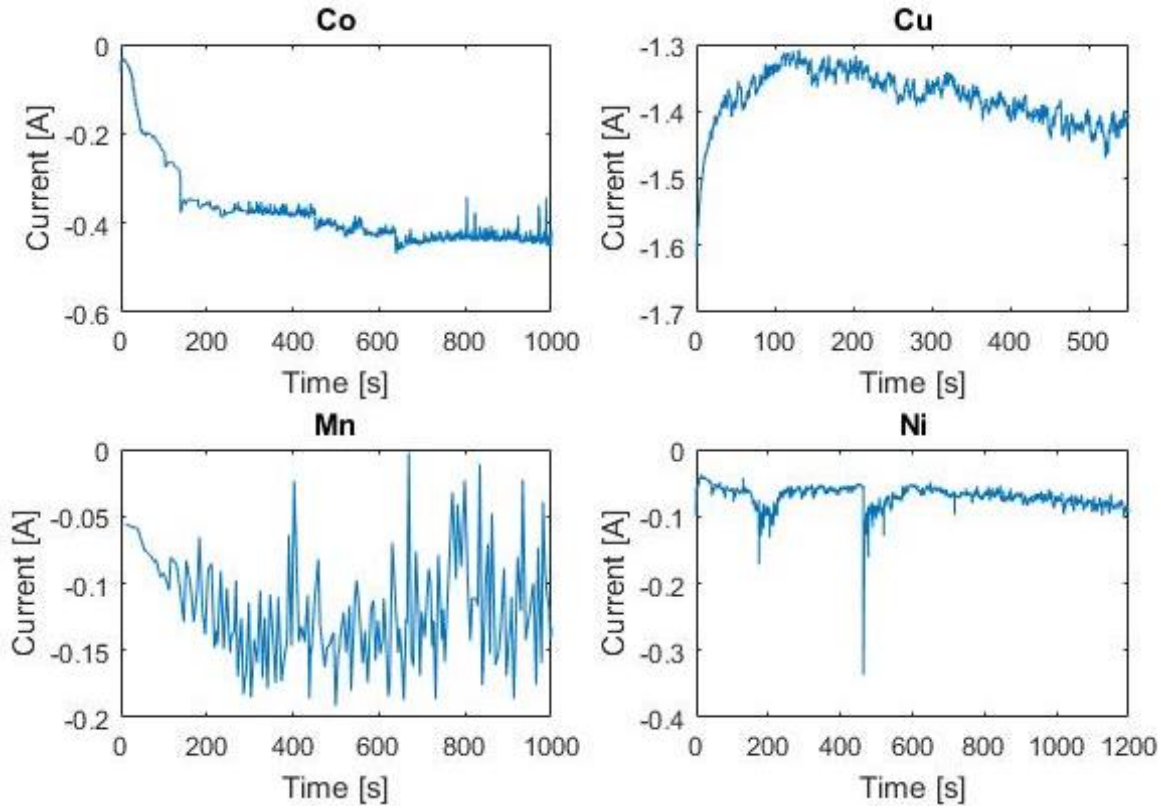


*Figure 6.3-3 Chronoamperometric plots of the selected metals electrodeposition. Plating potentials: Co: -500 mV, Cu: -450 mV, Mn: -950 mV, Ni: -300 mV at 900 $^{O}$C. WE: tungsten, CE: graphite, QRE: tungsten. As the electrode surface depends on the depth of the electrode submersion and the electrode surface changes with time, absolute current is presented rather than current density.*

**Single-phase cell analysis**

Table 6.3-1 contains the experimental data for the single-phase cell system, shown against the calculated thermodynamic values of the metal chloride electrolysis, described by the reaction 6.3-4 at the test temperature of 900 $^{O}$C. The CV plots representing the collected data are shown in Figure 6.3-4. The thermodynamic electrolysis potentials were calculated using the Gibbs free energy and cell potential relation equations (6.3-4) and (6.3-5):

$$\Delta G = -RTlnK = -nFE \quad (6.3\text{-}4)$$

$$E = \frac{-\Delta G}{nF} \quad (6.3\text{-}5)$$

where: $\Delta G$ is the Gibbs free energy change, $E$ is the calculated potential, $F$ is the Faraday constant, and $n$ is the number of electrons taking part in the redox reaction. The remaining symbols have their usual thermodynamic meaning.

The reactants concentration was set at 1 wt% across all tests, resulting in the following: 0.121 M Co, 0.116 M Cu, 0.1249 M Mn, 0.1213 M Ni (accounted for using the Nernst equation). The calculated metal chloride electrolysis potential values are relevant with reference to the chlorine evolution reaction occurring at the positive electrode, as described by the reactions (6.3-1) to (6.3-3).

*Table 6.3-1 Experimental and calculated thermodynamic electrolysis potential values in sodium chloride melt, in a single-phase cell with the metal chloride feed*

| **NaCl + $Me_xCl_y$** | | | | |
|---|---|---|---|---|
| **Single-phase (NaCl) cell** | **Co** | **Cu** | **Mn** | **Ni** |
| Formal redox potential [V] (vs. W ref) | 0.0501 | -0.182 | -0.651 | 0.094 |
| Thermodynamic potential [V] (vs. $Cl_2$ evolution) | -0.949 | -0.418<br>-1.075 ($Cu^+$) | -1.860 | -0.737 |

A similar tendency in the metals electroplating potentials was observed by Gaur et al. [108], meaning the reduction potentials of the evaluated metals grew in the same order. However, the molten chlorides system evaluated in his work was considerably different. As described in section 2.3.3.1, a number of overpotentials can be expected in the evaluated system. This includes the *activation overpotential* ($E_{act}$), related to the activation energy necessary for the electron transfer between the electrode and the electrolyte, *resistance overpotential* ($E_{\Omega}$) which includes the electrode capacitance and the junction overpotential, specific to each cell design, and the *concentration overpotential* ($E_{conc}$) which is related to the diffusion and the reactant depletion at the electrode surface. For this reason, the formal redox reaction potentials were analysed.

Interestingly, the recorded copper reduction potential is more negative than that of cobalt, contradictory to the thermodynamic values of $CuCl_2$ and $CoCl_2$ electrolysis (shown in Table

6.3-1). This is visible in Table 6.3-1 and Figure 6.3-3. The observed phenomena could be explained by the presence of high overpotential of copper electrodeposition on the tungsten electrode, caused by the specific electrode material and its structure [51,115,125]. Alternatively, copper(II) chloride can react according to the following reaction (6.3-6) as a mild oxidant, especially at the elevated temperature under the reducing argon atmosphere [162].

$$CuCl_2 = CuCl + 0.5Cl_2 \tag{6.3-6}$$

The resulting $Cu^{1+}$ ions would explain the higher electroreduction potential observed. The thermodynamic value of CuCl electrolysis equals -1.075 V for the experimental parameters used. If we assume the CuCl electrolysis, the thermodynamic values adhere to the trend observed in the experimental results. This assumption was evaluated experimentally by measuring the copper(I) chloride CV profile, which closely resembled that of the previous tests. Supported by the thermodynamic and experimental evaluation, it was determined that the copper(I) chloride electrolysis was observed.

The use of the formal potentials of the redox reactions for the analysis limits the influence of the aforementioned overpotentials; therefore, the thermodynamic-experimental potential difference can be ascribed to the W reference electrode potential and the anodic reaction (6.3-2). Theoretically, as the reference electrode represents a stable potential point, chlorine evolution should always be at the same potential difference vs reference, resulting in the metal reduction potential being the only variable in the system. However, as discussed in section 2.3.7, that might not be the case, as molten salts are not a completely neutral solvent. As the solvation layers formed in the electrolyte change with the composition of the melt, they are reported to have an influence on the redox reaction potentials of both cathodic and anodic processes [149,150]. This requires special consideration in order to be able to analyse the system.

As described earlier in this section, observing chlorine evolution onset would offer some solution, although due to its shortcomings it has not been selected as the method of choice. In an attempt to numerically describe the system and include both the anodic and cathodic shifts due to the electrolyte and metal feed influence, the thermodynamic full cell potential has been compared to the experimentally measured metal formal reduction potentials. The relation was found to be linear, and could be described with the following empirical equation (6.3-7). This

allowed for the calibration of the system evaluated using the thermodynamic metal chloride electrolysis potentials and the experimentally measured metal redox reaction (6.3-1).

$$E = E_{measured} \cdot 1.410 - 0.912 \tag{6.3-7}$$

where: $E$ is the thermodynamic electrolysis potential [V] and $E_{measured}$ is the observed formal redox reaction potential [V].

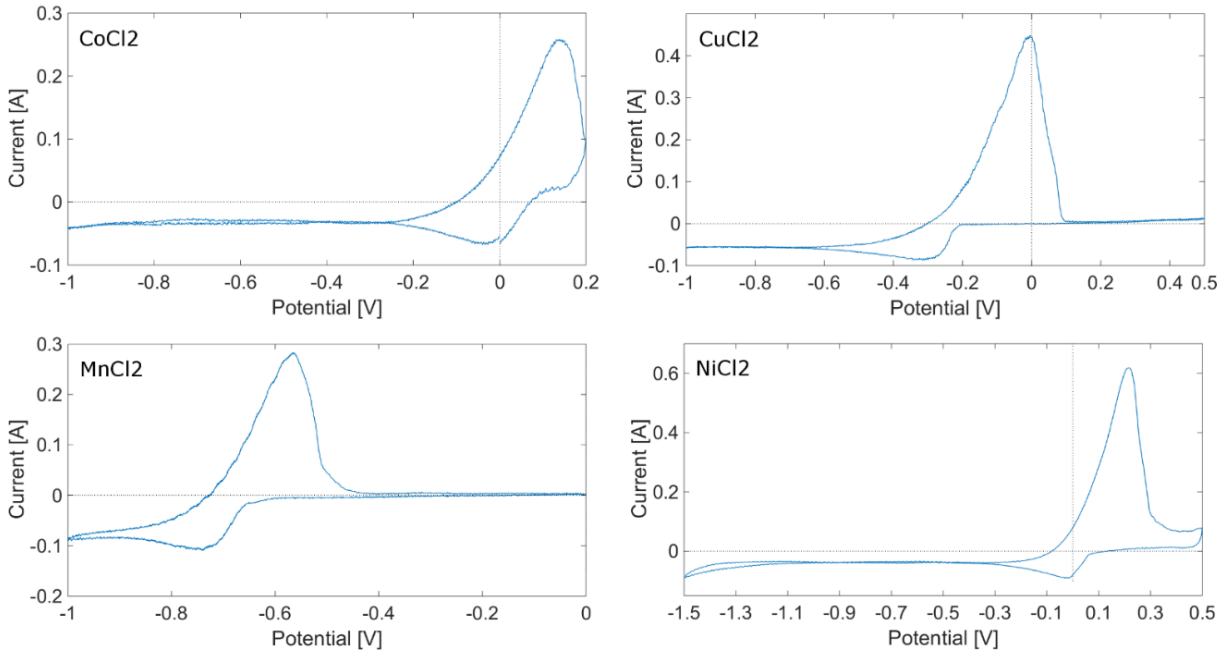


*Figure 6.3-4 Cyclic Voltammetry profiles of the metal chlorides electroreduction from the single-phase (NaCl) cell at 900 $^{O}$C vs tungsten electrode.. Scan rate of 0.1 V/ was used. WE: tungsten, CE: graphite, QRE: tungsten. Axis lines with (0,0) cross-point were added for easier interpretation.*

Useful observations can be made when analysing the plating and stripping peaks, and the respective charge passed through the working electrode. Although the process is practically reversible (as explained in section 2.3.3.3) as the metal plated can be re-oxidised, the metal oxidation peaks, also called stripping peaks [114], are much higher than the corresponding reduction/plating peaks. Identical behaviour has been observed by other researchers as well [104,125]. This is due to the reagent being readily available at the surface of the electrode, as previously discussed, which removes the mass transfer limitation from the process. By integrating the surface of the peaks, the amount of charge passed during cathodic and anodic processes can be calculated. The results are shown in table 6.3-2.

*Table 6.3-2 Plating and stripping charges comparison. Each metal was plated separately from its respective chloride at 900 $^{O}C$ using cyclic voltammetry sweep at 100 mV $s^{-1}$. WE: tungsten, CE: graphite, QRE: tungsten. Corresponding CV profiles are shown in Figure 6.2-4.*

| | **Co** | **Cu** | **Mn** | **Ni** |
|---|---|---|---|---|
| Plating [mC] | 934.2 | 958.4 | 598.7 | 622.3 |
| Stripping [mC] | 423.8 | 766.7 | 350.5 | 400.9 |

The results show that the amount of charge passed during plating is usually twice as much, which is reasonable considering that metal has to be plated first in order to be available for oxidation. The disparity between the oxidation/reduction charges can originate from the pace of the process – if left for longer, all the metal would eventually oxidise increasing the amount of the passed stripping charge. However, due to the side-processes such as back-dissolution lowering the reducing current efficiency, shuttling between the electrodes possible in case of multi-valent ions and the background current identified earlier in this section, the stripping charge would always be lower than the required plating charge. This also negatively influences the apparent reversibility of the process by increasing the disparity between the anodic and cathodic charge [114].

A slower scan rate of 10 mV was also evaluated and found not fitting, as was suggested in section 5.3. As can be seen in figure 6.3-5, the reduction peak is more stretched, less pronounced, as the reaction happens less suddenly, the metal ions activity is lower at the onset of the reaction, although the reagent is more slowly consumed creating the diffusion layer over a longer time. This results in longer tailing, as well as more significant modification of the electrode surface during a single scan. This in turn results in noisier readings making the analysis more challenging. This behaviour is expected to be opposite in case of faster sweep rates, resulting in higher peak current and overall sharper peak shapes.

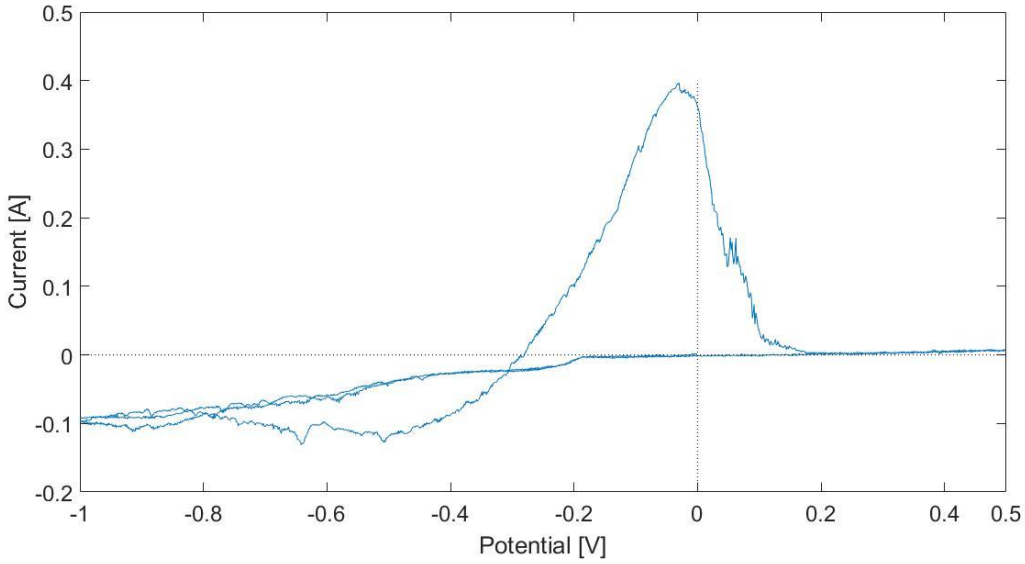


*Figure 6.3-5 Cu electrodeposition Cyclic Voltammetry scan at a scan rate of 10 mV $s^{-1}$. WE: tungsten, CE: graphite, QRE: tungsten. Mixture of 1 wt% $CuCl_2$ in NaCl was used at the temperature of 900 $^{O}C$.*

**Two-phase cell analysis:**

The two-phase cell setup ($Na_2O$-$2B_2O_3$ + NaCl) was analysed under the same parameters. Metals were added in the form of oxides ($Co_3O_4$, CuO, $Mn_2O_3$ and NiO) in the borate phase at the bottom of the crucible, as shown in the Figure 4.3-1. The proposed exchange mechanism describing the metal ions transfer from borate to the chloride phase through the liquid-liquid interface has been analysed in section 2.3.4, and was represented by the reaction (2.3-6) in the same section.

The phases were clearly divided by the liquid-liquid interface, as the mix composition was within the immiscibility area of the phase diagram, and could be easily separated after the testing. The reported mutual solubility of the evaluated phases is very low [59,139], and was confirmed to be negligible using the Inductively Coupled Plasma – Optical Emission Spectrometry (ICP-OES). A piece of metal deposit was recovered from the electrode with the solidified sodium chloride droplet trapped within the dendritic structure, and analysed with the ICP-OES for the boron presence. The amount found was approximately 40 ppm, which would be of little effect on the process evaluated, confirming the immiscibility of the molten phases.

The achieved metal concentration values in the chloride phase were analysed using the X-EDS apparatus as described in the previous section. The values measured were as follows: Cu 3 wt% (σ-0.2), Co 0.7 wt% (σ-0.1), Mn 0.4 wt% (σ-0.1) and Ni 0.1 wt% (σ-0.1). The copper

concentration was significantly higher, which in conjunction with the electron component superimposition effect (reported as caused by the copper chloride salts presence [111]) resulted in an ion-electron conductivity mechanism, changing the characteristics of the mix. To avoid the soft-shortening phenomenon and to obtain clear reduction characteristics, the copper concentration was limited to 0.5 wt% in the chloride layer.

Both single- and two-phase cell cases were evaluated in an identical electrolysis cell setup to remove the possibility of influence from different cell setup. To analyse the process differences, the metals evaluated are analysed case by case. Table 6.3-3 contains the experimental formal redox reaction potentials, adjusted using equation (6.3-8) to represent the metal chloride decomposition values and enable comparison with the Table 6.3-1 values of the single-phase cell setup.

*Table 6.3-3 Two-phase cell setup electrolysis experimental potential values.*
*The setup consisted of a two-phase $Na_2O$-$2B_2O_3$ + NaCl mix at 900 $^{O}C$ with the metal oxides as the feed, WE: tungsten, CE: graphite, QRE: tungsten. The revised electrolysis potentials were calculated using equation (6.3-7) to represent metal chloride electrolysis values (therefore vs $Cl_2$ evolution).*

| **NaCl + $Na_2O$-$2B_2O_3$ + $Me_xO_y$** | | | | |
|---|---|---|---|---|
| **Two-phase cell** | **Co** | **Cu** | **Mn** | **Ni** |
| Formal redox potential [V] (vs. W ref) | 0.127<br>-0.663 | -0.273<br>-1.037 | -0.454 | -0.583 |
| Revised formal potential [V] (vs. $Cl_2$ evolution) | -0.733<br>-1.848 | -1.297<br>-2.375 | -1.552 | -1.734 |
| Two- vs single-phase cell difference [V] | 0.216<br>-0.899 | -0.222<br>-1.300 | 0.308 | -0.997 |

The difference between the single- and two-phase cell formal redox reaction potentials can be ascribed to the lower metal cation concentration influencing the thermodynamic values, but also different cation availability and diffusion from the borate phase, and through the liquid-liquid interface. In some cases, there could be also chemistry change observed, as will be discussed separately in each case. The influences can be grouped as follows:

- Metal ion availability difference
- Mass transfer in the borate phase and through the liquid-liquid interface
- Different metal ion state in the chloride phase

As was already mentioned, each metal will be analysed separately. Nickel presents the simplest case, as it is stable at +2 oxidation state as a chloride and oxide at the experimental temperature, and the obtained electroreduction profiles are similar. Additionally, as discussed in section 2.3.5, Littlewood diagram for nickel suggests a one-step reaction from $Ni^{2+}$ cation to Ni metal, which is in agreement with the observations for both single- and two-phase cells. Nonetheless, the potential shift observed is significant. However, it needs to be noted that the nickel concentration of around 0.1% implies a relatively large margin of error, and as the nickel oxide shows a very limited solubility in sodium borate, as evaluated earlier in the experimental section, the low ion concentration can be assumed to have a significant impact on the electrochemical potential. Additionally, as the reagent can be rapidly depleted from the chloride layer due to its low concentration, the reaction might rely heavily on the borate layer providing the metal ion, adding the diffusion through borate phase and liquid-liquid interface transfer steps to the metal supply for electrolysis. There is no difference in the metal ion state, so the electrochemical reaction should stay identical in both single- and two-phase cell cases. Therefore, the more negative formal redox reaction potential is mostly caused by the significantly lower metal ion availability, diffusion through the borate layer and the liquid-liquid interface transfer.

As the $Mn_2O_3$ is the most stable metal oxide at 900 $^{O}C$, manganese is present as a different ion in the borate melt. Therefore, a less-negative formal redox potential was observed during the electrolysis. As a result, the electroreduction potential shift towards the more positive values was measured despite the lower concentration of the metal in the melt. This enables the possibility of manganese reduction from +3 ion in the chloride layer, when supplied as $Mn_2O_3$ into the borate. The reaction appears to happen as a one-step three-electron process resulting in a single reduction and oxidation peak, limiting the possibility of the efficiency-adverse shuttling between the electrodes. However, as no thermodynamic data was available on the Gibbs free energy of formation of $MnCl_3$ at the time of writing, the thermodynamic values comparison is impossible. Similarly, as there was a different ion present in the single- and two-phase cell cases, the observation of other influences is challenging. Nevertheless, while the concentration is lower than in the single-phase cell, it is still higher than in the Ni case,

which implies that the difference has smaller impact. An analogous electrochemical reaction is expected to occur at the electrode, as the electrolysis profiles for single- and two-phase cells are very much alike. The potential shift places the electroreduction peak closer to the Ni reduction value, making these two metals potentially more difficult to separate if both were present in the melt. However, such issues can be resolved by implementing optimal engineering solutions, e.g. alloying mechanisms or by using high-overpotential electrodes.

Uncommon behaviour can be observed in case of copper electroreduction from the two-phase cell. Two separate peaks appear on the CV profile, one relatively close to the original reduction potential, with the second peak shifted significantly into the more negative potential values. This observation can be ascribed to either a transient presence of the $Cu^{2+}$ ions in the upper melt phase after the transition from the borate layer, or alternatively to the copper oxychlorides formation, as mentioned in the section 2.3.4. The oxychlorides presence changes the voltammetry profile, and two separate electroreduction reactions can be observed. In case of other metals, no oxychlorides were detected, which is in concurrence with their cyclic voltammetry profiles. Alternative explanation of the peak splitting includes a possible two-step reaction in the form of $Cu^{2+} \leftrightarrow Cu^{1+} \leftrightarrow Cu$. This way the more negative potential peak would correspond to the second part of the reduction reaction. Presence of the $Cu^{1+}$ ions, however unstable [162], could also result in shuttling between the electrodes with the copper ion as the charge carrier following the first part of the redox reaction chain $Cu^{2+} \leftrightarrow Cu^{1+}$, which would result in a significantly lower process efficiency.

Cobalt is stable at a different oxidation level in oxide than in chloride at the experimental temperature of 900 $^{O}$C, similarly to manganese. It forms a spinel compound with +2 and +3 oxidation states, $Co_3O_4$, also written as $CoO\text{-}Co_2O_3$ or $Co^{II}Co^{III}{}_2O_4$. The presence of cobalt at two oxidation states in the melt is reflected in the CV profile, which shows two separate peaks. The +3 cobalt ion, present only in the two-phase cell setup, would show a different thermodynamic reduction potential $E^0$; however, due to the lack of thermodynamic data on the $CoCl_3$ compound it is impossible to calculate the considered chloride decomposition potential value. As the +2 cation reduction potential is most likely to be in the more negative range as it is more difficult to reduce than the +3 cation, we can observe a shift towards the more negative values for the $Co^{2+}$ reduction potential when compared to the single-phase cell setup. This can be also partially caused by the lower metal ion concentration in the melt, as the overall measured cobalt concentration in the chloride layer was 0.186 M; however, it has to be divided between the two ions at different oxidation states. This results in 0.062 M of

$Co^{2+}$ and 0.124 M of $Co^{3+}$ present in the sample. Moreover, as both of the oxidation states are stable in the system evaluated [162], shuttling reaction similar to the one suggested in case of copper could occur. The mechanism would be $Cu^{3+} \leftrightarrow Cu^{2+}$ on the cathode and anode respectively, resulting in lower current efficiency and less metal recovered. Such effects could be reduced by introducing a semi-porous membrane between the electrodes to limit direct diffusion between them, however it could also result in the adverse effect of limiting the diffusion of the species towards the cathode, lowering the reduction rate and increasing the cell's internal resistance.

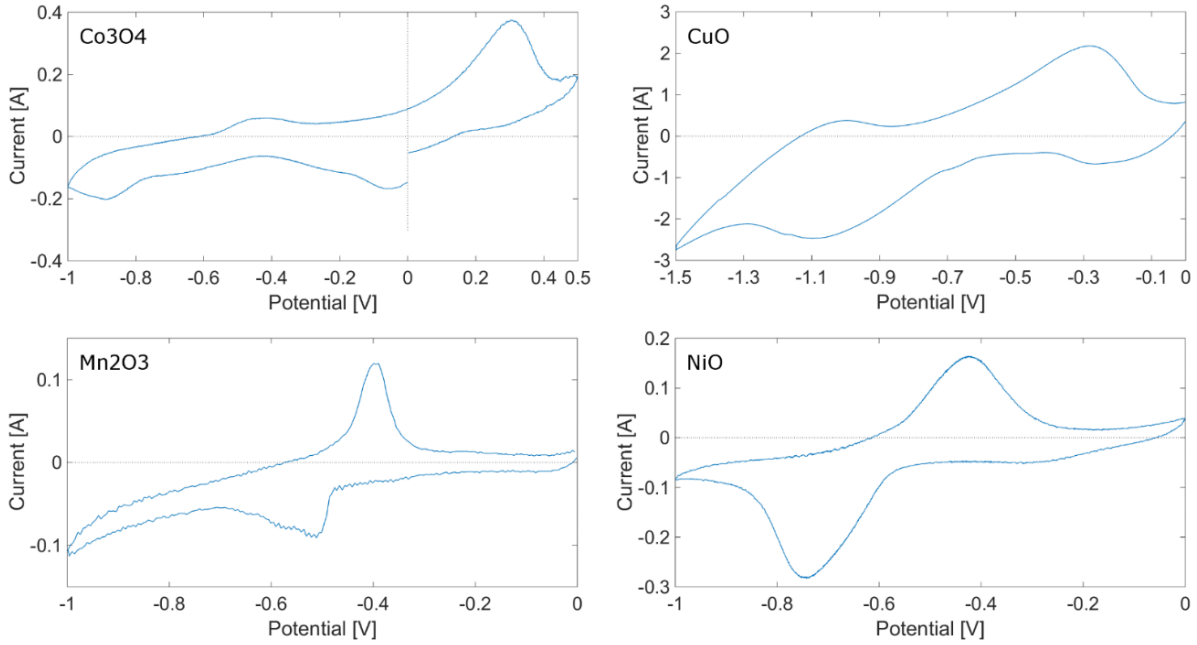


*Figure 6.3-6 Cyclic voltammetry profiles of the electrolysis from the two phase ($Na_2O - 2B_2O_3$ + NaCl) cell setup at 900 $^{O}$C. Scan rate is 0.1 V/s was used. WE: tungsten, CE: graphite, QRE: tungsten. Axis lines with (0,0) cross-point were added for easier interpretation.*

Similarly to the single-phase cell case, the reduction peaks show bigger surface (most visible in case of nickel), than the corresponding re-oxidation areas, while the stripping peaks are more prominent. This is due to the same reason of the reagent being readily available on the surface of the electrode, although the plating current efficiency lowering phenomena, e.g. back-dissolution, result in more charge passed for plating. Additionally, other background and parasitic reactions can effectively reduce the amount of charge used for the metal deposition process, such as shuttling in case of multi-valent ions [114], and the background current previously identified. Finally, metal that is not present at the electrode simply cannot be electrochemically oxidised, therefore such disparity will always be present.

Regarding the observable current, there is a general pattern of the peak current being lower in the two-phase cell, as can be expected due to the significantly lower metal ions concentration in the melt. Additionally, the process can now be dependent on the slower diffusion from the borate layer, which is a highly polymeric and more viscous liquid than the fully ionised halide salt, which would further reduce the maximum current obtained. However, current density could not be calculated due to the varying electrode sizes dependant on the immersion levels in the melt.

To summarise the single- and two-phase electrolytic cell setups, the metal concentration changes in all cases and, apart from nickel, different ions are present, resulting in different $E^0$. Diffusion in the borate layer and the liquid-liquid interface transfer add to the concentration effect. Both cobalt and manganese are present in the single- and two-phase melts at different oxidation states due to their specific metal oxides thermodynamic stability at 900 $^{O}$C. This results in different Gibbs free energies and $E^0$, and creates an interesting opportunity of reducing metal ions from a different oxidation state than usually possible in the chloride melts. Finally, copper presents unique behaviour due to the oxychlorides formation, forming an additional compound when transferred through the liquid-liquid interface to the chloride layer. Alternatively, for the metal species present in the melt at more than one oxidation state, some ion shuttling between the electrodes is possible due to the metals forming multi-valent ions, possible charge carriers between the anode and the cathode. Such possibility is most pronounced by two redox peaks pairs present on the CV curves, as in copper and cobalt case. This effect could effectively lower the process efficiency if present.

As the electrochemical system used featured a tungsten quasi-reference, and due to the solvation layers variations, with the changing electrolyte composition (different metal oxides) both cathodic and anodic potentials shifted. Such a behaviour has been observed by other researchers as well [150]. Therefore, a correlation with calculated full-cell electrolysis potentials has been numerically solved, enabling the comparison of the single- and two-phase cell setups. All of the evaluated metals were deposited successfully by means of electrolysis from the two-phase molten-salt system, proving the concept of this novel alternative metal recovery process for a range of metals in their various oxidation states.

### Recovered material analysis

Metals for analysis were plated potentiostatically at the following plating potentials: Co: -500 mV, Cu: -450 mV, Mn: -950 mV, Ni: -300 mV at 900 $^{O}$C, as described earlier in this section. The purity of the plated metal deposits was approximated using the FEG-SEM X-EDS technique. As the deposited dendrites were of a microscopic size, this method allowed for both structural analysis and chemical identification. It was confirmed using the ICP-OES analysis that the metal sample contained negligible amounts of boron, thus the chemical elements considered were within the detection capabilities of X-EDS at the reported concentrations. The plated metals purity was confirmed to be as follows: 98% for Cu, 99% for Co, 99% for Mn and 99% for Ni.

FEG-SEM pictures confirm the complex deposits structure, as shown in Figure 6.3-7 presenting cross-sections of the recovered metal deposits. Metal fragments seemingly separated from each other suggest a more complex structure in the plane perpendicular to the scanned surface, with the chloride salt trapped in between the metal dendrites. Such a structure is common in case of diffusion-controlled processes, which correlates with other researchers' observations reported in this field [125,126,180]. This phenomenon is analysed more closely in a later part of this work.

As the metal deposits recovery process from the melt is complex and inefficient in the current assembly form, it was impossible to reliably recover all of the metal plated. Dendritic form of the deposits made it difficult to retrieve the material without breaking from the electrode. The dendrites could also break during the process and sink to the bottom of the crucible, where they could also undergo back-dissolution into the borate phase. Therefore, Faradaic efficiency is not reported, until an alternative and more reliable deposited material recovery method is designed and applied. Such an analysis would be beneficial for further development of the process and would enable the process efficiency evaluation and optimisation.

The initial hypothesis on the feasibility of the system for the recovery of metal from the two-phase molten salt system has been confirmed with the successful metal recovery. Purity of the metals was assessed and the boron contamination was concluded negligible, proving the stable separation of the phases during the process and metal ions transfer through the liquid-liquid interface. The structure of the metal deposits is analysed in greater detail in the following section, which focuses on the chronoamperometric profile of the electrodeposition process.

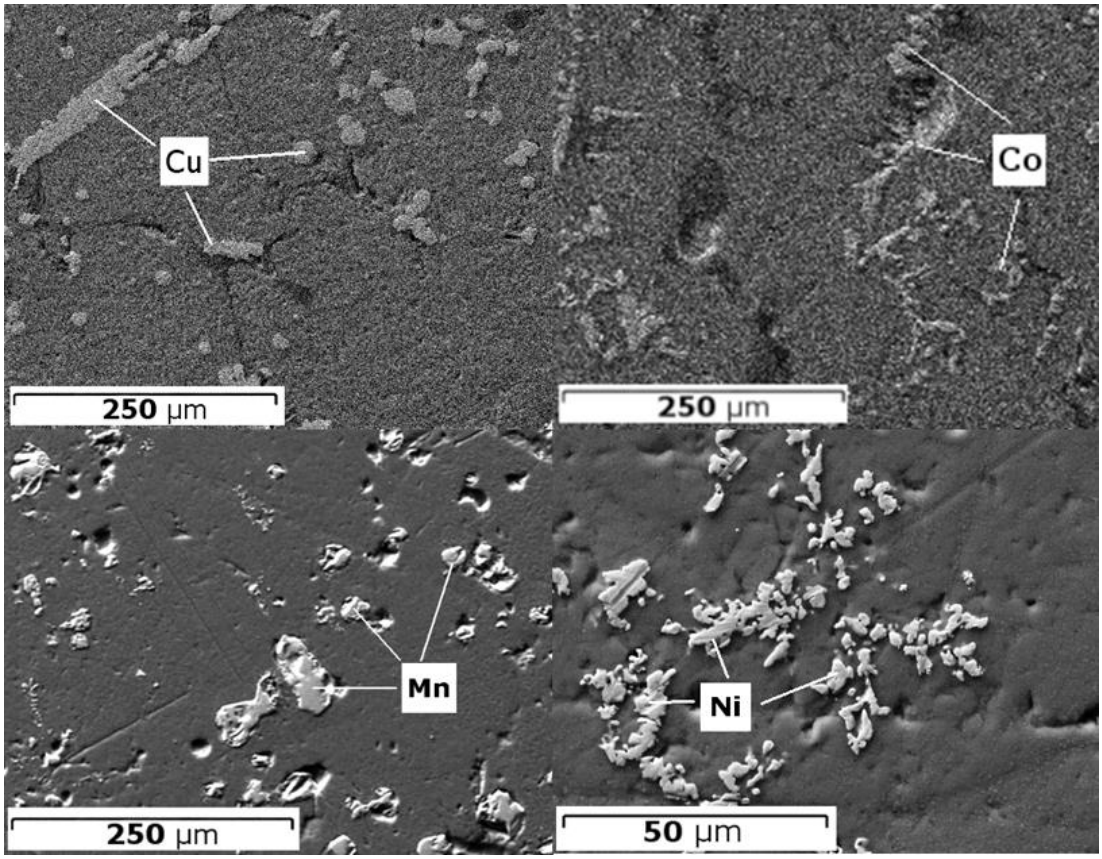


*Figure 6.3-7 Scanning electron microscope image of the metal deposits. Acceleration voltage of 20 kV was used, aperture of 30 microns, Secondary Electron (SE) detector was used to take the pictures. Samples were polished and carbon coated before the analysis.*

## 6.4. Chronoamperometric electrodeposition process analysis

The structure of the metal deposits is expected to be dendritic, as a result of the process being diffusion limited. The observed electric current behaviour should correlate to the diffusion parameters and the electrode surface area change caused by the dendritic growth. Dendritic deposits are easy to retrieve from the electrode by mechanical separation, which would be of benefit in case of automation or a semi-continuous process setup.

Chronoamperometric profiles were recorded as shown in Figure 6.4-1. The high current at the beginning of the process can be ascribed to the high initial reactants concentration on the surface of the cathode, which rapidly decreases as the diffusion layer is being formed. The electrochemical reactions occurring at the electrodes are identical to the previously described reactions (6.3-1) to (6.3-3).

As can be seen in Figure 6.4-1, both copper and silver start at similar current value, however silver remains at a stable value after forming the diffusion layer, while copper sample shows a significant electric current increase over time. With the assumption of no relevant side reactions happening at the electrodes, the observed electric current increase can be originating from shuttling of the reduced metal particles between the electrodes, electrode surface area increase caused by metal deposition, or reduction of the high energetic barrier for copper to plate on tungsten as copper layer forms on the electrode. For comparison, silver was plated at an elevated temperature of 1000 $^{O}$C. At this temperature silver remains liquid after deposition, forming metal droplets on the surface of the electrode instead of dendrites, minimising the surface to volume ratio variation. The potential surface increase would be related to the radius of the droplets formed rather than the significantly larger surface area of dendritic deposits. Figure 6.4-1 shows that the electric current increase is negligible in case of molten silver deposition. This supports the hypothesis of the electrode surface area increase originating from dendritic growth as the main contributor to the current increase.

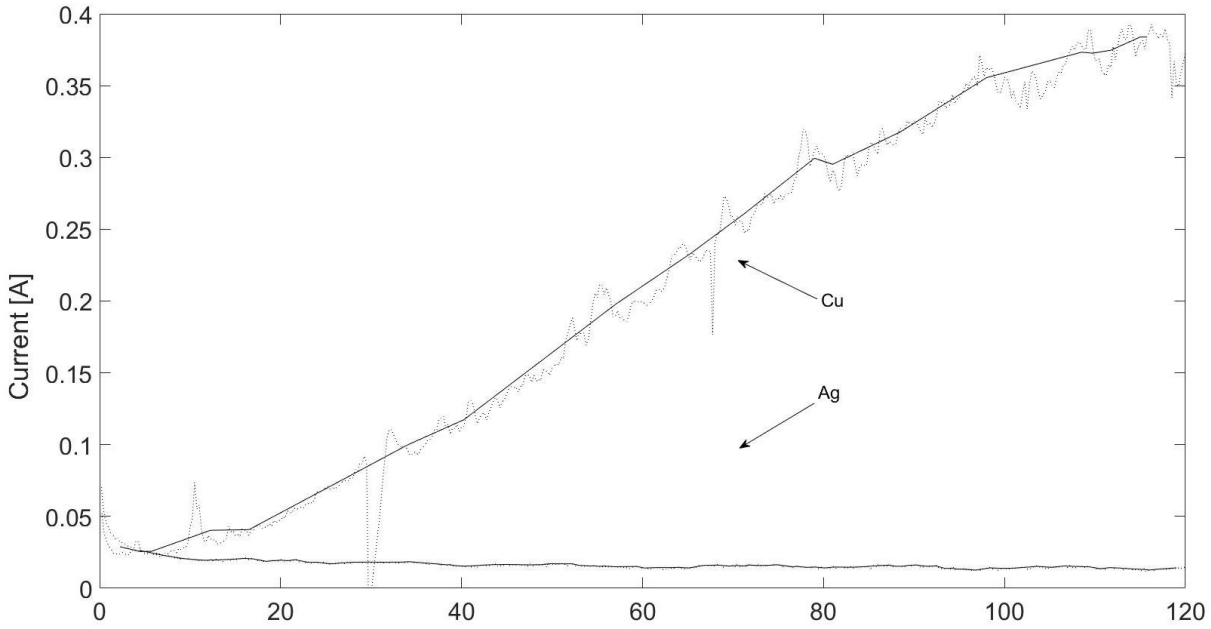


*Figure 6.4-1 Plating profiles comparison – copper (900 $^{O}$C) and silver (1000 $^{O}$C) deposition on identical flat disc electrodes (0.0314cm$^2$), form their respective chlorides in an NaCl melt. Reduction potentials: Ag -900 mV, Cu -450 mV. WE: tungsten, CE: graphite, QRE: tungsten. Solid black lines represent smoothened trend of raw (dotted line) data.*

It was observed that the current change occurring during the process is also connected to the initial surface area of the electrode used. Figure 6.4-2 represents a copper plating profile on a relatively large 1.32 cm$^2$ rod electrode, when compared to the Figure 6.4-1 profiles obtained using a flat-disc electrode with a 0.031 cm$^2$ initial surface area. There is no rapid current increase in case of larger electrode; however, the silver sample still shows greater current stability in comparison, even on a smaller electrode. This suggests that the observed current variations are an electrode surface-related phenomenon, associated with the surface/volume ratio of the metallic deposits, and the initial electrode surface area.

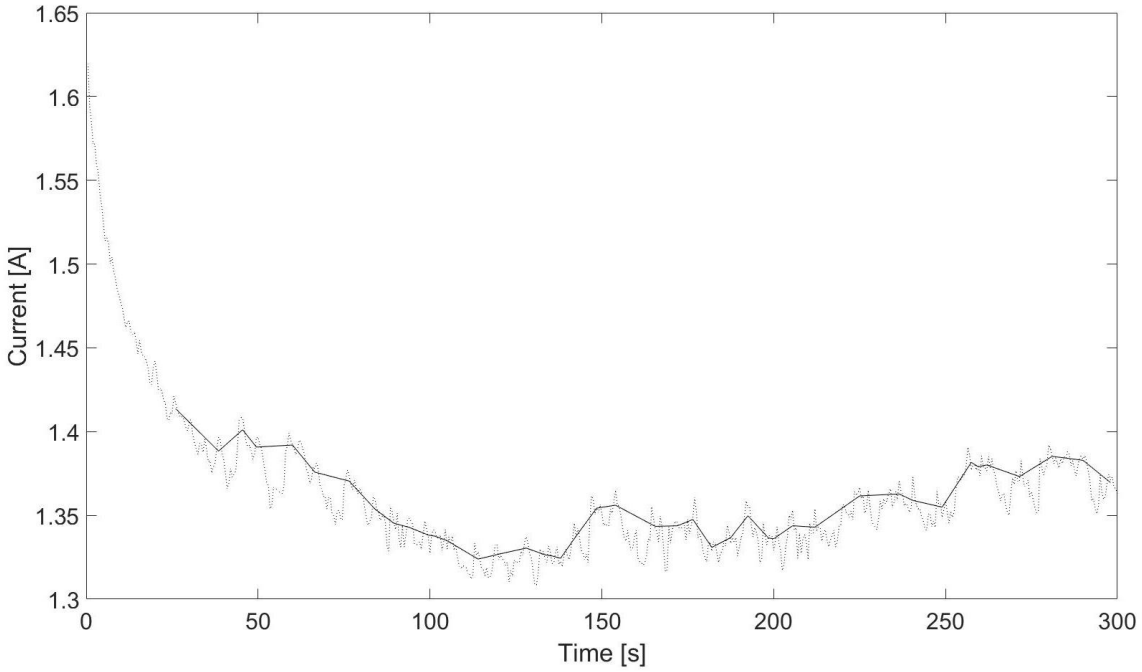


*Figure 6.4-2 Plating profiles comparison – copper plating (at 900 $^{O}$C) on a relatively larger surface rod electrode from 1 wt% CuCl in an NaCl melt. Reduction potential: Cu -450 mV vs tungsten. WE: tungsten, CE: graphite, QRE: tungsten. Initial fall in the current can be seen as the diffusion layer forms, and a subsequent increase in current follows although at a smaller rate, as the initial electrode surface is relatively large. Solid black lines represent smoothened trend of raw (dotted line) data.*

The current increase difference for small and large initial surface electrodes can be explained by the relative surface area change, which is of bigger impact on a smaller electrode. The initial diffusion layer formation phase, connected with the high starting current area at the beginning of the graph and its rapid decline, is much shorter for the smaller electrode as it takes less time to reduce the metal ions present in the close proximity of the cathode. As shown by the initial high current, a significant amount of metal can be deposited at the early stage of the process. Dendritic growth on the electrode surface has a significant impact on the surface to initial surface ratio of the small electrode (Figure 6.4-1), and a relatively smaller impact on the bigger electrode (Figure 6.4-2), resulting in an insignificant surface area change. This influence can be quantified and correlated with the experimentally observed electric current increase, as will be described later in this section.

Alternatively, the plating current increase can be caused by lowering of the kinetic barriers in number of ways. Firstly, plating overpotential for tungsten substrate can be higher than for

copper, resulting in preferential plating on the already-nucleated copper sites, as more are accessible with the ongoing process. Such phenomenon has been observed previously when plating Pb on carbon substrate [125], as previously discussed. Secondly, due to the change in the electrode geometry, higher current-density areas are formed, especially at the peaks of the metallic dendrites, intensifying the electroplating reaction in that region. Finally, change in geometry of the electrode surface results in unequal ion availability and diffusion geometry, furthermore perpetuating the dendritic growth [181].

**Deposits structural analysis**

The structure of the metallic dendrites was analysed using X-ray Computed Tomography and compared against the relatively flat surface of the plated silver droplet. X-CT was used to obtain a 3D reconstructed model of the deposited metal structure, shown in Figure 6.4-3a. The semi-transparent green represents the chloride, peeled away to reveal the considered metallic deposit. Clear identification and segmentation through a multi-level thresholding method is possible as the chloride and metal have a significantly different atomic numbers [182].

The high-density metal shows a relatively random tree-like structure with streaks of ordered material. This structure exhibits a very high surface-to-volume ratio, resulting in the rapid increase in the surface area of the electrode during the process. A smaller region of the deposit is shown in Figure 6.4-3b, where a regular highly dendritic structure can be seen and long branches of metal with perpendicular projections are visible. The deposited metal matrix can be easily crushed/broken off the electrode, which allows for easy recovery of both the metal considered and tungsten electrode.

The presented structure is commonly reported by other researchers [125,126,180] as to be originating from the diffusion control of the metal deposition process. As the diffusion layer is formed [114], analyte has to move towards the electrode from the bulk electrolyte, where the concentration is higher and can be assumed constant in a semi-infinite systems [123], which is relevant to our setup. As the ion is reduced as soon as it touches the metallic electrode surface, previously-deposited dendrites protruding from the surface are the preferential deposition areas due to their easier accessibility, higher charge and shorter diffusion path. All of these effects further perpetuate the diffusion growth of the deposits.

As previously mentioned in section 2.3, overpotential above the peak reduction potential are in the diffusion controlled region, therefore reducing the operating plating potential could limit

the diffusion effect on the deposition. Additionally, mixing could aid the diffusion with convection mass transfer mode [123], resulting in smoother deposits. Finally, higher operating temperature would lower the viscosity of the melt, increase the diffusion coefficients [170,183], and eventually result in a molten metal deposition, which would take a smooth droplet-like form. Example is given by electroplating silver as 1000 $^{O}$C, as discussed later in this section.

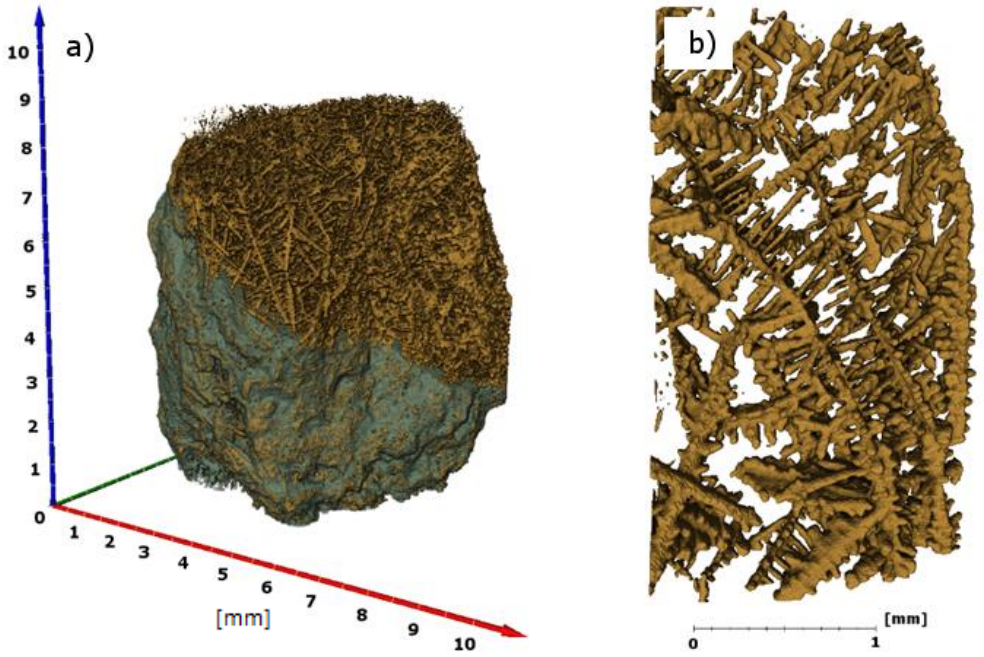


*Figure 6.4-3 3D reconstructed metal deposits obtained from a long deposition process on a rod tungsten electrode. X-CT scan parameters are described in text.*
*a.) A complete 3D model, b.) Smaller region under higher magnification*

By contrast, the silver deposit shown in Figure 6.4-4 and 6.4-5 show a very smooth surface. The FEG-SEM X-EDS picture represents the tungsten electrode tip cross-section after the silver electrodeposition. No dendrites can be seen, which is in agreement with our assumptions and the constant electric current visible on the chronoamperometric profile in Figure 6.4-1. However, the silver metal deposit was much more closely connected with the electrode surface, making it significantly harder to mechanically separate it from the tungsten rod.

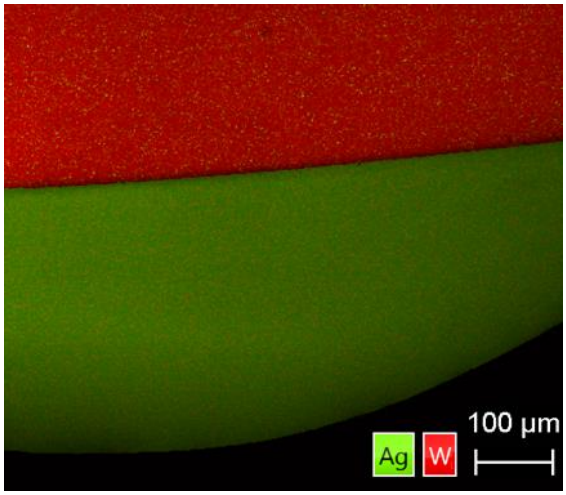


*Figure 6.4-4 FEG-SEM X-EDS scan of the silver deposit on a flat disc tungsten electrode. Acceleration voltage of 20 kV was used, aperture of 30 microns. No silver can be spotted in the tungsten (no alloying) and a smooth silver surface is clearly visible, suggesting no dendritic growth.*

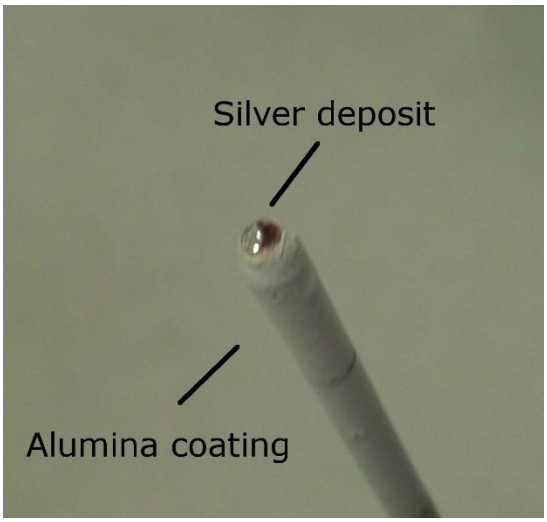


*Figure 6.4-5 Silver deposit on a tungsten flat-disc electrode. Plating potential: -900 mV vs tungsten, at the temperature of 900 $^{O}C$ from an 1wt% AgCl in NaCl mixture. WE: tungsten, CE: graphite, QRE: tungsten.*

**Electrode surface growth evaluation**

The electrode surface change was calculated using the chronoamperometric experiments data collected during the electro-deposition of copper. Cottrell equation (4.4-3) was used for calculations, as explained in the *Experimental* section. Parameters used for calculations were as follows: *D (calculated)* = 1.35e$^{-4}$ [$cm^2\ s^{-1}$], $F$ = 96485 [$C\ mol^{-1}$], $n$ = 2, and $c^{\infty}$= 0.116 [$mol\ dm^{-3}$]. The assumed initial electrode surface $A$ was that of the small disc electrode equal

to 0.0314 $cm^2$. The experimental electric current $I$ values (Cu: -450 mV, Ag: -900 mV) were obtained from the potentiostatic measurements, after the initial diffusion layer formation phase.

Alternatively, surface area increase can be calculated using the surface area to volume ratio (SA/V) estimated from the X-CT data. The ratio was estimated at 966.676 [$cm^{-1}$] for dendritic metal deposits. The sample used was produced by electroplating for an extended period of time to obtain a fragment big enough to be fitted onto the X-CT scanning machine sample holder. The reported SA/V ratio was used to calculate the expected surface growth based on the amount of electric charge passed, as in the following equations (6.4-1) and (6.4-2). Back-dissolution and imperfect current efficiency effects were not accounted for. The SA/V ratio was used as a constant value, which is only correct for a limited time as the growing dendrites will fuse into each other and create regions cut off from the bulk salt, resulting in the so-called reactor dead zones. This would reduce the accessible electrode surface, lowering the surface area growth.

$$m = \frac{(Q\ A)}{(n\ F)} \tag{6.4-1}$$

$$S = S_0 + \frac{m}{\rho}\ X \tag{6.4-2}$$

where: $m$ – mass of the metal deposited [$g$], $A$ – atomic mass of the element [$g\ mol^{-1}$], $n$ – number of the electrons exchanged in the red-ox reaction, $Q$ – electric charge passed through the electrode [$C$], $F$ – Faraday constant [$C\ mol^{-1}$], $S$ – electrode surface [$cm^2$], $S_0$ – initial electrode surface [$cm^2$], $X$ – surface-to-volume ratio [$cm^{-1}$] and $\rho$ – metal density [$cm^3\ g^{-1}$].

Significant surface area increase can be observed using both calculation methods, as shown in Figure 6.4-6, where the relative current and surface increase is plotted. Closely fitting trends can be observed for the surface area growth and experimentally measured electric current increase. This supports the hypothesis that the current variations are caused and can be quantitatively explained by the rapid surface area growth. As such, the current density remains constant for the duration of the process. Complex and highly developed electrode surface is created by the dendritic structure, which results in a significant surface area increase and the observed electric current gain. This phenomenon is expected to decline at a later stage of the process, when the metallic dendrites start to fuse together and create the stagnant regions, limiting the electrode surface development.

The surface growth calculated from the X-CT surface-to-volume ratio fits closer with the electric current increase, when compared to the Cottrell-derived trend. This is likely caused by the diffusion coefficients calculated from the Stokes-Einstein equation, which can be different from the non-ideal values. Alternatively, the disparity could originate from the electroplating current loss as a result of shuttling, side reactions, back-dissolution of the metal and/or imperfect current efficiency, or the aforementioned kinetics alteration by the change in the electrode structure or preferential copper-on-copper plating. As a result, not all of the experimentally measured charge passed would correspond to the metal being successfully electroplated.

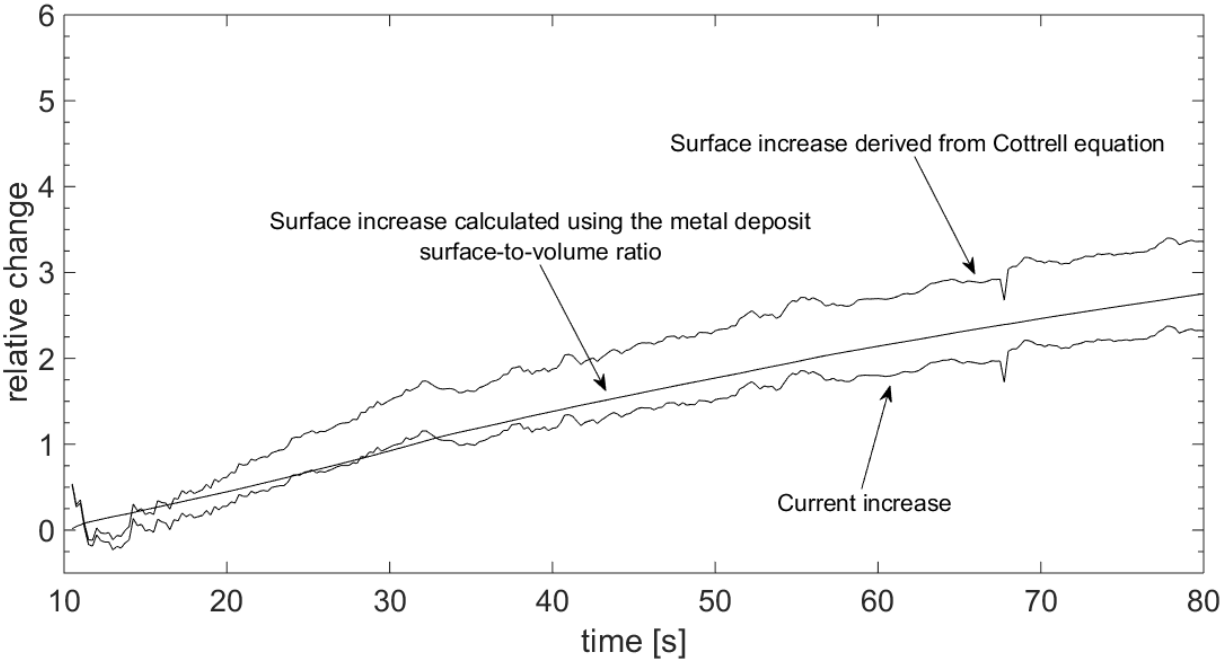


*Figure 6.4-6 Electric current and surface increase correlation for copper electrolysis from molten sodium chloride at 900 $^{O}$C on a flat disc electrode. Plating potential of -450 mV was applied. WE: tungsten, CE: graphite, QRE: tungsten. The y-axis represents the electric current and electrode surface area increase factors. Rapid and similar increase can be seen in both electroplating current and the surface, supporting the hypothesis of the surface increase resulting in an increased current.*

The hypothesis stated at the beginning of this section has been confirmed. The produced metal deposits were analysed and the calculated surface area growth is in all cases proportional to the experimentally obtained electric current trend. This can explain the phenomenon of rapid electric current increase observed during the process. The current growth is most probably caused by the increase in the electrode surface area, and can be directly correlated with the use

of the X-CT measured surface-to-volume ratio of the metal deposits or the Cottrell equation. However, kinetics change due to the electrode geometry and structure alteration can also be of influence, resulting in presence of preferential plating areas and current density variations, possibly explaining the slight discrepancies in the presented results. The experiments also show that the evaluated electrolytic cell setup allows for recovery of both molten and solid dendritic metal deposits, making it a versatile base for metal electrodeposition systems. However, while the obtained dendritic metal deposits could be easily broken off the electrode, offering no difficulty in the mechanical recovery from the system, in case of molten metal deposition the separation is more challenging due to the high adherence to the electrode.

Knowing that the dendritic growth is present in the system evaluated in this work, one has to consider its effect on the Cyclic Voltammetry measurements as well. Due to the increasing electrode surface and its geometry, potentially leading to a lower kinetic barrier of the electroreduction process, peak shifts could be observed in case a significant number of CV scans is plotted. Due to the lower kinetic barriers, the process would occur at lower potentials, which would manifest itself as the reduction peak shift towards the more positive values. Additionally, larger surface and its more complex geometry will lead to an increased charge passing through the electrode, which in turn would increase the peaks observable height. Such phenomena have to be kept in mind when evaluating similar systems, as it can lead to the measurements aberration if proper care is not taken to avoid unnecessary high number of scans.

# 7. Economic analysis

Considering the economic aspects of the process evaluated in this work, it offers certain benefits over the previously analysed hydro- and pyro-metallurgical methods. The process proposed uses two salts for the bulk of the cell, both of which are quite prevalent and naturally occurring [100,184]. There are no heavily corrosive and expensive acids used (e.g. hydrofluoric or sulfuric acids), which removes the adverse environmental effect of these as well [15]. This allows for zero water-waste production, which is of growing concern as the contaminated water disposal costs are growing, amplified by the pressure of the pro-ecological approach and governmental incentives to reduce the waste output.

Regarding the pre-treatment of feed materials, hydrometallurgical methods require certain (small) particle size for the acid leeching to reach required concentrations [44,185], while the evaluated method would not require such, as it could work on a pellet-size metal source even without additional mixing. This removes the need of additional milling and thermal pre-treatment steps, which reduces the cost of feed preparation.

The overall cost of the process can be divided into the initial expenditure, i.e. equipment, and the ongoing electricity consumption. Following calculations can be made using the example of cobalt as the rarest of the recovered metals at the price of £16.19 per kg of Co as set by the London Metal Exchange [186] and the average business electricity rate in the UK [187] at 9.26 p/kWh. The amount of electric energy required to plate 1 g of cobalt can be calculated using the Faraday's law of electrolysis equation (7-1):

$$Q = \frac{m\,F\,n}{M} \tag{7-1}$$

where: $Q$ – electric charge $[C]$, $F$ – Faraday constant equal 96485 $[C\ mol^{-1}]$, $n$ – number of electrons exchange in the redox reaction equal 2, $M$ – molar mass of the substance equal 58.933 $[g\ mol^{-1}]$ and $m$ – mass of the substance liberated $[g]$ assumed to be 1 g. The result is: $Q = 0.9096\ [Ah]$

The electrolysis parameters were obtained experimentally as described in section 5.2. The full-cell potential value of -1.848 V is required for the $Co^{2+}$ electroreduction from the two-phase cell system at the achieved concentration of 0.121 mol $dm^{-3}$. This results in the following theoretical electric energy consumption of the process calculated with the equation (7-2):

$$E = P\,t = |U|\,Q \tag{7-2}$$

where: $E$ – electric energy [$Wh$], $P$ – power [$W$], $t$ – time [$s$], $U$ – potential [$V$]. $Q$ – charge [$C$]. The resulting energy requirement is: $E = 1.6810\ [Wh]$

**At the assumed electricity rate, the theoretical cost of electricity required for the electroreduction of 1 g of cobalt equals 0.0156 p.** This means that the electricity cost is negligible for the amount of metal recovered and the major cost will probably result from a different process element. While some overpotential might need to be applied during the process (e.g. due to the higher assembly resistance, concentration variations), it would not increase the overall cost significantly, as discussed in the later part of this section.

As the time of the process is dictated by the limiting current, the value of which was obtained experimentally as described in section 6.2. The limiting current value observed at the experimental parameters was 0.02 A on a 0.0314 $cm^2$ electrode, which equals to 0.6369 A $cm^{-2}$ current density for cobalt electroreduction in the evaluated system. While for the simplification the current density can be assumed similar for larger electrodes, it needs to be noted it might not be the case and as a result, the efficiency might be lower than theoretically calculated.

More importantly, in case of a larger vessels the internal resistances would increase. As there will be bigger distance between the larger electrodes, longer connections and current collectors, the overall resistance of the system will increase. This will result in some of the energy being turned into waste heat, as well as need for increased overpotential applied. However, as will be discussed later in this section, that heat can be used to minimise the amount of external heating applied to reduce the heating cost.

The tests were conducted in a GVA 12/300 *Carbolite*® furnace using resistance heating elements, which required 1725 Watts of energy to keep the furnace at the working temperature of 900 $^{O}$C. **This translates to 15.97 p of electricity cost for 1 hour of the furnace working at the process temperature**. Therefore, the electrolysis cost is negligible when compared to the heat generation cost required during the evaluated process. To plate 1 g of cobalt a charge of 0.9096 Ah has to pass through the electrode, which would take 9 hours and 19 minutes using a 1 $cm^2$ surface area electrode. This would result in 148.86 p cost of furnace heat generation in comparison to 0.00156 p of electricity cost for electrolysis.

However, these considerations become less relevant on an industrial scale because of the following: the loss due to the electrode/cell resistance is small on a small scale, yet becomes significant if industrial-scale vessels are considered., e.g. in the Hall-Héroult process [188].

Almost two-thirds of the heat is reported to be generated in the electrolyte, the rest on the electrodes and external connections. As such, after the initial temperature increase to enable the process, the heat generated in the process can be sufficient to keep the melting temperature [151]. Precise heat balancing, especially considering the current density influence, should be done to avoid overheating/cooling if a significant upscale is attempted. Still, the process assembly would need to be able to heat up the mix in order to start the process, and potentially cool it down if the heat-generation exceeds the heat loss through radiation and diffusion.

The profitable amount of metal to recover from the initial feed will vary depending on the electrolytic cell setup. As the metal concentration decreases, the current density will deteriorate resulting in a slower process [114]. The optimal recovery rate will depend on the initial metal concentration, electrolytic cell size, electrode surface and the cost threshold, which is specific to each case, as well as the heat generation depending on the current density.

The initial cost of the process would involve the equipment expenditure, which in case of the laboratory scale consisted of £2900 for the furnace (GVA 12/300, *Carbolite*®) and the electrodes cost at £88 (tungsten rod 500m, Goodfellow Cambridge Ltd.) and £5.66 (graphite rod 150mm, Sigma-Aldrich®). The salts cost was respectively £160 and £20 for 1kg of high purity borax and sodium chloride (Sigma-Aldrich®), however at the industrial rate the price falls to £0.5 and £0.04 per kg. This again underlines the cost reduction related to the up-scaled production. Additionally, cost of a significantly bigger electrolytic vessel/furnace setup would increase the cost, however it would be more cost efficient per usable volume, especially considering the process heat generation that would reduce the electricity consumption rate.

It is evident that, after the initial setup, the most significant process cost contribution would be the electricity usage, making the price-per-mass-unit of the plated metal relatively high. Nonetheless, the electricity cost would be driven lower by other research sectors (e.g. nuclear, renewables), enabling and promoting electrolysis-oriented systems. Furthermore, the process could utilise process heat from the electrolysis itself, significantly reducing the cost contribution, or the residual heat present in other sectors of the metal industry. As suggested in the analysis, significant cost-per-unit reduction can be achieved by the up-scale of the process and competitive prices of metal can be potentially achieved with optimal engineering solutions in place, e.g. heat balancing, the process itself is not labour intensive, and can be easily automated. Additionally, due to the used chemicals being cheap and easily accessible, this method has low running materials requirements, reliant mostly on the electricity supply.

When compared with other available methods as was done in section 2.2.1, this unique and novel process allows for recovery of a wide range of feedstock, while remaining capable of recovery of all of the valuable metals present rather than using it as a secondary-feed for alloys production. Additionally, the process offers clean solution without the use of toxic acids for leaching and significant amounts of water, minimising the adverse effects on the environment, an effect especially important when on a large scale. Finally, the flexibility of the system allows for recovery of the ever-changing chemistries of the eWaste, without the need of costly and complex refurbishing of the electrolytic cell. With the development of the process and growing metal industry needs, the benefits of complete, clean and diverse metal recovery from a wide range of feedstock would outweigh the cost, especially considering the increasing environmental concerns and waste disposal costs.

# 8. Conclusions

The focus of this study was to create and evaluate a new proof-of-concept molten salt two-phase metal recovery method capable of recovering valuable metals from the eWaste stream. Within this work, a completely novel metal recovery process has been developed and the investigation of the fundamental system thermodynamics was undertaken, as they were not previously evaluated by other researchers The scope of this thesis includes a range of valuable metals present in the Li-ion and Ni-MH batteries, precisely: cobalt, copper, manganese and nickel. The thermodynamics of the melt electrolysis were evaluated by means of electro-analytical methods and materials characterisation methods like SEM-EDS and XRD were used to analyse the processed salts composition and the electroreduction products.

A two-phase molten salt system composed of sodium borate ($Na_2O$-$2B_2O_3$) and sodium chloride (NaCl) was designed, evaluated and used for metal recovery. The feed tested includes oxides and chlorides of Co, Cu, Mn and Ni, as representation of the Li-ion and Ni-MH waste composition. The tests were conducted in a three-electrode setup using tungsten (W) working electrode, graphite (C) counter-electrode and a tungsten (W) quasi-reference electrode to avoid introducing contaminations. The process was operating at the temperature of 900 $^{O}$C / 1173 K, which is a balance between the melting points of the salts used and metals deposited (based on their phase diagrams created using thermodynamic software), and the stability of the materials used. The cell was running in a gas-tight vertical tube furnace under argon atmosphere. This was a one-vessel assembly utilising the immiscibility of the two liquid phases used; however, a three-vessel version of the system has been proposed as well, both akin to an industrial set-up idea, their *pro et contra* and up-scale limitations discussed.

The system evaluated was designed to work with metals present in the eWaste stream composed of lithium ion and nickel metal hydride batteries; however, due to the chemical stability of the salts system used it could work with other metal sources as well, e.g. metal-accumulating biomass mentioned in the introduction section. The suggested system provides an alternative to the single-phase or aqueous metal recovery methods, while solving the issues related to the hydrometallurgical methods including significant amounts of water waste, sulphates by-products presence and toxic acids use resulting in highly detrimental effects on the environment. Additionally, the method developed is inclusive of a range of metals, which is of high importance considering the growing complexity of the eWaste stream.

Little to no work has been done in this dual salt system beforehand regarding various metal oxides solubility, and so this first step of the process was studied carefully and resulted in novel results produced. The equilibrium solubility study of the metal oxides, precisely $Cu_2O$, CuO, $Co_3O_4$, $Mn_2O_3$ and NiO in borate glass has been described in section 5.1. The solubility can be greatly increased by adding network modifiers, i.e. alkali metal oxides, changing the structure of the highly polymeric molten borate as described in section 2.3.2, and adding negative exchange sites, increasing the overall metal cation affinity of the melt. Significant solubility has been achieved by using the $Na_2O$-$2B_2O_3$ molten salt, with the metals concentration ranging between 4-20 wt%, which is sufficient for the later steps of the process.

Similarly, the transfer of the metal ions into the chloride layer has been analysed. The chemical reaction (2.3-9) occurring at the liquid-liquid interface results in metal chlorides being present in the upper halide layer; however, the metals concentration achieved was considerably lower (~1 wt%) due to the high metal ions affinity towards the oxide layer leading to an unfavourable partition coefficient. However, as the interface exchange is chemical reaction driven, the recovery process can continue with the sustained feed of metal ions from the metal-rich borate layer.

In section 5.2. the electrochemistry of the system is evaluated. All of the metals considered were successfully plated from the suggested two-phase cell system and compared against a simplified one-phase system for the thermodynamic analysis of the process. The system was evaluated in a three-electrode set-up and the formal redox reaction potentials were reported for the following feedstock: $Co_2O_3$ [-0.733/-1.848 V], CuO [-1.297/-2.375 V], $Mn_2O_3$ [-1.552 V] and NiO [-1.734 V] versus chlorine evolution. The solvation and other influences were accounted for using an empirical equation 6.3-7, created by comparing thermodynamic and experimental redox potentials. The electrochemical evaluation allowed for separate analysis of each metal behaviour during the electrolysis process. It was observed that the electrolysis profiles changed when compared to the single-phase system, because of different metal ions oxidation states transported from the oxide layer, resulting in different melt compositions.

Recovered metals were chemically analysed, their purity was measured using SEM-EDS and was found as follows: >98% for Cu, >99% for Co, >99% for Mn, and >99% for Ni. The lack of boron in the deposits was verified using ICP-OES, confirming the complete partition of the molten phases. The metals for analysis were electroplated by means of chronoamperometry and the data gathered was used for mathematical correlation of the current changes with the

electrode area growth measured using Stokes-Einstein diffusion model, Cottrell equation and X-CT scanning for the copper case. Significant current increase over time was observed and concluded to originate from the highly dendritic deposits structure, resulting in rapidly growing electrode surface area. Recovered copper deposits were reconstructed in 3D and showed a highly dendritic structure with surface-to-volume ratio of almost 1000 $cm^{-1}$. Such a structure is common for diffusion-controlled processes, as is the case in the cell studied, especially when applying high overpotentials.

Economic analysis of the process shows that heat generation is the most significant constituent of the overall cost per unit of the recovered metal when operating on a laboratory scale. Under simplified assumptions it was concluded that in case of the up-scale the process heat could be sufficient to minimise the need for external heating once the process starts, similarly to the Hall-Héroult process. This would significantly increase the feasibility of the process. The observations underscore the importance of the scale-up required to lower the production cost. Further feasibility analysis would require current efficiency and its correlation with the electrode size analysis, which is a subject for future work on this system. As the cost of the electricity falls down with new power generation methods, waste-disposal costs increase and the rare and valuable metal sources diminish, the competitiveness of the method developed increases offering a viable concept for the benefit of the future industry.

# 9. Future work

Although progress is being made in the molten salts metal recovery and this work evaluated some features of the molten borate-chloride two-phase system, there are areas that need to be addressed for future study. Further exploration of the dissolution and metal ions partition in the two-phase molten salt systems is suggested, in particular the influence of the oxygen partial pressure on the partition coefficients of the metals of interest. It would expand the understanding of the thermodynamics behind the metal ions partition between the molten oxide and halide phases and could be used for better two-phase molten salts processes control.

Alternatively, the liquid-liquid interface evaluation could be done with the use of the novel double-hot thermocouple technique [189]. Such method would allow optical and electrochemical observations at the same time, enabling analysis of such a complex reaction as a liquid-liquid interface ionic transfer. An intricate, purpose-built in-house assembly would have to be made, for the benefit of better understanding of this complex process kinetics and thermodynamics.

Furthermore, the kinetics of metal ions dissolution into the borate melt were not extensively studied, which offers limited confidence regarding the speed of this process. The high-temperature liquid-liquid and liquid-solid interactions investigation is non-trivial; however, it can be of great benefit to our understanding of the molten salts kinetics.

Improvement in the electrolysis cell design could be made, e.g. by experimenting with different electrode materials. Tungsten was selected for its thermal resistance and chemical stability; however, different metals could offer better performance or interesting alloying opportunities, e.g. liquid aluminium cathode. Additionally, while the recovery of both dendritic copper deposits and molten silver phase shows that the proposed system could work for a range of metal deposits, efficient metal collection from the assembly would be a subject of future work. In the current assembly the process had to be fully stopped to allow for safe metal rods extraction, which is highly impractical.

Further improvements to the process could be made through efficiency analysis, identifying potential energy losses and process design flaws. Faradaic efficiency analysis would be beneficial, which requires reliable deposited metal recovery method. X-CT or BET techniques could be used for the recovered deposits structural analysis. While the testing was conducted using high grade chemicals, the use of actual waste mixes could result in other elements

presence in the melt causing some current efficiency drop, increasing the energy required for the metal electrodeposition. However, as mentioned in section 7 the significantly larger part of the process cost at small scale is the heat generation, which optimisation would greatly benefit the feasibility of the process designed. Heat balancing would be required in order to achieve an optimal thermal equilibrium between the process heat generation and heat losses.

The optimisation and up-scale of the process would be an interesting subject for future investigation, potentially including a different, multi-vessel dissolution and electrolysis setup. As mentioned in chapter 7, an up-scaled process would be much more beneficial, turning into an economically feasible recycling method. Other metal feeds could also be experimented with, widening the range of the evaluated molten salts systems and benefitting the molten salts metal recovery research. The suggested engineering solutions regarding the process control and electrode materials could lead to easier metals separation and recovery from the proposed system.

# Bibliography


[1] F.J. Dyson, Search for Artificial Stellar Sources of Infrared Radiation., Science (80-. ). 131 (1960) 1667–8. doi:10.1126/science.131.3414.1667.

[2] D. Deng, Li-ion batteries: basics, progress, and challenges, Energy Sci. Eng. 3 (2015) 385–418. doi:10.1002/ese3.95.

[3] W. Sunk, Survey of metal recovery in the USWTE industry, in: Nawtec 15 Proc. 15th Annu. North Am. Waste to Energy Conf., 2007. <Go to ISI>://000252171300028.

[4] European Commission DG Enterprise and Industry, Critical raw materials for the EU - Report of the Ad-hoc Working Group on defining critical raw materials, 2010.

[5] U.S. Department of Energy (DOE) Office of Policy and International Affairs, Critical Materials strategy, 2011.

[6] P. Jiang, M. Harney, Y. Song, B. Chen, Q. Chen, T. Chen, G. Lazarus, L.H. Dubois, M.B. Korzenski, Improving the End-of-Life for Electronic Materials via Sustainable Recycling Methods, Procedia Environ. Sci. 16 (2012) 485–490. doi:10.1016/j.proenv.2012.10.066.

[7] H. Vikström, S. Davidsson, M. Höök, Lithium availability and future production outlooks, Appl. Energy. 110 (2013) 252–266. doi:10.1016/j.apenergy.2013.04.005.

[8] J.R. Dodson, A.J. Hunt, H.L. Parker, Y. Yang, J.H. Clark, Elemental sustainability: Towards the total recovery of scarce metals, Chem. Eng. Process. Process Intensif. 51 (2012) 69–78. doi:10.1016/j.cep.2011.09.008.

[9] A. Hern, Tesla Motors receives $10bn in Model 3 pre-orders in just two days, Guard. (2016). https://www.theguardian.com/technology/2016/apr/04/tesla-motors-sells-10bn-model-3-two-days (accessed June 6, 2016).

[10] C. Johnston, Tesla's batteries could be bigger business than electric cars – Elon Musk, Guard. (2015). https://www.theguardian.com/technology/2015/may/07/teslas-batteries-could-be-bigger-business-than-electric-cars-elon-musk (accessed June 6, 2016).

[11] L. Gaines, R. Cuenca, Costs of lithium-ion batteries for vehicles, Argonne, IL, 2000. doi:10.2172/761281.

[12] J.H. Miedema, H.C. Moll, Lithium availability in the EU27 for battery-driven vehicles: The impact of recycling and substitution on the confrontation between supply and demand until2050, Resour. Policy. 38 (2013) 204–211. doi:10.1016/j.resourpol.2013.01.001.

[13] D. Kushnir, B.A. Sandén, The time dimension and lithium resource constraints for electric vehicles, Resour. Policy. 37 (2012) 93–103. doi:10.1016/j.resourpol.2011.11.003.

[14] T. Georgi-Maschler, B. Friedrich, R. Weyhe, H. Heegn, M. Rutz, Development of a recycling process for Li-ion batteries, J. Power Sources. 207 (2012) 173–182. doi:10.1016/j.jpowsour.2012.01.152.

[15] S.M. Shin, N.H. Kim, J.S. Sohn, D.H. Yang, Y.H. Kim, Development of a metal recovery process from Li-ion battery wastes, Hydrometallurgy. 79 (2005) 172–181. doi:10.1016/j.hydromet.2005.06.004.

[16] M. Contestabile, S. Panero, B. Scrosati, A laboratory-scale lithium-ion battery recycling process, J. Power Sources. 92 (2001) 65–69. doi:10.1016/S0378-7753(00)00523-1.

[17] J. Myoung, Y. Jung, J. Lee, Y. Tak, Cobalt oxide preparation from waste LiCoO2 by electrochemical–hydrothermal method, J. Power Sources. 112 (2002) 639–642. http://www.sciencedirect.com/science/article/pii/S0378775302004597 (accessed January 9,

2014).

[18] H. Yoshida, S. Izhar, E. Nishio, Y. Utsumi, N. Kakimori, S. Asghari Feridoun, Recovery of indium from TFT and CF glasses in LCD panel wastes using sub-critical water, Sol. Energy Mater. Sol. Cells. 125 (2014) 14–19. doi:10.1016/j.solmat.2014.02.009.

[19] J. Nan, D. Han, M. Yang, M. Cui, X. Hou, Recovery of metal values from a mixture of spent lithium-ion batteries and nickel-metal hydride batteries, Hydrometallurgy. 84 (2006) 75–80. doi:10.1016/j.hydromet.2006.03.059.

[20] B.G. Pollet, I. Staffell, J.L. Shang, Current status of hybrid, battery and fuel cell electric vehicles: From electrochemistry to market prospects, Electrochim. Acta. 84 (2012) 235–249. doi:10.1016/j.electacta.2012.03.172.

[21] S. Zhu, W. He, G. Li, X. Zhou, X. Zhang, J. Huang, Recovery of Co and Li from spent lithium-ion batteries by combination method of acid leaching and chemical precipitation, Trans. Nonferrous Met. Soc. China. 22 (2012) 2274–2281. doi:10.1016/S1003-6326(11)61460-X.

[22] S. Al-Thyabat, T. Nakamura, E. Shibata, A. Iizuka, Adaptation of minerals processing operations for lithium-ion (LiBs) and nickel metal hydride (NiMH) batteries recycling: Critical review, Miner. Eng. 45 (2013) 4–17. doi:10.1016/j.mineng.2012.12.005.

[23] D.E. Williams, A.A. Nobile, D. Inman, Solvent extraction with inorganic liquids at high temperature, Trans. I.M.M. 86 (1977) C35–C37.

[24] C.W. Bale, P. Chartrand, S.A. Decterov, G. Eriksson, K. Hack, R. Ben Mahfound, J. Melancon, A.D. Pelton, S. Petersen, FactSage Thermochemical Software and Databases, Calphad J. 62 (2002) 189–228.

[25] Crushing energy costs in the mining sector, (2013). http://eex.gov.au/2013/11/crushing-energy-costs-in-the-mining-sector/ (accessed June 7, 2016).

[26] A. Lossin, Copper, in: Ullmann's Encycl. Ind. Chem., Wiley-VCH Verlag GmbH & Co. KGaA, 2000. doi:10.1002/14356007.a07_471.

[27] P.H. Kuck, Nickel, 2013.

[28] J.E. Kogel, N.C. Trivedi, J.M. Barker, S.T. Krukowski, Industrial Minerals & Rocks, 7th ed., Society for Mining, Metallurgy and Exploration, Inc., Colorado, 2006.

[29] W. Zhang, C.Y. Cheng, Manganese metallurgy review. Part I: Leaching of ores/secondary materials and recovery of electrolytic/chemical manganese dioxide, Hydrometallurgy. 89 (2007) 137–159. doi:http://dx.doi.org/10.1016/j.hydromet.2007.08.010.

[30] J.J. Barry, G.R. Matos, W.D. Menzie, U.S. Mineral Dependence—Statistical Compilation of U.S. and World Mineral Production, Consumption, and Trade, 1990–2010, 2013. http://pubs.usgs.gov/of/2013/1184/pdf/ofr2013-1184.pdf.

[31] D. Kushnir, B.A. Sandén, The time dimension and lithium resource constraints for electric vehicles, Resour. Policy. 37 (2012) 93–103. doi:10.1016/j.resourpol.2011.11.003.

[32] S.P. Atacama, An increasingly precious metal, Econ. (2016). http://www.economist.com/news/business/21688386-amid-surge-demand-rechargeable-batteries-companies-are-scrambling-supplies (accessed June 7, 2016).

[33] A. Väyrynen, J. Salminen, Lithium ion battery production, J. Chem. Thermodyn. 46 (2012) 80–85. doi:10.1016/j.jct.2011.09.005.

[34] B. Scrosati, J. Garche, Lithium batteries: Status, prospects and future, J. Power Sources. 195 (2010) 2419–2430. doi:10.1016/j.jpowsour.2009.11.048.

[35] Z. Bakenov, I. Taniguchi, Cathode Materials for Lithium-Ion Batteries, in: Lithium-Ion Batter. Adv. Mater. Technol., 2012: pp. 51–96.

[36] S. Santhanagopalan, Z. Zhang, Separators for Lithium-Ion Batteries, in: Lithium-Ion Batter. Adv. Mater. Technol., 2012: pp. 197–252.

[37] M. Narasimha, V. Prasad, H. Maria, D.O. Freitas, Metal hyperaccumulation in plants - Biodiversity prospecting for phytoremediation technology, Electron. J. Biotechnol. 6 (2003) 286–321.

[38] H. Vandenhove, M. Van Hees, Phytoextraction for clean-up of low-level uranium contaminated soil evaluated, J. Environ. Radioact. 72 (2004) 41–45. doi:10.1016/S0265-931X(03)00184-X.

[39] J. Xu, H.R. Thomas, R.W. Francis, K.R. Lum, J. Wang, B. Liang, A review of processes and technologies for the recycling of lithium-ion secondary batteries, J. Power Sources. 177 (2008) 512–527. doi:10.1016/j.jpowsour.2007.11.074.

[40] A. Khaliq, M.A. Rhamdhani, G. Brooks, S. Masood, Metal Extraction Processes for Electronic Waste and Existing Industrial Routes: A Review and Australian Perspective, Resources. (2014) 152–179. doi:10.3390/resources3010152.

[41] M. Caffarey, Umicore Precious Metals Refining, in: Southeast Recycl. Dev. Counc. Summit, 2012: pp. 1–65.

[42] C. for E. Cooperation, Environmentally Sound Management of End-of-Life Batteries from Electric-Drive Vehicles in North America, 2015.

[43] P. van der Werf, MHSW Processor Audit Report - Inmetco, 2011.

[44] L. Chen, X. Tang, Y. Zhang, L. Li, Z. Zeng, Y. Zhang, Process for the recovery of cobalt oxalate from spent lithium-ion batteries, Hydrometallurgy. 108 (2011) 80–86. doi:10.1016/j.hydromet.2011.02.010.

[45] A.A. Nayl, R.A. Elkhashab, S.M. Badawy, M.A. El-Khateeb, Acid leaching of mixed spent Li-ion batteries, Arab. J. Chem. (2014). doi:10.1016/j.arabjc.2014.04.001.

[46] C.K. Lee, K.I. Rhee, Preparation of LiCoO2 from spent lithium-ion batteries, J. Power Sources. 109 (2002) 17–21. doi:10.1016/S0378-7753(02)00037-X.

[47] C. Lee, K. Rhee, Preparation of LiCoO2 from spent lithium-ion batteries, J. Power Sources. 109 (2002) 17–21. http://www.sciencedirect.com/science/article/pii/S037877530200037X (accessed January 9, 2014).

[48] R. Bhagat, M. Jackson, D. Inman, R. Dashwood, Production of Ti–W Alloys from Mixed Oxide Precursors via the FFC Cambridge Process, J. Electrochem. Soc. 156 (2009) E1–E7. doi:10.1149/1.2999340.

[49] R. Bhagat, M. Jackson, D. Inman, R. Dashwood, Production of Ti-Mo Alloys from Mixed Oxide Precursors via the FFC Cambridge Process, J. Electrochem. Soc. 155 (2008) E63-69. doi:10.1149/1.2904454.

[50] H.Y. Kang, J.M. Schoenung, Economic analysis of electronic waste recycling: Modeling the cost and revenue of a materials recovery facility in California, Environ. Sci. Technol. 40 (2006) 1672–1680. doi:10.1021/es0503783.

[51] D.G. Lovering, Molten Salt Technology, Springer Science + Business Media New York, New York, 1982. doi:10.1007/978-1-4757-1724-2.

[52] American Chemical Society, Production of aluminium metal by electrochemistry, 1997.

[53] L. Segws, A. Fontana, R. Winand, Electrochemical boriding of iron in molten salts, Electrochim. Acta. 36 (1991) 41. doi:10.1016/0013-4686(91)85177-9.

[54] C. Schwandt, a. T. Dimitrov, D.J. Fray, The preparation of nano-structured carbon materials by electrolysis of molten lithium chloride at graphite electrodes, J. Electroanal. Chem. 647

(2010) 150–158. doi:10.1016/j.jelechem.2010.06.008.

[55] S. Basu, A.K. Lahiri, S. Seetharaman, Phosphorus Partition between Liquid Steel and CaO-SiO2-FeOx-P2O5-MgO Slag Containing 15 to 25 Pct FeO, Metall. Mater. Trans. B. 38 (2007) 623–630. doi:10.1007/s11663-007-9063-0.

[56] K.E. Einarsrud, The Modified Quasichemical Model: Applications to molten salts, 2008.

[57] M. Temkin, No Title, Acta Physico-Chimica. 20 (1945) 411.

[58] L. Pauling, The Nature of the Chemical Bond, 3rd ed., Cornell University Press, Ithaca, 1960.

[59] H. Rowell, Liquid-Liquid Extraction in the Sodium Oxide-Boron Oxide-Sodium Chloride System, Inorg. Chem. 4 (1965) 1802–1806.

[60] H. Gaye, J. Welfringer, Modelling of the thermodynamic properties of complex metallurgical slags, in: Second Int. Symp. Metall. Slags Fluxes, TMS-AIME, Nevada, 1984: pp. 281–294.

[61] D.R. Gaskell, The Thermodynamic Properties and Structures of Slags, Metallurgical Treaties, Metallurgical Society of AIME, Warrendale, 1981.

[62] R.H. Fowler, E.A. Guggenheim, Statistical Thermodynamics, Cambridge University Press, 1939.

[63] E.S. Treatment, A. Bonomi, H. Giess, C. Gentaz, R. De Drize, Electrochemical boriding of molybdenum in molten salts, Electrodepos. Surf. Treat. 1 (1973) 419–427. doi:10.1016/0300-9416(73)90025-4.

[64] G. Kartal, S. Timur, M. Urgen, A. Erdemir, Electrochemical boriding of titanium for improved mechanical properties, Surf. Coatings Technol. 204 (2010) 3935–3939. doi:10.1016/j.surfcoat.2010.05.021.

[65] H. Çelikkan, M.K. Öztürk, H. Aydin, M.L. Aksu, Boriding titanium alloys at lower temperatures using electrochemical methods, Thin Solid Films. 515 (2007) 5348–5352. doi:10.1016/j.tsf.2007.01.020.

[66] Y.S. Mustafa Alajerami, S. Hashim, W.M. Saridan Wan Hassan, A.T. Ramli, The effect of CuO and MgO impurities on the optical properties of lithium potassium borate glass, Phys. B Condens. Matter. 407 (2012) 2390–2397. doi:10.1016/j.physb.2012.03.029.

[67] G.A. Appleby, C.M. Bartle, G.V.M. Williams, A. Edgar, Lithium borate glass ceramics as thermal neutron imaging plates, Curr. Appl. Phys. 6 (2006) 389–392. doi:10.1016/j.cap.2005.11.025.

[68] S. Ozawa, H. Sato, T. Saito, T. Motegi, J. Yu, Production of Nd–Fe–B alloys by the glass slag method, J. Appl. Phys. 91 (2002) 8831. doi:10.1063/1.1456409.

[69] A. Abbasalizadeh, S. Seetharaman, L. Teng, S. Sridhar, O. Grinder, Y. Izumi, M. Barati, Highlights of the Salt Extraction Process, Jom. 65 (2013) 1552–1558. doi:10.1007/s11837-013-0752-7.

[70] M. Medlin, K. Sienerth, H. Schreiber, Electrochemical determination of reduction potentials in glass-forming melts, J. Non. Cryst. Solids. 240 (1998) 193–201. http://www.sciencedirect.com/science/article/pii/S0022309398006978 (accessed October 18, 2013).

[71] S.S. Zumdahl, Chemical Principles, Houghton Mifflin Company, 2002.

[72] M. Blander, Thermodynamic properties of molten-salt solutions, Oak Ridge National Laboratory, 1962. doi:10.1007/978-94-009-3863-2_2.

[73] A. Mori, I.L. Maksimov, On the Temkin model of solid–liquid interface, J. Cryst. Growth. 200 (1999) 297–304. doi:10.1016/S0022-0248(98)01397-9.

[74] T. Saito, H. Sato, S. Ozawa, J. Yu, T. Motegi, The extraction of Nd from waste Nd–Fe–B alloys by the glass slag method, J. Alloys Compd. 353 (2003) 189–193. doi:10.1016/S0925-8388(02)01202-1.

[75] T. Saito, H. Sato, S. Ozawa, T. Motegi, The Extraction of Sm from Sm-Co alloys by the Glass Slag Method, Mater. Trans. 44 (2003) 637–640. doi:10.2320/matertrans.44.637.

[76] J.Z. Xiao, H.W. Kui, Solidification of undercooled molten Cu30Ni70, J. Mater. Res. 14 (1999) 1771–1781.

[77] H. Doweidar, Consideration of the boron oxide anomaly, J. Mater. Sci. 25 (1990) 253–258.

[78] H. Doweidar, G.M. El-Damrawi, Y.M. Moustafa, R.M. Ramadan, Density of mixed alkali borate glasses: A structural analysis, Phys. B Condens. Matter. 362 (2005) 123–132. doi:10.1016/j.physb.2005.02.001.

[79] H. Doweidar, G. El-Damrawi, M. Al-Zaibani, Distribution of species in Na2O–CaO–B2O3 glasses as probed by FTIR, Vib. Spectrosc. 68 (2013) 91–95. doi:10.1016/j.vibspec.2013.05.015.

[80] H. Aboud, H. Wagiran, R. Hussin, H. Ali, Y. Alajerami, M. a Saeed, Thermoluminescence properties of the Cu-doped lithium potassium borate glass., Appl. Radiat. Isot. 90C (2014) 35–39. doi:10.1016/j.apradiso.2014.01.012.

[81] Y.S.M. Alajerami, S. Hashim, W.M.S. Wan Hassan, A.T. Ramli, The effect of titanium oxide on the optical properties of lithium potassium borate glass, J. Mol. Struct. 1026 (2012) 159–167. doi:10.1016/j.molstruc.2012.05.047.

[82] H.P. Lim, A. Karki, S. Feller, J.E. Kasper, G. Sumcad, The density of potassium borate glasses related to atomic arrangements, J. Non. Cryst. Solids. 91 (1987) 324–332.

[83] M.I.E.-S. M. Morsi, S. El-Konsol, Optical spectra of borate glasses containing Ti and Co in relation to their structure, J. Non. Cryst. Solids. 83 (1986) 241–250.

[84] Y. Matsuda, Y. Fukawa, M. Kawashima, S. Mamiya, S. Kojima, Dynamic glass transition and fragility of lithium borate binary glass, Solid State Ionics. 179 (2008) 2424–2427. doi:10.1016/j.ssi.2008.09.011.

[85] A. Kajinami, T. Kotake, S. Deki, S. Kohara, The structural analysis of manganese borate glass by high-energy X-ray diffraction measurement, Nucl. Instruments Methods Phys. Res. Sect. B Beam Interact. with Mater. Atoms. 199 (2003) 34–37. doi:10.1016/S0168-583X(02)01399-X.

[86] M. Dawy, A. Salama, Electrical and optical properties of some sodium borate glasses, Mater. Chem. Phys. 71 (2001) 137–147. doi:10.1016/S0254-0584(01)00280-2.

[87] Y. Lwin, Chemical equilibrium by Gibbs energy minimization on spreadsheets, Int. J. Eng. Educ. 16 (2000) 335–339. http://www.ijee.ie/articles/Vol16-4/Ijee1157.pdf.

[88] G. Ilonca, I. Ardelean, Magnetic behaviour of some potassium-borate glasses with vanadium and manganese ions, J. Magn. Magn. Mater. 46–57 (1986) 86–87.

[89] Y. Matsuda, Y. Fukawa, C. Matsui, Y. Ike, M. Kodama, S. Kojima, Calorimetric study of the glass transition dynamics in lithium borate glasses over a wide composition range by modulated DSC, Fluid Phase Equilib. 256 (2007) 127–131. doi:10.1016/j.fluid.2007.03.011.

[90] X. Liu, W. Zhu, X. Cui, T. Liu, Q. Zhang, Facile thermal conversion route synthesis, characterization, and optical properties of rod-like micron nickel borate, Powder Technol. 222 (2012) 160–166. doi:10.1016/j.powtec.2012.02.026.

[91] N. Eustathopoulos, M.G. Nicholas, B. Drevet, Wettability at High Temperatures, Elsevier Science Ltd, 1999.

[92] G.J. De Koning, P.J. Van Der Put, Boronation of thin transition metal films, React. Solids. 3

(1987) 101–111. doi:10.1016/0168-7336(87)80021-9.

[93] C. Kaptay, S.A. Kuznetsov, Electrochemical synthesis of refractory borides from molten salts, Plasmas Ions. 2 (1999) 45–56. doi:10.1016/S1288-3255(00)87686-8.

[94] M. Makyta, K.M. Ovsk, P. Fellner, Mechanism of the cathode process in the electrolytic boriding in molten salts, Electrochim. Actamica Acta. 29 (1984) 1653. doi:10.1016/0013-4686(84)89006-4.

[95] F. Xie, L. Sun, J. Pan, Characteristics and mechanisms of accelerating pack boriding by direct current field at low and moderate temperatures, Surf. Coatings Technol. 206 (2012) 2839–2844. doi:10.1016/j.surfcoat.2011.12.003.

[96] J. Ma, Y. Gu, L. Shi, L. Chen, Z. Yang, Y. Qian, Reduction–boronation route to chromium boride (CrB) nanorods, Chem. Phys. Lett. 381 (2003) 194–198. doi:10.1016/j.cplett.2003.09.128.

[97] L. Chen, Y. Gu, L. Shi, Z. Yang, J. Ma, Y. Qian, A reduction–boronation route to nanocrystalline titanium diboride, Solid State Commun. 130 (2004) 231–233. doi:10.1016/j.ssc.2004.01.037.

[98] J.E. Shelby, Introduction to Glass Science and Technology, 2nd editio, Royal Society of Chemistry, 2005. https://books.google.co.uk/books?id=ZeF_QLW6-xsC&pg=PA95&lpg=PA95&dq=borate+anomaly&source=bl&ots=RuEwyjVnEQ&sig=cjcaSPphK6kk_o3ePrgq-ZFwUno&hl=en&sa=X&ved=0ahUKEwjF-5q1jM7QAhXGC5oKHV08A5cQ6AEIJTAB#v=onepage&q=borate anomaly&f=false.

[99] M. Schuch, C. Trott, P. Maass, Network forming units in alkali borate and borophosphate glasses and the mixed glass former effect, RSC Adv. 1 (2011) 1370–1382. doi:10.1039/C1RA00583A.

[100] G. Westphal, G. Kristen, W. Wegener, P. Ambatiello, H. Geyer, B. Epron, C. Bonal, G. Steinhauser, F. Götzfried, Sodium Chloride, in: Ullmann's Encycl. Ind. Chem., Wiley-VCH Verlag GmbH & Co. KGaA, 2000. doi:10.1002/14356007.a24_317.pub4.

[101] R. Fathi, S. Sanjabi, Electrodeposition of nanostructured Ni(1−x)Mnx alloys films from chloride bath, Curr. Appl. Phys. 12 (2012) 89–92. doi:10.1016/j.cap.2011.04.047.

[102] H.-S. Shin, J.-M. Hur, S.M. Jeong, K.Y. Jung, Direct electrochemical reduction of titanium dioxide in molten lithium chloride, J. Ind. Eng. Chem. 18 (2012) 438–442. doi:10.1016/j.jiec.2011.11.111.

[103] C.R. Stafford, C.M. Haarberg, The electrodeposition of Al-Nb alloys from chloroaluminate electrolytes, Plasmas Ions. 1 (1999) 35–44.

[104] M. Zhang, W. Han, M. Zhang, F. Zhu, Y. Xue, Z. Zhang, Electrochemical formation process and phase control of Mg-Li-Ce alloys in molten chlorides, J. Rare Earths. 31 (2013) 609–615. doi:10.1016/S1002-0721(12)60329-9.

[105] H. Kawamura, K. Moritani, Discharge electrolysis in molten chloride: formation of fine silver particles, Plasmas Ions. (1998) 29–36. doi:10.1016/S1288-3255(99)80004-5.

[106] Y. Liu, G. Ye, L. Yuan, K.- Liu, Y. Feng, Z. Li, Z. Chai, W. Shi, Electroseparation of thorium from ThO2 and La2O3 by forming Th-Al alloys in LiCl-KCl eutectic, Electrochim. Acta. (2015). doi:10.1016/j.electacta.2015.01.128.

[107] R. Baughman, R. Lefever, W. Wilcox, Evaporation of sodium chloride melts, J. Cryst. Growth. 8 (1971) 317–323. doi:10.1016/0022-0248(71)90259-4.

[108] H. Gaur, H. Jindal, Standard electrode potentials in molten chlorides—II, Electrochim. Acta. 15 (1970) 1113–1126. doi:10.1016/0013-4686(70)85004-6.

[109] Y. Xue, Y. Yan, M. Zhang, W. Han, Z. Zhang, Electrochemical formation of Mg-Li-Y alloys by

co-deposition of magnesium, lithium and yttrium ions in molten chlorides, J. Rare Earths. 30 (2012) 1048–1054. doi:10.1016/S1002-0721(12)60177-X.

[110] D.S. Kostick, 2008 Minerals Yearbook - Salt, 2010.

[111] P.Y. Shevelin, N.G. Molchanova, A.N. Yolshin, N.N. Batalov, Electron transfer in an electron-ion molten mixture of CuCl-CuCl2-MeCl (Me = Li, Na, K, Cs), Electrochim. Acta. 48 (2003) 1385–1394. doi:10.1016/S0013-4686(03)00005-7.

[112] I.N. Levine, Physical chemistry, 6th editio, McGraw-Hill Companies, 1937. doi:10.1039/c1cs15191f.

[113] I. Mills, T. Cvitas, Green Book, 2nd ed.: IUPAC Quantities, Units and Symbols in Physical Chemistry., Second Edi, Blackwell Scientific Publications, Oxford, 1993.

[114] A. Bard, L. Faulkner, Electrochemical methods: fundamentals and applications, John Wiley & Sons, Inc., Austin, 1980.

[115] A. Lewenstam, F. Scholz, Handbook of Reference Electrodes, Springer Berlin Heidelberg, Berlin, Heidelberg, 2013. doi:10.1007/978-3-642-36188-3.

[116] P.H. Rieger, Electrochemistry, Prentice-Hall, Inc., New Jersey, 1987.

[117] Q. Xu, C. Schwandt, D.J. Fray, Electrochemical investigation of lithium and tin reduction at a graphite cathode in molten chlorides, J. Electroanal. Chem. 562 (2004) 15–21. doi:10.1016/j.jelechem.2003.07.032.

[118] W. Vonau, W. Oelßner, U. Guth, J. Henze, An all-solid-state reference electrode, Sensors Actuators B Chem. 144 (2010) 368–373. doi:10.1016/j.snb.2008.12.001.

[119] Y. Wen, X. Wang, Characterization and application of a metallic tungsten electrode for potentiometric pH measurements, J. Electroanal. Chem. 714–715 (2014) 45–50. doi:10.1016/j.jelechem.2013.12.031.

[120] L. Su, K. Liu, Y. Liu, L. Wang, L. Yuan, Electrochemical behaviors of Dy (III) and its co-reduction with Al (III) in molten LiCl-KCl salts, Electrochim. Acta. 147 (2014) 87–95. http://www.sciencedirect.com/science/article/pii/S0013468614019264 (accessed December 12, 2014).

[121] Q. Xu, C. Schwandt, G. Chen, D. Fray, Electrochemical investigation of lithium intercalation into graphite from molten lithium chloride, J. Electroanal. …. 530 (2002) 16–22. http://www.sciencedirect.com/science/article/pii/S0022072802009981 (accessed October 15, 2014).

[122] L.E. Barosse-Antle, A.M. Bond, R.G. Compton, A.M. O'Mahony, E.I. Rogers, D.S. Silvester, No Titl, Chem Asian J. 5 (2010) 202.

[123] J. Crank, The mathematics of diffusion, Oxford University Press, Oxford, 1975.

[124] B. Børresen, G. Haarberg, R. Tunold, Electrodeposition of magnesium from halide melts—charge transfer and diffusion kinetics, Electrochim. Acta. 42 (1997) 1613–1622. doi:10.1016/S0013-4686(96)00322-2.

[125] G.M. Haarberg, T. Støre, R. Tunold, Metal deposition from chloride melts : I . Rates of diffusion in solvent melt, Electrochmica Acta. 76 (2012) 256–261. doi:10.1016/j.electacta.2012.05.003.

[126] A. Martínez, B. Børresen, Electrodeposition of magnesium from the eutectic LiCl–KCl melt, J. Appl. Electrochem. 34 (2004) 1271–1278. doi:10.1007/s10800-004-1761-6.

[127] H. Ebe, M. Ueda, T. Ohtsuka, Electrodeposition of Sb, Bi, Te, and their alloys in AlCl3-NaCl-KCl molten salt, Electrochim. Acta. 53 (2007) 100–105. doi:10.1016/j.electacta.2007.03.017.

[128] F. Gao, C. Wang, L. Liu, J. Guo, S. Chang, L. Chang, R. Li, Y. Ouyang, Electrode process of La(III) in molten LiCl-KCl, J. Rare Earths. 27 (2009) 986–990. doi:10.1016/S1002-0721(08)60375-0.

[129] G.J. Hills, D.J. Schiffrin, J. Thomopson, No Title, Electrochim. Acta. (1974) 657.

[130] L.D. Brown, R. Abdulaziz, R. Jervis, V.J. Bharath, R.C. Attwood, C. Reinhard, L.D. Connor, S.J.R. Simons, D. Inman, D.J.L. Brett, P.R. Shearing, Following the electroreduction of uranium dioxide to uranium in LiCl-KCl eutectic in situ using synchrotron radiation, J. Nucl. Mater. 464 (2015) 256–262. doi:10.1016/j.jnucmat.2015.04.037.

[131] G.M. Haarberg, J. Thonstad, Electrochemical properties of metal-molten salt mixtures, J. Appl. Electrochem. 19 (1989) 789–801. doi:10.1007/BF01007924.

[132] I. Ueda, M. Baba, T. Kikuchi, R.O. Suzuki, Formation of niobium powder by electrolysis in molten salt, Electrochim. Acta. 100 (2013) 269–274. doi:10.1016/j.electacta.2013.01.054.

[133] M. Zhang, Y. Yang, W. Han, M. Li, Y. Sun, Y. Yan, Separation of SmCl3 from SmCl3-DyCl3 system by Electrolysis in KCl-LiCl-MgCl2 Molten Salts, Energy Procedia. 39 (2013) 375–381. doi:10.1016/j.egypro.2013.07.225.

[134] Y.-L. Liu, L.-Y. Yuan, G.-A. Ye, M.-L. Zhang, H. He, H.-B. Tang, R.-S. Lin, Z.-F. Chai, W.-Q. Shi, Electrochemical extraction of samarium from LiCl-KCl melt by forming Sm-Zn alloys, Electrochim. Acta. 120 (2014) 369–378. doi:10.1016/j.electacta.2013.12.081.

[135] K. Liu, L.-Y. Yuan, Y.-L. Liu, X.-L. Zhao, H. He, G.-A. Ye, Z.-F. Chai, W.-Q. Shi, Electrochemical reactions of the Th4+/Th couple on the tungsten, aluminum and bismuth electrodes in chloride molten salt, Electrochim. Acta. 130 (2014) 650–659. doi:10.1016/j.electacta.2014.03.085.

[136] Y. Xu, L.S. Chumbley, F.C. Laabs, Liquid metal extraction of Nd from NdFeB magnet scrap, J. Mater. Res. 15 (2011) 2296–2304. doi:10.1557/JMR.2000.0330.

[137] P. Hébant, G.S. Picard, Electrochemical investigations of the liquid lithium/(LiCl–KCl eutectic melt) interface. Chronopotentiometric and electrochemical impedance spectroscopy measurements, Electrochim. Acta. 43 (1998) 2071–2081. doi:10.1016/S0013-4686(97)10141-4.

[138] M. Itoh, S. Sato, T. Yokokawa, E.m.f. measurements of molten mixtures of lithium oxide +, sodium oxide +, and potassium oxide + boron oxide, J. Chem. Thermodyn. 8 (1976) 339.

[139] B.L. Dunicz, R.C. Scheidt, Immiscibility Diagrams of Molten Sodium Chloride - Sodium Polyborates at 810 and 980 C, J. Chem. Eng. Data. 11 (1966) 566–570. doi:10.1021/je60031a029.

[140] M. Pourbaix, Atlas of electrochemical equilibria in aqueous solutions, 2nd Editio, National Association of Corrosion Engineers, Houston, 1974. doi:978-0915567980.

[141] R. Littlewood, Diagrammatic Representation of the Thermodynamics of Metal-Fused Chloride Systems, J. Electrochem. Soc. 109 (1962) 525. doi:10.1149/1.2425462.

[142] G.J. Janz, N.P. Bansal, Molten Salts Data: Diffusion Coefficients in Single and Multi-Component Salt Systems, J. Phys. Chem. 11 (1982) 505–693. doi:10.1063/1.555665.

[143] A.M. Martínez, B. Børresen, G.M. Haarberg, Y. Castrillejo, R. Tunold, Electrodeposition of Magnesium from CaCl[sub 2]-NaCl-KCl-MgCl[sub 2] Melts, J. Electrochem. Soc. 151 (2004) C508. doi:10.1149/1.1758814.

[144] S. Wang, G.M. Haarberg, E. Kvalheim, Electrochemical Behavior of Dissolved Fe2O3 in Molten CaCl2-KF, J. Iron Steel Res. Int. 15 (2008) 48–51. doi:10.1016/S1006-706X(08)60265-4.

[145] Y. Leng, Materials Characterization, Wiley-VCH, 2013.

[146] G.J. Hills, Electrochemistry, Vol 2: A Review of Chemical Literature, CRC Press, 1990. https://books.google.co.uk/books?id=VFZuKjS5tPsC&.

[147] P. Migowski, D. Zanchet, G. Machado, M.A. Gelesky, S.R. Teixeira, J. Dupont, Physical chemistry of ionic liquids., Phys. Chem. Chem. Phys. 12 (2010) 1648. doi:10.1039/c001176m.

[148] http://intro.chem.okstate.edu/1314f00/lecture/chapter7/BornHaber2.GIF, (n.d.). http://intro.chem.okstate.edu/1314f00/lecture/chapter7/BornHaber2.GIF.

[149] A.A.J. Torrieto, Electrochemistry in ionic liquids: Applications, Springer International Publishing, 2015. doi:10.1007/978-3-319-15132-8.

[150] M. Misra, K.S. Raja, A. V. Jaques, S. Baral, Effect of Addition of Multi-Component Lanthanides to LiCl-KCl Eutectic on Thermal and Electrochemical Properties, in: ECS Trans., 2010: pp. 351–360. doi:10.1149/1.3484793.

[151] E. Winkel Jessen, Mathematical Modeling of a Hall Héroult Aluminum Reduction Cell, Technical University of Denmark, 2008.

[152] Y. Marcus, Volumetric behavior of molten salts, Thermochim. Acta. 559 (2013) 111–116. doi:10.1016/j.tca.2013.03.009.

[153] M.D. Donne, S. Dorner, Measurements of Density and of Thermal Expansion Coefficient of Sodium Tetraborate (Borax)-UO2 and of Sodium Metaborate-UO2 Solutions, J. Nucl. Mater. 118 (1983) 195–205. doi:10.1016/0022-3115(83)90225-8.

[154] A.C. Fisher, Electrode Dynamics, Oxford University Press, New York, 2006.

[155] R.S. Nicholson, Theory and Application of Cyclic Voltammetry for Measurement of Electrode Reaction Kinetics, Anal. Chem. 37 (1965) 1351–1355. doi:10.1021/ac60230a016.

[156] W.J. Boettinger, U.R. Kattner, J.H. Perepezko, DTA and Heat-flux DSC Measuremenents of Alloy Melting and Freezing, National Institute of Standards and Technology, Washington, 2006. doi:10.1016/B978-008044629-5/50005-7.

[157] X. Hou, B.T. Jones, Inductively Coupled Plasma/Optical Emission Spectrometry, in: Encycl. Anal. Chem., John Wiley & Sons, Ltd., Chichester, 2006: pp. 9468–9485. doi:10.1002/9780470027318.a5110.

[158] F. Natterer, F. Wubbeling, Reconstruction Algorithms, in: Math. Methods Image Reconstr., Society for Industrial and Applied Mathematics, 2001: pp. 81–137. doi:doi:10.1137/1.9780898718324.ch5.

[159] X. Li, J. Zhu, The Convergence of Two Algorithms for Compressed Sensing Based Tomography, Adv. Comput. Tomogr. 1 (2012) 30–36. doi:10.4236/act.2012.13007.

[160] B. Rao, D. Gaskell, The thermodynamic activity of MnO in melts containing SiO2, B2O3, and TiO2, Metall. Trans. B. 12 (1981) 469–477. http://link.springer.com/article/10.1007/BF02654316 (accessed July 7, 2014).

[161] Y. Zhu, K. Mimura, M. Isshiki, Oxidation Mechanism of Cu 2 O to CuO at 600 – 1050 ◦ C, Oxid. Met. 62 (2004) 207–222.

[162] N.N. Greenwood, A. Earnshaw, Chemistry of the Elements, 2nd ed., 1997.

[163] G. Brauer, Handbook of Preparative Inorganic Chemistry, 2nd ed., 1963.

[164] N.R. Lugg, G. Kothleitner, N. Shibata, Y. Ikuhara, On the quantitativeness of EDS STEM, Ultramicroscopy. 151 (2015) 150–159. doi:10.1016/j.ultramic.2014.11.029.

[165] M. Abbasi, M. Dehghani, H.U. Guim, D.I. Kim, Investigation of Fe-rich fragments in aluminum-steel friction stir welds via simultaneous Transmission Kikuchi Diffraction and EDS, Acta Mater. 117 (2016) 262–269. doi:10.1016/j.actamat.2016.06.064.

[166] A.S. Gorzalski, C. Donley, O. Coronell, Elemental composition of membrane foulant layers using EDS, XPS, and RBS, J. Memb. Sci. 522 (2016) 31–44. doi:10.1016/j.memsci.2016.08.055.

[167] L.T. Gonz??lez, F.E.L. Rodr??guez, M. S??nchez-Dom??nguez, C. Leyva-Porras, L.G. Silva-Vidaurri, K. Acuna-Askar, B.I. Kharisov, J.F. Villarreal Chiu, J.M. Alfaro Barbosa, Chemical and morphological characterization of TSP and PM2.5 by SEM-EDS, XPS and XRD collected in the metropolitan area of Monterrey, Mexico, Atmos. Environ. 143 (2016) 249–260. doi:10.1016/j.atmosenv.2016.08.053.

[168] J.I. Goldstein, D.E. Newbury, P. Echlin, D.C. Joy, C.E. Lyman, E. Lifshin, L. Sawyer, J.R. Michael, Scanning Electron Microscopy and X-Ray, Third edit, 1992. doi:10.1002/1521-3773(20010316)40:6<9823::AID-ANIE9823>3.3.CO;2-C.

[169] K. Raouadi, Z. Fakhfakh, Monte Carlo Calculation of the X-Ray Depth Distributions in an Aluminium Target, Micros. Microanal. Microst. 6 (1995) 415–420.

[170] C.C. Miller, The Stokes-Einstein Law for Diffusion in Solution, Proc. R. Soc. A Math. Phys. Eng. Sci. 106 (1924) 724–749. doi:10.1098/rspa.1924.0100.

[171] S. Lindsay, Introduction to Nanoscience, OUP Oxford, 2009.

[172] T. Ito, N. Kojima, a. Nagashima, Redetermination of the viscosity of molten NaCl at elevated temperatures, Int. J. Thermophys. 10 (1989) 819–831. doi:10.1007/BF00514478.

[173] R.D. Shannon, Revised effective ionic radii and systematic studies of interatomic distances in halides and chalcogenides, Acta Crystallogr. Sect. A. 32 (1976) 751–767. doi:10.1107/S0567739476001551.

[174] J. Jackle, Models of the glass transition, Reports Prog. Phys. 49 (1999) 171–231. doi:10.1088/0034-4885/49/2/002.

[175] M. Allibert, H. Gaye, J. Geiseler, D. Janke, J.B. Keene, D. Kirner, M. Kowalski, J. Lehmann, K.C. Mills, D. Neushutz, R. Parra, C. Saint-Jours, P.J. Spences, M. Susa, M. Tmar, E. Woermann, Slag Atlas, 1995.

[176] C.J. Adkins, Equilibrium thermodynamics, Thirs edit, Cambridge University Press, 2003.

[177] A.D. Pelton, P. Chartrand, The Modified Quasi-Chemical Model: Part II. Multicomponent Slutions, Metall. Mater. Trans. A. 32A (2001) 1355–1360.

[178] A.D. Pelton, S.A. Degterov, G. Eriksson, C. Robelin, Y. Dessureault, The modified quasichemical model I—Binary solutions, Metall. Mater. Trans. B. 31B (2000) 651–659. doi:10.1007/s11663-000-0103-2.

[179] S. Brunauer, P.H. Emmett, E. Teller, Adsorption of Gases in Multimolecular Layers, J. Am. Chem. Soc. 60 (1938) 309–319. doi:10.1021/ja01269a023.

[180] G.J. Hills, D.J. Schiffrin, J. Thompson, Electrochemical Nucleation From Molten Salts 1. Diffusion Controlled Electrode Position of Silver From Alkali, Electrochim. Acta. 9 (1974) 657–670. doi:10.1016/0013-4686(74)80008-3.

[181] A.J. Bard, L.R. Faulkner, Electrochemical Methods - Fundamentals and Applications, Second Edi, Wiley, 2004.

[182] S. Arora, J. Acharya, A. Verma, P.K. Panigrahi, Multilevel thresholding for image segmentation through a fast statistical recursive algorithm, Pattern Recognit. Lett. 29 (2008) 119–125. doi:10.1016/j.patrec.2007.09.005.

[183] G.J. Janz, N.P. Bansal, Molten Salts Data: Diffusion Coefficients in Single and Multi-Component Salt Systems, 1982.

[184] J. Wisniak, Borax, boric acid, and boron - From exotic to commodity, Indian J. Chem. Technol. 12 (2005) 488–500.

[185] Z. Kamberovic, M. Korac, D. Ivsic, V. Nikolic, M. Ranitovic, Hydrometallurgical Process for Extraction of, Metall. Mater. Eng. 15 (2009) 231–243.

[186] London Metal Exchange - Official Prices, (n.d.). http://www.lme.com/home.asp (accessed June 7, 2016).

[187] Unit kWh Prices for Business Electricity, (2016). http://www.businesselectricityprices.org.uk/cost-per-kwh (accessed June 7, 2016).

[188] G.E. MacKenzie, D. Scott, Handbook of Aluminium: Volume 2: Alloy production and materials manufacturing, Marcel Dekekr, Inc., New York, 2003.

[189] Y. Kashiwaya, C.E. Cicutti, A.W. Cramb, K. Ishii, Development of Double and Single Hot Thermocouple Technique for in Situ Observation and Measurement of Mold Slag Crystallization., ISIJ Int. 38 (1998) 348–356. doi:10.2355/isijinternational.38.348.

# Appendix I

**AutoCAD drawings**

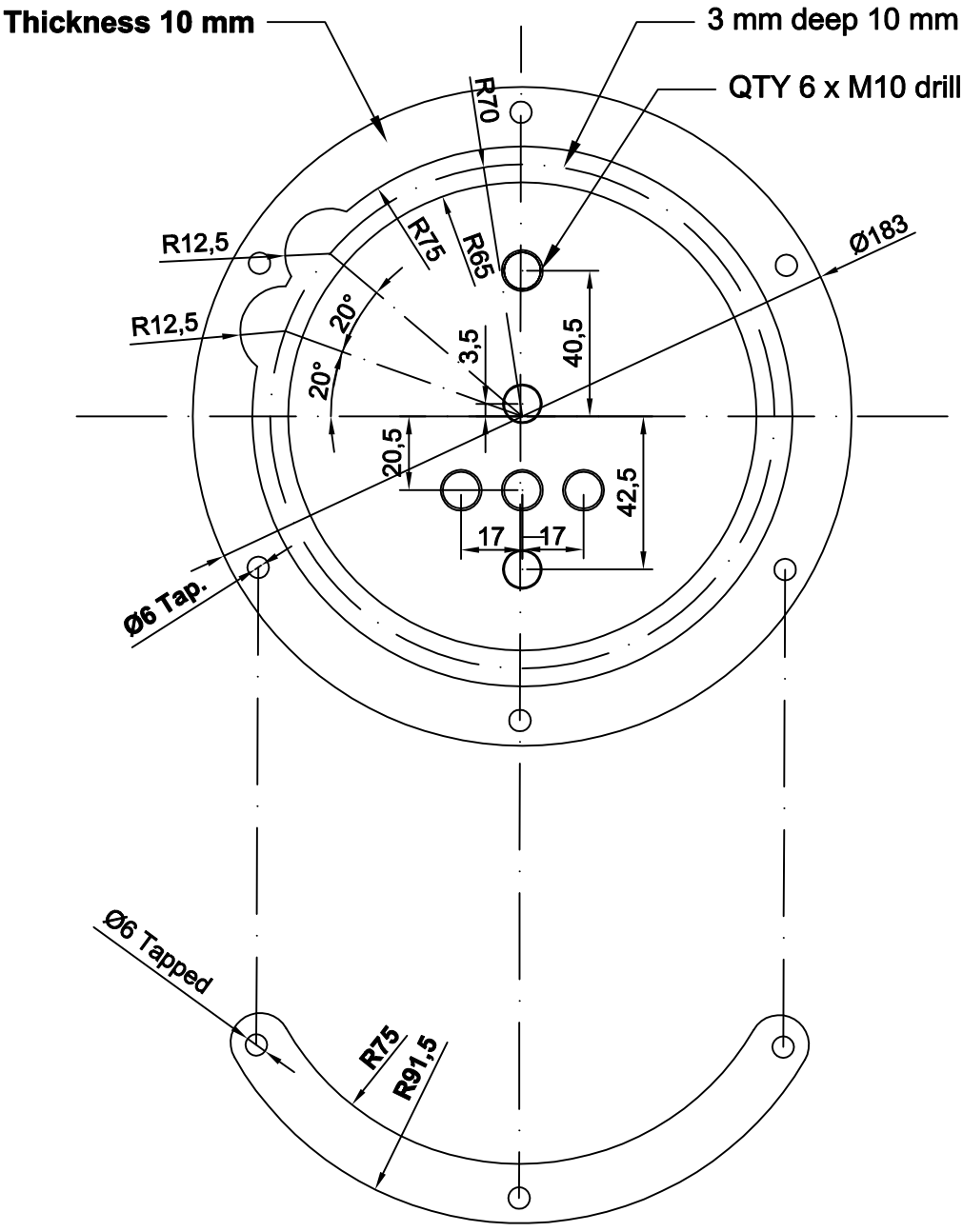


| Ver. 1.2 | | Name | Date |
|---|---|---|---|
| Drawn | | T. Amietszajew | 15/06/2016 |
| Scale 1:2 | Tolerance 0.02 mm | Furnace top plate | |

PRODUCED BY AN AUTODESK EDUCATIONAL PRODUCT

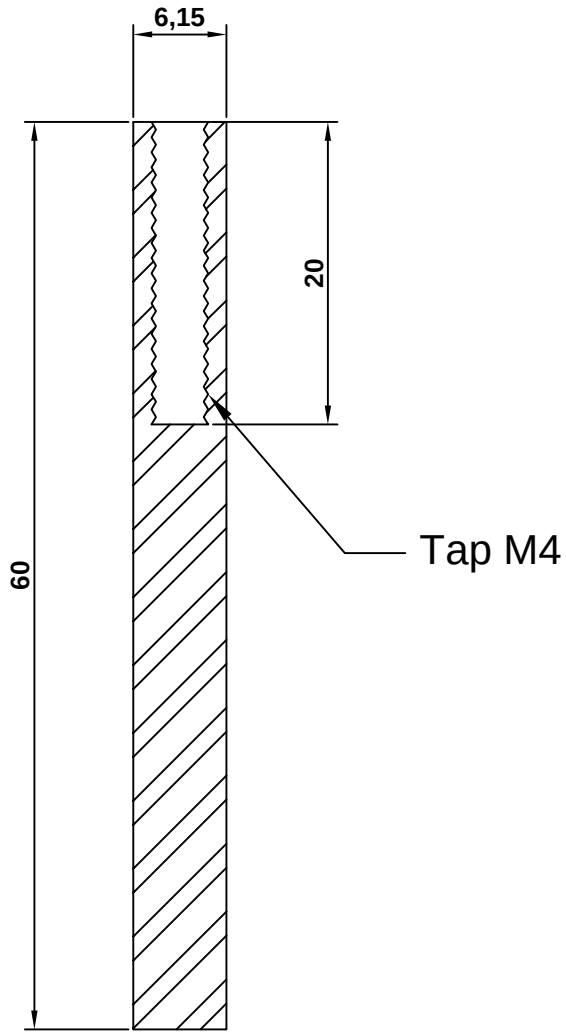


| Ver. 1.1 | | Name | Date |
|---|---|---|---|
| Drawn | | T. Amietszajew | 15/06/2016 |
| Scale 2:1 | Tolerance 0.02 mm | Anode (graphite) | |

PRODUCED BY AN AUTODESK EDUCATIONAL PRODUCT

PRODUCED BY AN AUTODESK EDUCATIONAL PRODUCT

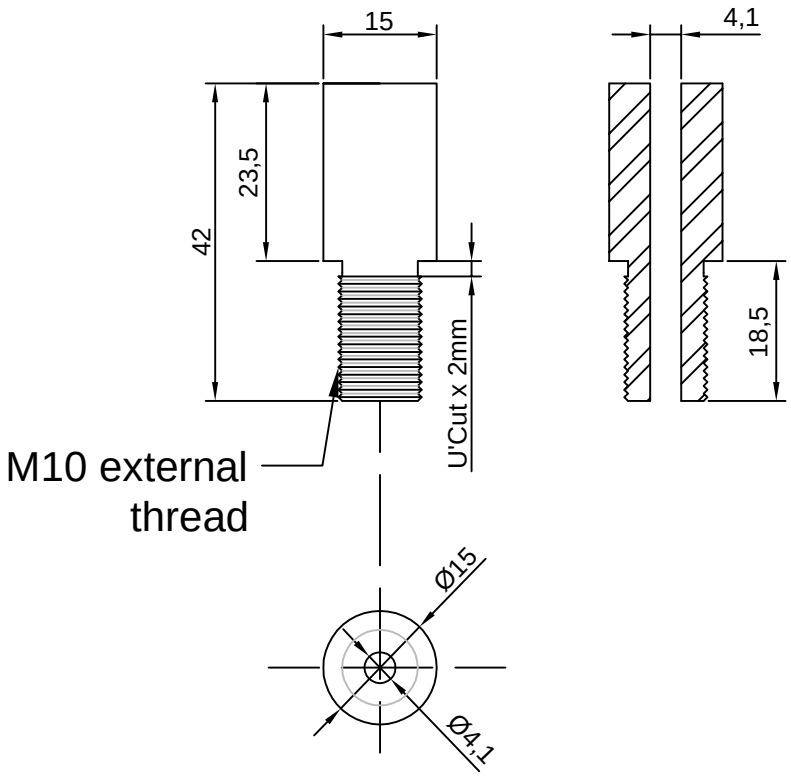


| Ver. 1.0 | | Name | Date |
|---|---|---|---|
| Drawn | | T. Amietszajew | 15/06/2016 |
| Scale 1:1 | Tolerance 0.02 mm | MACOR feedthrough 4.1 mm | |